

Abstract

WANG, YI. Design, Fabrication, and Implantation Control of Flexible Neural Microprobes for Medical Neurology Applications. (Under the direction of Dr. Yuan-Shin Lee.)

This paper presents a new fMRI-compatible flexible neural microprobe and the corresponding flexible neural microprobe implantation strategy using three-dimensional ultrasonic vibration with bio-dissolvable insertion guides. A flexible neural microprobe is a powerful tool for neuromodulation and recording in neuroscience and medical neurology treatments. The designed microprobe of interest in this paper needs to be conducted under functional Magnetic Resonance Imaging (fMRI) for neuroscience studies and investigating circuit-level modulation in a whole-brain scale. The developed neural microprobe was designed to simultaneously record and/or stimulate the neural action potentials under the fMRI to further explore the precise neurophysiological mechanisms and diagnose/control brain diseases. The materials used for the neural microprobe were comprehensively selected for fMRI compatibility. The detailed fabrication procedures of the fMRI compatible flexible neural microprobes were developed. The fabricated neural microprobes were characterized for the validation of the effectiveness.

To successfully implant the flexible neural microprobes with minimized tissue damage, this paper presents a method of applying a three-dimensional longitudinal-twisting (L&T) ultrasonic vibration with a bio-dissolvable insertion guide for flexible planar microelectrode implantation. Due to the thin and flexible substrate of the neural probe, the flexible microprobes are susceptible to buckling and bending during insertion. That leads to the deflection of flexible microelectrodes and even the failure of implantation to successfully reach the target location in the brain during surgery. The proposed longitudinal-twisting vibration is applied to decrease the insertion friction force, thereby reducing the insertion force, microprobe bending, and tissue damage for a successful implant. To generate longitudinal-twisting vibration, a new design of a

3D printed waveguide-based longitudinal-twisting ultrasonic vibratory insertion device is presented in this paper. With the aim to improve the stiffness of neural microprobe and success rate, a bio-dissolvable insertion guide is designed in this paper. It is to reduce the buckling equivalent effective length of a flexible neural probe and thus to enhance the insertion stiffness. The insertion guide is made of the PEG bio-dissolvable material that can be easily flushed away during implantation by water, avoiding secondary damage and interference with the implanted neural probe during surgery.

In vitro and in vivo laboratory experiments were conducted in a surgery room with fMRI for testing and validation. The results were presented in this paper. The experimental results show the proposed new methods are promising in accurately implanting the developed flexible neural microprobe with minimizing implantation bending and tissue damages. The presented design and fabrication of flexible microprobes can be used for medical neuroscience discovery and treatments. The presented method and control strategy can also be readily scaled up for various neural microprobe implantation.

© Copyright 2022

Yi Wang

All Rights Reserved

Design, Fabrication, and Implantation Control of Flexible Neural Microprobes for Medical
Neurology Applications

by
Yi Wang

A dissertation submitted to the Graduate Faculty of
North Carolina State University
in partial fulfillment of the
requirements for the degree of
Doctor of Philosophy

Industrial Engineering

Raleigh, North Carolina
2022

APPROVED BY:

Dr. Yuan-Shin Lee (Committee Chair)

Dr. Paul Cohen

Dr. Mo-Yuen Chow

Dr. Jingyan Dong

Dr. Yen-Yu Ian Shih

DEDICATION

To my parents, Hongjun Wang and Wei Zong, and my in-laws, Wendong Wang and Shuqin Yang, who have always loved me unconditionally and supported me to achieve my goal.

To my beautiful wife, Yuqi Wang, and my lovely daughter Carolyn Wang, for everything they have done for me during these wonderful years.

BIOGRAPHY

Yi Wang received his B.S and M.S. in Precision Instruments and Optoelectronics Engineering from Tianjin University, Tianjin, China, in 2013 and 2015. He joined the Ph.D. program in the Edward P. Fitts Department of Industrial and Systems Engineering at North Carolina State University in 2017. His current research interests include neural microprobe fabrication, ultrasonic transducer design, vibration-assisted needle insertion and machining, computer-aided design and manufacturing, and MEMS manufacturing. At the completion of this dissertation, Yi has received several offers that he is currently considering, and he highly possibly would accept to become a university faculty in academics.

ACKNOWLEDGEMENTS

I would like to express my deepest appreciation and gratitude to my advisor Dr. Yuan-Shin Lee for his continuous support, guidance, and encouragement during my academic and research work at North Carolina State University. Without his valuable guidance and continuous support, I would never have completed my study. His personalities and research ethics keep encouraging me and set a role model for my future career. I also would like to express my gratitude to Dr. Yen-Yu Ian Shih and Dr. SungHo Lee at the University of North Carolina State at Chapel Hill for technical supports, suggestions, and providing access to their lab equipment. I would like to thank my committee members, Dr. Paul Cohen, Dr. Jingyan Dong, and Dr. Mo-Yuen Chow for their efforts and serving in my Ph.D. committee.

I would like to thank the technical staff at North Carolina State University Nanofabrication Facility, Dr. Phil Barletta, Nicole Hedges, Marcio Cerullo, Greg Allion, Jeff Ricker-Hagler, Jim Mitchell for their technical support and helpful discussion in training and setting up the experimental equipment. I would like to thank professors in our department: Dr. Xu Xu, Dr. Karen Chen, Dr. Rohan Shirwaiker, Professor Jason Low. I would like to thank my research group members and colleagues: Daniel Leonard, Dr. Yi Cai, Dr. Yang Cao, Hengfeng Gu, Ping Ren, Sarah Gerkin, Pavel Koprov, Matthew White, Jie Zhai, Jing, Ao, Dr. Li Li, Ken Chen, Kejun Li, Jiali Huang, Hongyu Wang, Gimantha Perera. Thank you all for your support, suggestions, friendship, and inspiration. You have made my journey at NC State much more wonderful and memorable.

TABLE OF CONTENTS

LIST OF FIGURES	viii
LIST OF TABLES	xii
CHAPTER 1 INTRODUCTION	1
1.1 Background	1
1.2 Motivation and Objectives	3
1.3 Dissertation Outline	5
CHAPTER 2 LITERATURE REVIEW	7
2.1 Development of Neural Microelectrode	7
2.2 Why Flexible Neural Microelectrodes Are Needed.....	10
2.3 Fabrication of State-of-art Neural Microelectrodes	12
2.4 Applications of Neural Microelectrodes	14
2.5 Implantation Techniques.....	16
2.5.1 Removable Rigid Shuttle.....	16
2.5.2 Bio-resorbable Polymer Coating	17
2.5.3 Mechanically-adaptive Substrate	18
2.5.4 Bio-inspiration Methods	19
2.5.5 Reinforcement Layer	19
2.5.6 Vibration-assisted Insertion.....	20
2.6 Summary	21
CHAPTER 3 NEURAL MICROPROBE FABRICATION	23
3.1 Materials Selection.....	23
3.1.1 Polyimide.....	23
3.1.2 Metals for Neural Microprobes	25
3.2 Design of Neural Microprobe	27
3.3 Microfabrication Procedures.....	28
3.3.1 Sacrificial Layer	28
3.3.2 First Polyimide Layer	30
3.3.3 Reinforcement layer	33
3.3.4 Second Polyimide Layer	36
3.3.5 Circuit Trace Layer	37
3.3.6 Third Polyimide Layer	39

3.3.7 Dry Etching Openings	40
3.3.8 Gold Electroplating	43
3.3.9 Laser Ablation of the Neural Microprobe Profile	44
3.3.10 Microprobes Releasing	45
3.4 Microprobe Packaging	46
3.5 Summary	47
Chapter 4 CHARACTERIZATION OF NEURAL MICROPROBE	48
4.1 Scanning Electron Microscopy (SEM) Measurement	48
4.2 Electrochemical Impedance Spectroscopy Measurement	51
4.3 Mechanical Characterization	52
4.4 Summary	54
CHAPTER 5 DESIGN AND 3D PRINTED LONGITUDINAL-TORSIONAL TRANSDUCER FOR FLEXIBLE MICROPROBE INSERTION	56
5.1 Introduction	56
5.2 Design Principles	58
5.3 Geometric Design and Configuration of the L&T Transducers	62
5.4 Finite Element Analysis	63
5.4.1 Harmonic Response Analysis	64
5.4.2 L&T Vibration Modal Analysis	70
5.5 3D Printed Prototype of the Waveguide-based Transducer	73
5.6 Characterization of the 3D Printed L&T Transducer	76
5.6.1 Experiments on Impedance Analysis	76
5.6.2 Experiments on Vibrational Characterization	78
5.7 Summary	80
CHAPTER 6 IMPLANTATION STRATEGIES FOR FLEXIBLE NEURAL MICROPROBE	81
6.1 Introduction	81
6.2 Vibration Assisted Insertion	82
6.2.1 Influence of Ultrasonic Vibration	82
6.2.2 Devices Development	86
6.3 Improve Insertion Stiffness with Bio-dissolvable PEG Guide	89
6.4 Experiments and Discussions	92
6.4.1 Insertion Force under the Ultrasonic Vibration	93

6.4.2 Insertion with Bio-dissolvable Guides	97
6.4.3 Insertion Performance with Two Strategies	101
6.4.4 In Vivo Experiments of Neural Microprobe Insertion	103
6.5 Summary	108
CHAPTER 7 CONCLUSIONS AND FUTURE WORKS.....	109
7.1 Conclusions.....	109
7.2 Limitations	112
7.3 Future Works	114
REFERENCES	116

LIST OF FIGURES

Figure 2.1 Wire-type neural microelectrode [8].....	8
Figure 2.2 (a) Utah type intracortical electrode array [18] (b) Michigan type neural electrodes with drug delivery [20].....	9
Figure 2.3 The elastic moduli of different materials [23].	11
Figure 2.4 Implantation with a removable stiffer shuttle [38,56]. (a) An example of a silicon insertion shuttle, (b) Implantation procedure of neural probe with insertion shuttle, (c) Flexible neural probe with a hole for assembly insertion needle, (d) An inserter for the probe in (c).....	17
Figure 2.5 An example of coating the bio-resorbable polymer [63].	18
Figure 2.6 An example of a flexible neural probe with the reinforcement layer [71].....	20
Figure 2.7 Illustration of our proposed flexible neural probe compatible with fMRI.....	21
Figure 3.1 The chemical structure of polyimide PI-2611.....	25
Figure 3.2 Structure of our flexible and fMRI compatible neural probe.....	27
Figure 3.3 Processing flow of the neural microprobes fabrication at NNF.....	28
Figure 3.4 Photo of the DC sputter tool.	30
Figure 3.5 Photo of the Cr/Al sacrificial layer deposited on the wafer.....	30
Figure 3.6 (a) March Asher, (b) TMS Blue-M programmable oven.....	31
Figure 3.7 Spin speed curve of polyimide PI-2611.....	32
Figure 3.8 Photo of the failed polyimide coating.....	33
Figure 3.9 Photo of the four-stages full cured polyimide layer.....	33
Figure 3.10 Photo of deposited Cr layer on the polyimide base.	34
Figure 3.11 (a) YES® ClassOne primer oven, (b) MA6 (Suss MicroTec) contact aligner.	35
Figure 3.12 Photo of patterned Cr reinforcement layer.....	36
Figure 3.13 Photo of the second 24 μm thick polyimide layer.	37
Figure 3.14 Photo of patterned circuit traces layer with a lift-off process.	38
Figure 3.15 Photo of deposited Cr/Cu circuit layer.....	39

Figure 3.16 The spin curve of polyimide PI-2611 coated for 45 seconds..... 40

Figure 3.17 Photo of the third polyimide layer. 40

Figure 3.18 Oxford NGP80 RIE etcher. 42

Figure 3.19 Photo of etched polyimide openings with the Al mask. 42

Figure 3.20 Electroplated gold 3D mushroom-shaped electrode site..... 43

Figure 3.21 Setup of the housemade gold electroplating tool. 44

Figure 3.22 Carbonization line on the edge of the neural microprobe. 45

Figure 3.23 Photo of a fabricated flexible neural microprobe after releasing..... 46

Figure 3.24 Illustration of the PCB for connecting the neural microprobe and Omnetic connector. 47

Figure 4.1 The SEM images of the top view of the neural microprobe. 49

Figure 4.2 The EDS results of the neural microprobe..... 51

Figure 4.3 Laboratory setup for electrochemical impedance spectroscopy measurements. 52

Figure 4.4 Lab Setup of tensile testing and compressive testing. 53

Figure 4.5 Strain-stress curve of the neural microprobe tensile testing. 53

Figure 4.6 Neural microprobe compressive testing..... 54

Figure 5.1 Typical longitudinal-excited L&T ultrasonic transducers: (a) diagonal slits type [87,92]; (b) helical grooves type [93,94]. 57

Figure 5.2 Illustration of the concept of the waveguide-based L&T transducer..... 59

Figure 5.3 Design and configuration of the waveguide-based L&T ultrasonic system. 63

Figure 5.4 Relationship between the number of waveguides and output vibrations..... 66

Figure 5.5 Harmonic response simulation results: (a) vibration amplitudes under the analysis frequency 25 kHz to 27 kHz, (b) working at the resonant frequency 25,514 Hz. 66

Figure 5.6 Harmonic response simulation results: (a) vibration amplitudes under the analysis frequency 56 kHz to 61 kHz, (b) working at the resonant frequency 59,000 Hz. 67

Figure 5.7 Harmonic response simulation results of different cross-section shapes of the waveguide: (a) rectangle shape, (b) triangle shape. 68

Figure 5.8 Maximum stress analysis at its corresponding resonant frequency.	69
Figure 5.9 Maximum stresses under different applied drive voltages.....	70
Figure 5.10 Modal analysis results of the waveguide-based L&T transducer under 20 kHz to 30 kHz. (a) and (b) are a pair of flexing vibrations with a frequency difference of 26 Hz. (c) is an L&T vibration.....	72
Figure 5.11 Modal analysis results of the waveguide-based L&T transducer under 55 kHz to 65 kHz. (a) is an L&T vibration. (b) and (c) are a pair of flexing vibrations with a frequency difference of 220 Hz.....	73
Figure 5.12 The prototype of the waveguide-based transducer fabricated by SLM-AM (a) original 3D printed part, (b) after assembly.	75
Figure 5.13 Laboratory setup for measurement of the L&T transducer.....	76
Figure 5.14 Impedance measurement results of the prototype of the waveguide-based ultrasonic transducer: (a) 24 kHz to 27 kHz; (b) 57 kHz to 65 kHz.	77
Figure 5.15 Experimental setups to measure the vibration amplitudes: (a) longitudinal direction (b) torsional direction.....	79
Figure 5.16 The plot of the L&T displacement amplitudes versus the frequency: (a) 24.0 kHz to 26.5 kHz; (b) 56 kHz to 62 kHz.....	79
Figure 5.17 The plot of vibration amplitudes versus driving voltage.	80
Figure 6.1 The interaction model of planar electrode probe and tissue under the influence of Longitudinal-Twisting vibration.	85
Figure 6.2 Models of vibration-assisted neural probe insertion devices. (a) Longitudinal-Twisting (L-T) vibration, (b) Longitudinal (L) vibration.	87
Figure 6.3 The harmonic response analysis results for both ultrasonic devices. (a) Longitudinal-Twisting vibration, (b) Longitudinal vibration.	89
Figure 6.4 Illustration of an insertion guide reducing the equivalent effective length.....	90
Figure 6.5 An example of a real bent neural microprobe.....	90
Figure 6.6 The illustration of the PEG insertion guide.	91
Figure 6.7 The experiment setup for neural probe implantation.	93
Figure 6.8 Insertion force measurements at 0.4 mm/s insertion speeds with longitudinal vibration, longitudinal-twisting vibration, and no vibration.	95
Figure 6.9 Relationship between the puncture force and insertion force.	95

Figure 6.10 Maximum insertion force at different insertion speeds. 96

Figure 6.11 Relative reductions of insertion forces at different ultrasonic driving voltages. 97

Figure 6.12 The casted PEG insertion guide. 97

Figure 6.13 Experiment setup of probe compression test with a six-axis force sensor..... 98

Figure 6.14 Compression buckling testing results with different thick guides. 99

Figure 6.15 The relationship between the enhancement ratio and the support length ratio (guide thickness/probe length). 100

Figure 6.16 Compression buckling test under the influence of L&T vibration. 100

Figure 6.17 Insertion experiments in 4% Agarose gel with different implantation strategies. . 102

Figure 6.18 Insertion experiments using fabricated neural microprobe..... 103

Figure 6.19 In Vivo experiment setup for neural probe implantation (at UNC neurology surgery room). 104

Figure 6.20 In vivo Implantation of Flexible neural probes on a rat’s brain during surgery (at UNC neurology surgery room). 105

Figure 6.21 fMRI Image of the implanted neural microprobe. 106

Figure 6.22 Results of simultaneous DBS and fMRI. 107

Figure 6.23 fMRI image during DBS on the infralimbic area (IL, A25). 107

Figure 7.1 Photo of a failed lift-off circuit trace layer. 112

Figure 7.2 High power ultrasonic vibration causes the failure of a plastic Luer connector. 114

LIST OF TABLES

Table 3.1 The characteristics of PI-2611 after cure.	25
Table 3.2 Some material properties of thin-film metals.....	26
Table 4.1 Electrochemical impedance spectroscopy measurement results.....	52
Table 5.1 Material properties for the FE model of the ultrasonic transducer.	63
Table 5.2 SLM machining parameters.	74
Table 6.1 Material properties for the FE models of the ultrasonic devices.	88

CHAPTER 1

INTRODUCTION

This chapter provides an introduction of the flexible neural microprobes that can be used under functional Magnetic Resonance Imaging (fMRI) for neuroscience applications and the challenging problems of flexible microprobes implantation for neural medical treatments. The research motivation and objectives are also presented in this chapter.

1.1 Background

Implantable neural microelectrodes as a promising tool are used in fundamental neuroscience to investigate physiological processes at the cellular level, and in neural prosthetics to help restore function in the nervous system [1]. Implantable microprobes provide a critical interface to the nervous system, which can record and/or stimulate neurons electrically. One important application of the neural microprobe is deep brain stimulation (DBS). The DBS can be employed to treat Parkinson's disease (PD), movement disorders, and other neuropsychiatric disorders by delivering electrical signals to target regions of the brain via implanted electrodes [2]. Also, the implantable microelectrode arrays are able to record the neural action potentials or local field potentials in real-time with a high spatial and temporal resolution, which helps us diagnose nervous diseases and reveal the functioning of networks of neurons. Owing to the recording and stimulating capabilities of neural microelectrodes, it has already become a powerful technology for medical diagnostic and therapeutic applications. To better understand the global effect of DBS and assist medical diagnostics, neuroimaging is another useful and noninvasive tool to map the neural circuit change during DBS [2]. To date, a lot of research has started to

simultaneously use DBS and functional magnetic resonance imaging (fMRI) to functionally and unbiasedly map the circuit and network-level connectivity of brain neurons [3]. However, most current neural microelectrodes are not compatible with fMRI, resulting in unreadable imaging results (large shadow artifacts) and potential risks associated with heating, magnetic field interactions, induced currents, and the functional disruption of these devices [4,5]. Therefore, an fMRI-compatible neural microprobe is urgently needed for neuroscience.

The invasive neural interfaces require the implantation of microelectrodes in the brain, which may potentially cause clinical risks due to infection and damage to the tissue. Also, chronic recording of the neural activities requires the microelectrodes to remain stable for long periods and reduce degradation due to the foreign body immune response. To minimize the damage to brain tissue and ensure the recording signal quality, it is crucial and necessary to lower the mechanical mismatch between the neural electrodes and brain tissues. This requires the neural microelectrodes to behave as flexible as “brain tissue”. Therefore, the ideal implantable neural microelectrodes would be flexible with a small cross-section to introduce as little trauma as possible.

Although flexible neural microelectrodes are capable of mitigating the unfavorable mechanical mismatch, they are more susceptible to bending and buckling during implantation due to the decrease of stiffness. Most neural microprobes have a long shaft topology with a small cross-section. This high-aspect-ratio structure allows the electrodes to reach a deep target in the brain with minimum brain tissue damage, but it further reduces the rigidity of the neural probe. The bending and buckling of the neural probe also cause a deflection during the penetration procedure, decreasing the accuracy of the electrode implantation. The displacement of neural electrodes directly influences the accuracy of DBS and electrophysiological recording in the brain.

Therefore, overcoming the challenge of implantation and maintaining the high flexibility of the neural probe is essential for deep brain stimulation and recording.

To date, researchers devised a number of ways to resolve the implantation obstacle of flexible neural interfaces. Although some insertion strategies are able to successfully implant their developed neural microprobes, there are still some potential shortcomings, such as creating a gap between the brain tissue and electrode recording sites, noticeable displacements of the implanted microprobe, secondary damage to the brain tissue, etc. More details will be discussed in the next chapter. In addition, some implantation strategies are designed for specific types of neural microprobes, limiting their versatility. For this purpose, it deserves more research and development on an effective and straightforward implantation method for multiple types of flexible neural interfaces.

1.2 Motivation and Objectives

The objective of this paper is to develop a flexible neural microprobe compatible with fMRI, and corresponding insertion strategies to successfully implant it into a deep brain target location with minimized tissue damage and deflection. The following are the research objectives and the approaches to achieve them.

1) Design and fabrication of an fMRI compatible flexible neural microprobe

In order to use DBS and fMRI simultaneously, an MRI-compatible neural microprobe needs to be designed and manufactured in the cleanroom. For the chronic recording of the nervous system, the microprobe must remain stable in the brain for a long period with good signal quality. This requires a neural microprobe with good flexibility. Although the flexible neural microprobe mitigates the mechanical mismatch to the brain tissue, an appropriate design should be considered

to make the microprobe easy to be implanted. Therefore, it is crucial to optimize the design, materials, and fabrication procedures to make the neural microprobe with high flexibility and fMRI compatibility.

2) Design and development of a three-dimensional ultrasonic vibratory insertion system for flexible microprobe insertions

In this paper, ultrasonic vibration is used for assisting the flexible neural microprobe implantation. Many research concludes that vibration-assisted insertion can effectively improve insertion performance and reduce immune response. The three-dimensional ultrasonic vibration has been demonstrated to possess more advantages than the conventional longitudinal vibration on needle insertion. In this paper, we propose to develop a three-dimensional ultrasonic vibratory insertion system for the implantation of various flexible neural microprobes. To achieve a three-dimensional harmonic vibration, a high-efficiency compact ultrasonic transducer needs to be designed and developed.

3) Implantation strategies for flexible neural probes

Although ultrasonic vibration is capable of improving implantation performance, the mechanism behind it is still unclear. Analytical models and laboratory experiments are needed to study the effects of the three-dimensional ultrasonic vibration-assisted insertion. On the other hand, the ultrasonic vibration-assisted insertion is still difficult to solve the low stiffness dilemma of the flexible microprobe. Although implanting the flexible microprobe with a stiffer needle is a straightforward way, it causes additional trauma and other unwanted disadvantages. Other potential strategies need to be further explored and applied to increase insertion stiffness and success rate.

1.3 Dissertation Outline

The remainder of this paper is organized as follows:

Chapter 2 gives a review of different types of neural microelectrodes, and the motivation for the development of flexible neural microelectrodes. Working with fMRI as an important application of neural microelectrodes for mapping the nervous system is also reviewed, showing the crucial need for a neural microprobe compatible with fMRI. Due to the critical challenges of flexible microprobe implantation, implantation techniques for flexible neural probes are then reviewed.

Chapter 3 presents a detailed design and fabrication procedures of the MRI-compatible flexible neural microprobes that can be used with fMRI to map the circuit and network-level connectivity of the nervous system for neurological diagnosis and neuroscience studies.

Chapter 4 presents the characterization results of our developed fMRI-compatible flexible neural microprobe. The microstructures, mechanical properties, and electrochemical properties are measured to validate the effectiveness of our developed neural microprobe.

Chapter 5 introduces a new design of a waveguide-based longitudinal-torsional (L&T) ultrasonic transducer for the vibration-assisted microprobe insertion. The design philosophy of the ultrasonic transducer is introduced. Finite element (FE) analysis and laboratory experiments are conducted and presented. The experiment results show the new ultrasonic transducer is promising to deliver synchronized longitudinal-torsional vibration with high efficiency.

Chapter 6 adopts the longitudinal-torsional vibration with a bio-dissolvable insertion guide to deliver accurate microprobe insertion with minimized tissue damage and deflection. Both in vitro and in vivo experiments results show that the proposed insertion technique is promising and readily scaled up for various types of neural electrodes.

Chapter 7 summarizes the research works and limitations, and discusses the potential future research directions.

CHAPTER 2

LITERATURE REVIEW

This chapter provides a review of various neural microelectrodes as well as the motivation for developing flexible neural microelectrodes. Working with fMRI as an important application of neural microelectrodes for mapping the nervous system is also reviewed. Due to the critical challenges of flexible probe implantation, existing implantation techniques are then reviewed.

2.1 Development of Neural Microelectrode

Electrical stimulation of nerve tissue and recording of neurons' activity has contributed considerably to neuroscience and neuroengineering. The electrical nature of neurophysiology was first revealed by Italian scientist Luigi Galvani in 1780, who discovered that a dead frog's leg would twitch with the application of an electrical stimulus [6]. This first opened the door for the human to explore the nervous system. Although people took a lot of detours during the exploration of the nervous system at the beginning, a century later, Edgar Adrian, in 1928, first recorded electrical discharges in the nervous system, thereby describing the function of neurons [7,8]. This breakthrough allows people to acquire the electrical activity from neurons by using electrodes, which makes the electrodes an essential tool for neural recording and stimulating systems. In 1952, Hodgkin and Huxley conducted neural recording experiments on thick nerve fibers in squid, finding the neural activity can be marked by millisecond-long 80–100 mV spikes called action potentials. In 1957, Hubel and Wiesel first fabricated a tungsten microwire electrode with a submicrometer-diameter tip size to map the visual path from the retina to the striate cortex in cats [9], marking that people can further measure smaller neurons and axons. That also led the

microwire electrode as a powerful tool for exploring and mapping the organization of neural structures [8]. The microwire electrodes made by other types of biocompatible conducting metals were then reported, such as gold [10], iridium [11], stainless steel [12], platinum [13]. From then, researchers started using various types of microelectrode wires to record spike activities from neurons in brain tissues [9,13,14]. To date, tungsten microwire and carbon fibers are still both widely used. Individual electrode wire has only one channel to record at one time, which largely limits the throughput and exploration of the nervous system. Until 1967, Marg proposed to implant a microwire array (bundles of insulated metal wires) in the brain to collect the neural signals simultaneously [15]. Since the microelectrode arrays enable recording action potentials from different neuron populations simultaneously, it further encourages the development of neural interfaces with multiple recording sites [8,16,17].



Figure 2.1 Wire-type neural microelectrode [8].

By the 1970s, the development of the semiconductor microfabrication and the availability of cleanroom infrastructure facilitate the development of silicon-based multielectrode arrays. The advances in complementary metal-oxide-semiconductor (CMOS) technology promoted that scale-up higher resolution, and smaller neural electrode arrays were designed and fabricated. Two famous types of neural microelectrode arrays appeared, Michigan electrodes in 1970 and Utah Arrays in 1990. The Utah Arrays contain up to 100 vertical shanks on one silicon base, and its recording site is located only at the tip of each silicon shank [18], as shown in Figure 2.2 (a). The

Michigan electrode is planar arrays with several recording sites distributed along the shank [19–21], as shown in Figure 2.2 (b). Both types of neural microelectrodes are able to remain in the brain for a long period to record action potentials. Silicon shanks with metal electrode contacts, like Michigan electrodes, were the most general topology of the current micro neural electrode arrays or probes [8,22]. The number of electrodes on the neural microelectrode arrays has a similar trend as Moor’s Law. The number of electrodes on one shank from several increases to hundreds, which enables larger populations of neurons from several brain structures to be recorded. That also allows accurate sorting and assignment of spikes to individual neurons [23]. In 2007, James et al. designed and fabricated a silicon-based neural probe known as Nueropixel that has 960 recording sites in a 10-mm long, 70 x 20 μm cross-section shank [24].

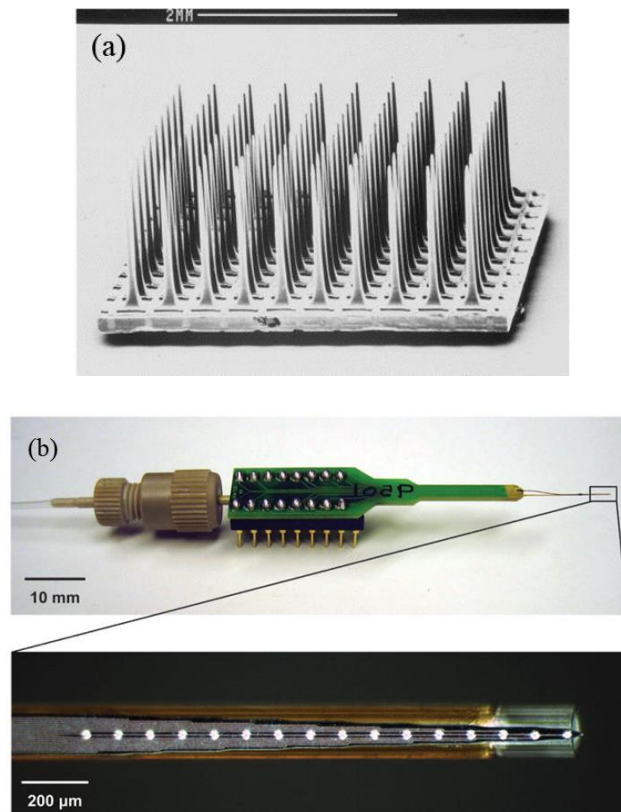


Figure 2.2 (a) Utah type intracortical electrode array [18] (b) Michigan type neural electrodes with drug delivery [20].

2.2 Why Flexible Neural Microelectrodes Are Needed

The invasive neural interfaces require the implantation of microelectrodes in the brain, which may potentially cause clinical risk and other unfavorable consequences [1]. That may directly reduce the signal quality during chronic recording and degradation of the microelectrodes. They are associated with a variety of biological and non-biological mechanisms, including mechanical mismatches between devices and the neural tissue, unwanted micromotion of the array within the brain tissue, immune responses induced by a foreign body, delamination, and chemical corrosion on the implant surface and internal interconnections [25,26]. Acute and chronic tissue responses influence the performance of neural implants for their whole life. Acute injuries are induced during the initial surgical implantation. For example, blood-brain barrier disruption caused by vessel compression and rupture is a typical acute injury, which leads to neuron death, neurodegeneration, and inflammation. Experiments show that the blood-brain barrier disruption accelerates electrode failure [27]. The implanted electrodes also activate the proliferation of microglial cells that are related to both immune response and maintaining homeostasis. Astroglial cells, or astrocytes, play a role in the repair and scarring process after injuries, which will form a dense scar sheath surrounding the foreign implants to protect the central nervous system. This sheath, however, insulates the electrode from neurons and influences the study of neural activities in their native state and environment [23,28].

To minimize the tissue damage and ensure the recording signal quality, it is crucial to lower the mechanical mismatch between the stiff neural interfaces and soft brain tissues. In vivo experiments show that compliant implants can significantly reduce neuroinflammatory responses and have a more stable blood-brain barrier than stiff implants [29,30]. In addition, the mechanical mismatch between the interfaces aggravates micromotions, leading to chronic instability of

recordings. The continuous micromotion of a stiff implant adding movable brain tissue causes repeated chronic damage around brain tissue, including damage and death of neurons near the implant site, proliferation of astrocytes, and microglia [31].

The intrinsic reason for the mechanical mismatch is the inconsistency of Young's moduli of the implants and brain tissue. Figure 2.3 shows the elastic moduli of potential materials for neural microelectrodes. The elasticity modulus of the brain tissue is normally less than 10 KPa, but which of traditional silicon-based neural microelectrode is much higher, at around 130-185 GPa [32]. This huge discrepancy creates a significant mechanical mismatch between the implants and the brain tissue. To lower the elastic moduli of the microelectrodes, the polymer-based flexible microelectrodes were proposed from 2000 [33]. Young's moduli of polymer-based microelectrodes are from 50 MPa to about 10 GPa [32], which are much softer than the silicon-based neural microelectrode. Both in vivo and in vitro experiments demonstrated that the polymer-based neural interfaces have better performance on signal quality and life span due to less damage caused in the brain.

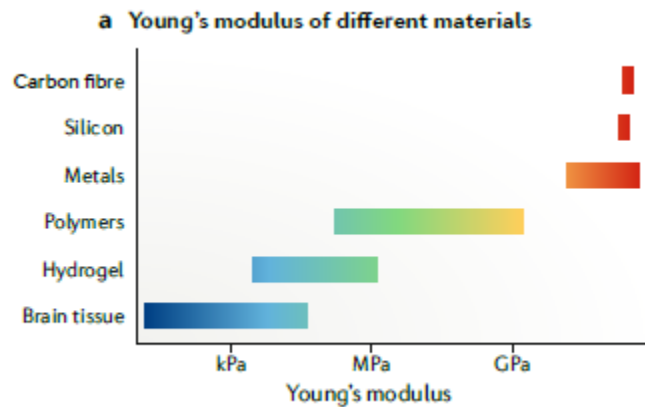


Figure 2.3 The elastic moduli of different materials [23].

With the advent of flexible electronics and the mature of micromachining techniques, different types of flexible neural microprobes were designed and fabricated. Ultra-flexible and smaller with denser electrode numbers neural probe is the trend of future neural microelectrode arrays.

2.3 Fabrication of State-of-art Neural Microelectrodes

To date, many kinds of materials have been employed for neural microelectrodes, including metals, semiconductors, polymers, oxides, glass, nanomaterials, and hybrid materials [28], which can be fabricated by mature microfabrication technologies. Most polymer-based neural microelectrode arrays are based on the planar long shank topology. For example, Lecomte et al. [34] developed a thin, highly compliant neural probe using parylene-C as substrate. Altuna et al. [35] incorporated polyimide and SU-8 to fabricate a microprobe for simultaneous neural depth recording and drug delivery. Mercanzini et al. [36] and Lai et al. [37] developed a long shaft neural probe with more than ten recording sites by employing polyimide. In 2019, Musk and his company Neuralink released polyimide-based arrays of small and flexible “threads”, with as many as 3072 electrodes per array distributed across 96 threads [38]. The fabrication of polymer-based neural probes commonly uses a layer-by-layer additive process procedure in which the conductive metal layer is encapsulated by the polymers. The detailed materials and corresponding process methods are introduced below.

Since the neural electrodes are in direct contact with brain tissue, all the exposed materials of the electrodes should be non-toxic and biocompatible, especially for chronic application. The materials also should have excellent resistance to corrosion, delamination, breakage, and failure in order to have a long span of life. For various types of flexible electrode arrays, it has been demonstrated that biocompatible polymers possess many extraordinary physical and chemical

properties, such as polyimide, Parylene-C, LCP, benzocyclobutene (BCB), Polydimethylsiloxane (PDMS), and SU-8 [26,39]. These polymers have been demonstrated by many groups that chronically implantation does not cause chronic damage and inflammation at the site of injury [26]. To be a substrate and an insulation layer, the polymers should have a good dielectric property. These polymers can be spin-coated using the common method to form different thick polymer films via controlling the coating time and speed. The thickness of the coated film ranges from 1 μm to several hundred μm [39]. Following deposition, some types of polymers require a thermal curing process to complete the cross-linking process, such as polyimide and BCB. Then the polymer layers can be patterned using dry etching with a hard mask in oxygen or fluorine plasma. For patterning thick polymer, DRIE or laser ablation process is capable of removing the polymer, leaving a vertical sidewall. Besides, some polymers can be photo-definable by adding certain additives, such as polyimides, BCB, or SU-8, which can be patterned via exposure to light in standard photolithography processes [39].

For the conductive metal layer of the electrodes, a wide range of metals have been reported, including stainless steel, tungsten, platinum, platinum-iridium alloys, iridium oxide, titanium nitride, gold, silver/ silver chloride, chrome, copper, etc. [39,40]. To coat a conductive layer on the polymer substrate, the metallization techniques should be carefully selected, since polymers are unable to tolerate high temperatures during processing. The metallization of polymers can be performed with physical vapor deposition, such as thermal evaporation, E-beam evaporation, Sputtering [41]. In this process, some potential issues would be introduced, such as thermal stress caused by the large discrepancy of thermal coefficients between metals and polymers, and poor adhesion of polymers to metal. To improve the polymer-metal adhesion, additional processes could be applied, such as introducing an adhesion metal layer [42,43], using chemical adhesion

promoters, annealing [44], plasma pre-treatment of polymer surface [43,45]. To pattern the metal layer, a variety of methods can be used. The wet etching is the most simple one with an appropriate etchant. The resolution of the electrode circuit trace is relatively low by using wet etching. Another way to pattern the electrode circuit traces with high resolution is the lift-off process. A lift-off process is also an option if there is no appropriate etchant for use.

Although many metals can be used as a conductive layer, only gold, platinum, tungsten, iridium, and stainless steel are non-toxic and regularly used in medical devices. Copper, silver/silver-chloride, pure iron are considered toxic, causing severe immune responses, even though they have good electrical conductivity. Since the signals of the action potential are weak, plus a lot of noise, the good electrical conductivity of the interconnect layer is significant to improve the signal quality. To balance the issue, the electrode circuit layer was made of metal with excellent conductivity, such as copper, but it will be encapsulated with a layer of biocompatible metal or polymer around the recording site. This procedure is called electrode modification. For example, electroplating can be used to coat a gold layer on the copper electrode sites [46]. Since most metals will be oxidized and corroded in the brain tissue, more and more neural electrodes were coated with conductive polymers (CP) surrounding the recording electrode sites. The most popular one is Poly(3, 4-ethylenedioxythiophene)-poly(styrenesulfonate) (PEDOT:PSS). Many research reports that the PEDOT:PSS modified electrodes have better electrical characteristics and lower impedance [47,48].

2.4 Applications of Neural Microelectrodes

Recording and stimulating neural potential actions with neural microelectrode arrays is a start point for various applications. Implantable neural microelectrodes, as an important part of brain-machine interfaces (BMIs), are capable of capturing, digitizing, and transferring neural

signals outside of the body with a transmitter [49]. It facilitates our understanding of physiological processes at the cellular level by recording the neurons' activities. Deep brain stimulation (DBS) is a critical application by using neural microelectrode arrays to stimulate deep targets in the brain. To date, DBS has been reported as an effective diagnosis and surgical intervention for patients' neurological diseases, such as essential tremor, Parkinson's disease, dystonia, refractory obsessive-compulsive disorder, depressive disorder, etc. [50,51].

Despite the fact that the neural microelectrode arrays are a powerful tool to study brain functions and treat neurological symptoms, the knowledge of precise neurophysiological mechanisms is limited. Methods of functional imaging such as functional MRI (fMRI), single-photon emission computed tomography (SPECT), and positron emission tomography (PET) can help us unveil the mechanisms by combining them with DBS [52–54]. This combination can reveal the neural activity at the site of stimulation and also provide a global view of the rest of the brain. Functional magnetic resonance imaging (fMRI) is a non-invasive brain imaging technique by mapping the changes in blood supply in the brain activated by certain stimuli. fMRI allows real-time imaging under normal physiological conditions with high spatial and temporal resolution. The blood-oxygen-level-dependent (BOLD) response is a primary form of fMRI to map neural activity due to stimuli in the brain [55]. Compared to PET and SPECT, fMRI is a promising and safer method to map the nervous system due to no risk of exposure to ionizing radiation [53].

Although combining fMRI with DBS has many advantages, the implanted electrode makes fMRI a potentially dangerous technique due to risks associated with heating, magnetic field interactions, induced currents, and the functional disruption of these devices [4,53]. Furthermore, artifacts caused by the metallic material of the implanted electrode may be larger

than the stimulated nucleus, directly leading to the failure of imaging. Therefore, an fMRI-compatible neural microprobe is critical and urgent for neuroscience and medical treatment.

2.5 Implantation Techniques

Although flexible neural microprobes mitigate the unfavorable mechanical mismatch, it is more susceptible to bending and buckling during implantation due to the decrease of stiffness. Implantation of neural microprobes plays a critical role in recording/stimulating performance and minimizing injury and immune response. This is particularly true for the thin planar flexible neural microprobes with a high-aspect-ratio during the insertion. The neural microelectrodes require to be placed near firing neurons to detect extracellular single-unit action potentials. The buckling and bending of the neural probe also lead to a deflection to the target, causing failure of the implantation. Therefore, implantation techniques become more and more important as the neural microprobe becomes more and more flexible. To overcome this challenge, a number of techniques have been developed to assist the implantation of flexible neural microelectrodes.

2.5.1 Removable Rigid Shuttle

Temporarily attaching the flexible probe to a rigid backbone or needle is the most common way to assist the implantation of neural probes. Biodissolvable adhesives can be used between the probe/shuttle (e.g., needle) interfaces during insertion. After insertion, the shuttle can be separated from the microelectrodes by adding water or other fluids [56,57]. Although this is a straightforward way to assist the implantation of flexible electrodes, there are still many drawbacks when using the needle-like shuttle. One difficulty is the adhesion method, in which both too strong and too weak adhesion would influence the performance of the shuttle. A too strong bonding would subsequently prevent the probe from being released, whereas too weak bonding would cause sliding of the probe against the shuttle when surgically manipulated. No

matter which situation occurs, it would affect the accuracy of placement. To overcome this disadvantage, a hole near the tip of the neural microprobe was designed for assembly to a removable needle [38,58]. That allows the shuttle needle to be removed easily and faster. Since there are no recording sites near the hole area, this design requires the microprobe to be implanted deeper, causing additional damage to the deep brain area. In addition, the shuttle structure is normally larger than the neural microprobe, which enlarges the insertion trauma and creates a gap between the recording electrode sites and neural tissue after retraction of the shuttle.

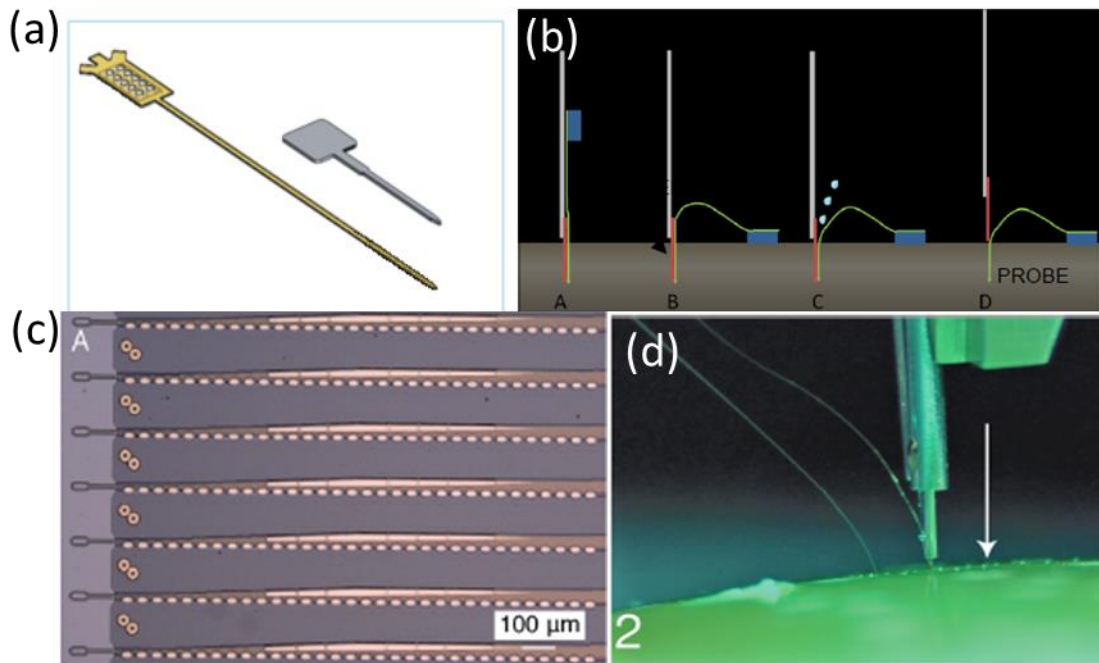


Figure 2.4 Implantation with a removable stiffer shuttle [38,56]. (a) An example of a silicon insertion shuttle, (b) Implantation procedure of neural probe with insertion shuttle, (c) Flexible neural probe with a hole for assembly insertion needle, (d) An inserter for the probe in (c).

2.5.2 Bio-resorbable Polymer Coating

Coating with a bio-resorbable polymer is able to temporarily increase the stiffness of the neural microprobe. Many biocompatible materials can be employed in this situation, including

poly(lactic-co-glycolic acid) (PLGA), polyethylene glycol (PEG), tyrosine-derived polymers, carboxy-methyl-cellulose (CMC), saccharose, silk [59], collagen/gelatin, chitosan, and sucrose/maltose [26,60]. After insertion, those materials are contacted with physiological fluids to be dissolved, and then only the neural probe can be left. However, this method also induces some potential disadvantages. Obviously, the coated polymer increases the cross-section area of the original neural probe, which enlarges the insertion trauma and reduces the integration with neural tissue. Coating expansion due to moisture absorption from brain tissue may cause secondary damage [61]. Furthermore, the dissolution time is directly associated with implantation performance. For example, PEG's fast degradation rate makes it unpractical for long surgical procedures, while a long dissolution time may cause a chronic immune response [62].

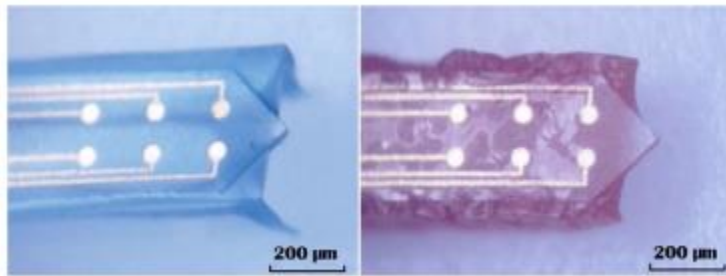


Figure 2.5 An example of coating the bio-resorbable polymer [63].

2.5.3 Mechanically-adaptive Substrate

Mechanically-adaptive substrate whose stiffness changes under a certain condition, such as temperature, light, humidity, etc., can also temporarily increase the stiffness of neural microelectrodes [64]. For example, a thiol-ene/acrylate shape memory polymer was utilized as a substrate of the invasive neural interface, which can be softened by heating from Young's modulus of more than 600 to 6 MPa [65]. Harris et al. [66] developed a kind of polymer nanocomposite whose Young's modulus decreases from 5 GPa to 12 Mpa within 15 minutes

under physiological conditions. These promising outcomes may need to be intensively investigated, especially for long-term neural recording in vivo.

2.5.4 Bio-inspiration Methods

Buckling prevention strategies in nature as inspiration has been reviewed by Sakes [67]. Some strategies can be applied to the flexible probe implantation, such as vibration, guide support, etc. Inspired by the mosquito bite process, Andrew et al. [68] proposed to use a guide structure to aid the implantation of ultra-flexible microprobes. This biomimetic guide successfully raises the critical buckling force of the microprobe to 3.8-fold, leading to a 100% insertion success rate. The plastic guide structure has to be physically removed after use, which may cause secondary damage and interference to the already implanted neural probe.

2.5.5 Reinforcement Layer

Instead of using implantation aids, researchers also modified the structure of the flexible neural microprobe to improve their insertion performance. Kim et al. [69] and Alexandru et al. [70] adopted a compromised method that combines flexible recording sites with a rigid tip to enable penetration. Embedding a thin metal reinforcement metal layer is another good way to attenuate mechanical mismatch while retaining rigid for probe penetration. Fomani et al. [71] adopted gold micro-needles to locally reinforce the implants, as shown in Figure 2.6. Chen et al. [46] designed a long shaft polyimide-based neural probe with a thin chromium impact layer. This method is a compromised way to increase the stiffness of the neural probe while maintaining its flexibility. Importantly, for the long shaft neural microprobe, the reinforcement layer enables the flexible probe to reach a deep target in the brain without any external aids. However, it is a tradeoff to determine the stiffness of the embedded metal layer and the flexibility of the neural probe.

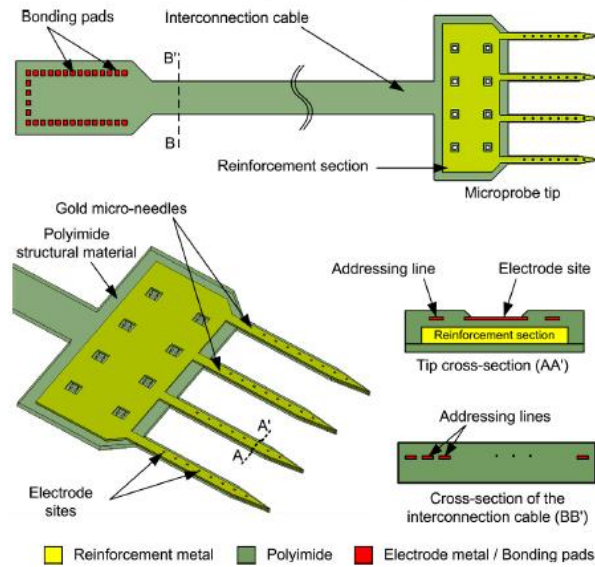


Figure 2.6 An example of a flexible neural probe with the reinforcement layer [71].

2.5.6 Vibration-assisted Insertion

Attaching the neural microprobe to an ultrasonic device to assist its insertion shows a promising way for the implantation of flexible implants [72,73]. This dynamic insertion can effectively improve insertion performance and reduce the generation of microglial and astrocytic than static insertion procedures [74]. Importantly, it also improves the signal collection of the neural probe after the insertion. Since the reported method still uses an ultrasonic-actuated needle-like shuttle to assist the insertion, similar unfavorable consequences of using a removable shuttle would be introduced during insertion, as discussed in Section 2.4.1.

Although only a few numbers of research reports about ultrasonic-assisted insertion for the flexible neural probe, the traditional vibratory assisted rigid needle insertion has been studied for decades, which gives us a lot of useful guides and inspirations. Yang et al. [75] employed a vibratory actuator operating in the kHz range on the microneedle to overcome the structural material limitations, relieve insertion pain, and enhance the efficiency of drug delivery. Huang et

al. [76] presented a piezoelectric vibration-based syringe to reduce the insertion force in the kHz range. The paper indicated that the high-frequency vibration can influence the friction force and cutting force by 28%. Liao et al. [77] reported an ultrasonic device for needle insertion, which can achieve force reduction by 34.5% and deflection reduction by 38.3%. And the higher driving voltage causes lower insertion force. As high frequency increases the mechanical impedance of the vibration system, it is difficult to increase the vibration amplitude in the meanwhile, thereby limiting the further improvement of vibratory insertion. To further improve the insertion performance using ultrasonic vibration, three-dimensional ultrasonic vibration is another promising direction. In our earlier research [78,79], Cai et al. modified the current needle with slots and achieved a longitudinal-flexing vibration on the tip of the needle. The experiment results show that the design can further reduce the insertion force compared with traditional longitudinal vibration. By looking through the influence of ultrasonic vibration on needle insertion, the ultrasonic vibration reduces the insertion force primarily due to a reduction in friction force which is the primary component of the insertion force during insertion. To improve implantation performance, this paper will investigate the possibility of directly driving the planar flexible neural microprobe with a three-dimensional ultrasonic vibration.

2.6 Summary

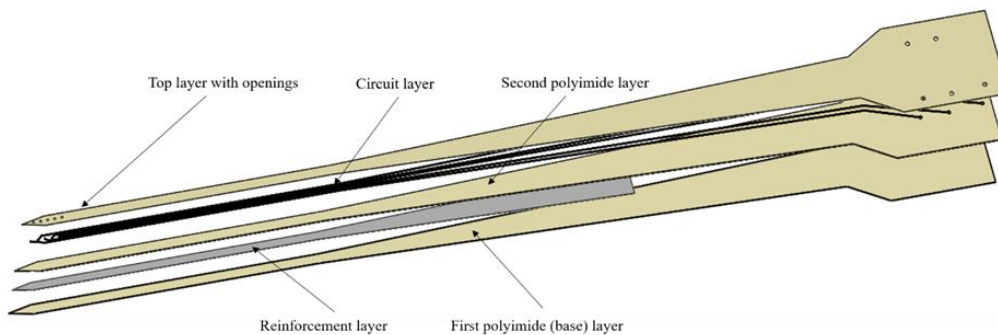


Figure 2.7 Illustration of our proposed flexible neural probe compatible with fMRI.

This chapter provides a brief overview of the development, fabrication, and application of neural microelectrodes. Implantable flexible neural microelectrodes are capable of recording and/or stimulating neuron activities electrically for a long period in the brain. Simultaneously applying DBS and fMRI have been revealed to be a promising method to functionally and unbiasedly map the circuit and network-level connectivity of brain neurons. However, most current neural implants are incompatible with the MRI environment, resulting in unreadable imaging results and potential risks. In this work, therefore, we will present a flexible neural microprobe that can be used with fMRI, as shown in Figure 2.7. The detailed design and fabrication method will be introduced later in Chapter 3, followed by the characterization of the developed neural microprobe in Chapter 4

Although flexible neural microprobes mitigate the unfavorable mechanical mismatch to the brain tissue, it is more susceptible to bending and buckling during implantation due to the decrease of stiffness. The insertion techniques play a significant role in flexible probe implantation, which is also reviewed in this chapter. We found that more research and development on an effective and straightforward implantation method for a variety of flexible neural interfaces is still necessary. Later in Chapters 5 and 6, we present a promising strategy that uses longitudinal and twisting ultrasonic vibration with a bio-dissolvable insertion guide to deliver accurate insertion with minimized tissue damage and deflection.

CHAPTER 3

NEURAL MICROPROBE FABRICATION

This chapter presents the detailed design and fabrication processes of an fMRI-compatible flexible neural microprobe that can be used with fMRI to map the circuit and network-level connectivity of brain neurons. Due to the electrophysiological recording and fMRI compatibility requirements, the fabrication processes are limited to very few feasible solution possibilities. The fabrication processes are studied and discussed in the following sections.

3.1 Materials Selection

To ensure the neural microprobe have good performance and compatibilities, the materials need to be appropriate and comprehensively selected based on their mechanical, chemical, and electromagnetic properties. In this work, polyimide is adopted as the substrate for our fMRI compatible flexible neural microprobe, and chromium, copper, and gold are used for the functional layers.

3.1.1 Polyimide

Polyimide was first invented by Dupont® in the 1960s. Polyimides are thermosetting ring chain polymers constructed from imide monomers. Polyimide is an extremely versatile material that can be modified with different properties by adding chemical additives [80]. The modified polyimide can be conductive or insulating, magnetic or non-magnetic, photosensitive, or non-photosensitive. Polyimides' versatile and excellent properties enable them to be widely applied in the fabrication of MicroElectroMechanical Systems (MEMS) devices, such as the sacrificial

layer, actuators, biometric sensors. It is also easy to manufacture by using microfabrication technology in the cleanroom.

In recent years, many researchers [46,60,81] started to adopt polyimide to fabricate neural implants due to their excellent mechanical, chemical, and biocompatible properties. The relatively low Young's moduli of polyimides (2.3-8.5 GPa) are more closely match the mechanical properties of neural tissues, which can effectively reduce foreign body response of the tissue and micromotion between the microprobe and soft brain tissue. The cured polyimide is also perfectly suited as a dielectric layer in electronics due to its high insulation resistance, dielectric strength, and low moisture uptake. Many studies conclude that polyimides are non-toxic and resistant to organic solvents [82], which facilitates a long life span for the neural microprobe in the animal body. In terms of MRI compatibility, a polyimide-based neural electrode can work well under the MR environment with minimal artifacts.

Many types of commercial polyimide are available on the market, such as Kapton PI-2556, PI2566, PI-2600, PI-2611, etc. In this work, we chose the polyimide Pyralin PI-2611 (HD Microsystems®) as the substrate and insulation layer for our neural microprobe. The chemical structure of a monomer of polyimide PI-2611 is shown in Figure 3.1. The PI-2611 provides high molecular weight and fully aromatic polyimides, which can achieve a thick film with multiple cures. The cured PI-2611 film exhibits a series of desirable properties for neural microprobes, including low stress, low CTE, low moisture uptake, and good ductility, as shown in Table 3.1. The PI-2611 can be very stable over a broad range of temperatures up to 360 °C and has excellent chemical resistance, which enables the PI-2611 to be compatible with most microfabrication processes.

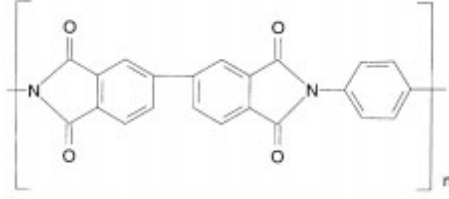


Figure 3.1 The chemical structure of polyimide PI-2611.

Table 3.1 The characteristics of PI-2611 after cure.

	PI-2611	Unit
Tensile strength	350	MPa
Elongation	100	%
Density	1.4	g/cm
Modulus	8.5	GPa
Stress (10 μ m film)	2	MPa
Moisture uptake	0.5	%
Glass transition temperature	360	$^{\circ}$ C
Melting point	None	$^{\circ}$ C
Decomposition temperature	620	$^{\circ}$ C
Coefficient of thermal expansion	3	ppm/ $^{\circ}$ C
Coefficient of thermal conductivity	25×10^{-5}	cal/cm sec $^{\circ}$ C
Dielectric constant (at 1 kHz, 50% RH)	2.9	-

3.1.2 Metals for Neural Microprobes

The metal materials in neural implants play a significant role and should be carefully selected. For safety considerations, all the metal materials have to be non-toxic to cells or be encapsulated with a non-toxic material. The exposed electrode metals are also required to have good corrosion resistance as the brain tissue is a salt solution environment. The degradation of the electrodes caused by the immune response and corrosion results in an increase of impedance and decrease of signal-to-noise ratio (SNR), thereby reducing the quality of signals. The fMRI has a complex and strong magnetic environment that can interact with the metals in the neural microprobe in many ways, causing hazardous conditions, such as force, induced voltage, heating, etc. To eliminate any hazards and reduce imaging artifacts, all metals utilized should be non-magnetic and MRI compatible. To determine the appropriate metals for the neural microprobe,

we investigated the physical and electromagnetic properties of common thin-film metals, as listed in Table 3.2.

Table 3.2 Some material properties of thin-film metals.

Metal	Symbol	Resistivity ($\times 10^{-8}$ $\Omega.m$)	Melting point $^{\circ}C$	CTE ppm/ $^{\circ}C$	Thermal cond. W/m.K	MRI compatibility
Copper	Cu	1.67	1083	19.7	418	Yes
Gold	Au	2.35	1064	14.2	297	Yes
Silver	Ag	1.59	961.8	19.5	429	Yes
Aluminum	Al	2.65	660	23.0	240	Yes
Tungsten	W	2.52	3415	4.5	200	No
Nickel	Ni	6.9	1455	13.3	92	No
Titanium	Ti	55	1667	8.9	22	Yes
Platinum	Pt	10.52	1774	9.0	71	No
Chromium	Cr	12.99	1900	6.3	66	Yes

According to Table 3.2, copper, chromium, and gold are selected in this paper. The circuit trace layer should generate a low impedance to obtain a good recording/stimulation signal quality, which is particularly important for relatively high-frequency signal collection. Copper is a good candidate due to its excellent electrical conductivity and less influence on MRI signal quality and device performance [83]. The adhesion strength between Cu and polyimide is weak, resulting in the failure of copper deposition and patterning. A chromium adhesion layer can be deposited between the two to improve the adhesion performance, because of the higher chemical reactivity of Cr than Cu [43]. Based on Table 3.2, the CTE mismatches of copper (19.7 ppm/ $^{\circ}C$) and polyimide (3 ppm/ $^{\circ}C$) will introduce high thermal stress when the polyimides are curing at 350 $^{\circ}C$. The chromium layer serves as a transitional layer to neutralize the introduced thermal stress due to its intermediate CTE (6.3 ppm/ $^{\circ}C$). These are also the reasons that we select chromium as the reinforcement layer of the neural microprobe, which can be deposited and patterned easily. The copper ions may also migrate into the polyimide during the fabrication process, causing a

circuit shorting. The Cr layer also behaves as a barrier to avoid the shorting circuit. Although copper has excellent electrical conductivity, it is not a good biocompatible metal and is easy to be corroded in a salt solution environment. Gold exhibits excellent biocompatibility and electrical conductivity. The coated gold on the medical implant surface can reduce immune response and improve corrosion resistance. Therefore, gold is employed to encapsulate the copper electrode sites to improve biocompatibility and corrosion resistance.

3.2 Design of Neural Microprobe

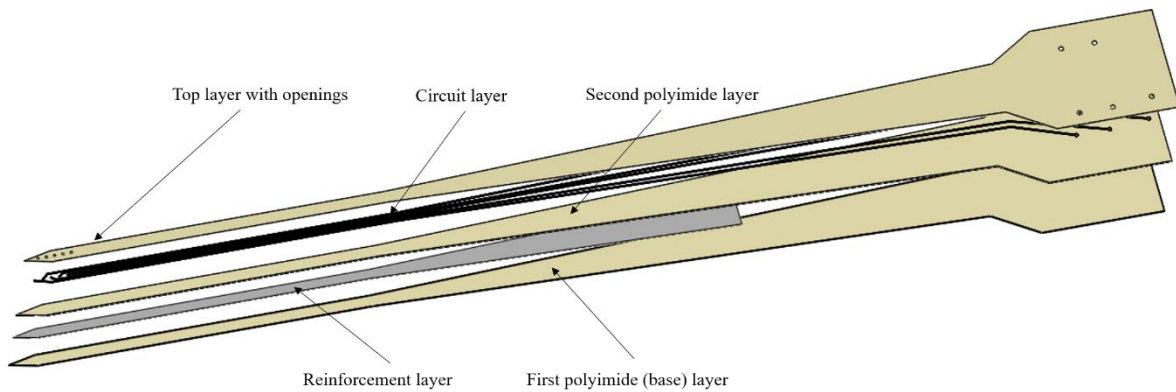


Figure 3.2 Structure of our flexible and fMRI compatible neural probe.

Figure 3.2 shows the concept design of our fMRI compatible flexible neural microprobe. The neural microprobe consists of five layers. Figure 3.3 shows a graphical depiction of the processing procedure for our neural microprobe manufactured in the cleanroom [84]. Three polyimide layers are used as the substrate and encapsulating layers. A 200 nm thick Cr reinforcement layer is patterned as a needle shape to increase the stiffness of the neural microprobe and assist the penetration while retaining good flexibility. A metal stack [Cr/Cu/Au (100 nm/ 700 nm/ 100 nm)] is deposited and patterned as the circuit trace layer followed by a 4 μm polyimide layer to encapsulate the circuit layer. Openings are created on the top polyimide layer to expose the recording electrode sites and contact pads. Electrode modification is conducted

to encapsulate the exposed electrodes and contact pads as well as to improve the signal quality. To pattern the features, a total of three 5” masks are designed and fabricated. The details of fabrication procedures are presented in the following sections.

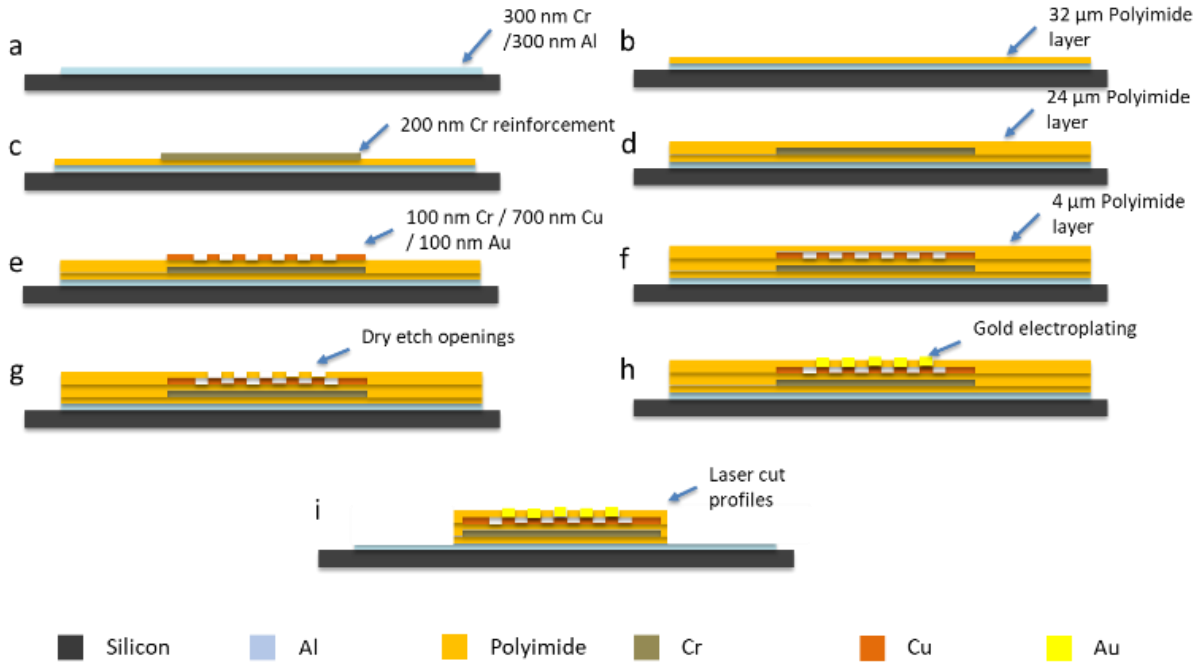


Figure 3.3 Processing flow of the neural microprobes fabrication at NNF.

3.3 Microfabrication Procedures

In this paper, the neural microprobes were fabricated on a 4” single-side polished silicon wafer. The wafer is P-type, <100> crystal orientation, and 500 μm in thickness. The detailed fabrication procedures are presented below.

3.3.1 Sacrificial Layer

To easily release the neural microprobes after fabrication, a 300 nm thick Cr layer followed by a 300 nm thick Al sacrificial layer was initially sputter deposited on the wafer, as shown in Figure 3.3 (a). Although the individual chromium layer is also able to serve as the

sacrificial layer, it has to be immersed into a harsh acid solution for a long period to remove all the chromium. This procedure would attack already patterned metals and shorten the life span of the neural microprobes. In our case, anodic metal dissolution with sodium chloride solution can be employed to dissolve the Al sacrificial layer, which makes the process faster and compatible with a wide range of materials. While the aluminum is used as a sacrificial layer for microprobes release, the chromium layer ensures the electrical contact to avoid incomplete release and get better adhesion between silicon wafer and aluminum.

The DC sputtering was used to deposit the chromium and aluminum, which can obtain a uniform metal layer and better adhesion. The DC sputter equipment in our NCSU Nanofabrication Facility (NNF) is shown in Figure 3.4. After loading the wafers, the sputter chamber was vacuumed to a pressure below 1.1×10^{-6} Torr. According to the sputtering parameter testings, the deposition rate of the chromium and aluminum thin metal layers are 4.97 nm/min and 3.75 nm/min, respectively. The deposition thickness can be precisely controlled based on the deposition rate and time. We performed four minutes of pre-sputtering before the actual deposition to remove MRI incompatible contaminant metals in the sputter chamber. The wafer with Cr/Al sacrificial layer deposition is shown in Figure 3.5.



Figure 3.4 Photo of the DC sputter tool.

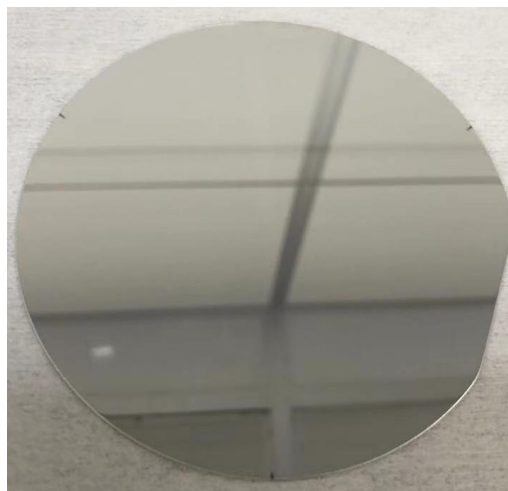


Figure 3.5 Photo of the Cr/Al sacrificial layer deposited on the wafer.

3.3.2 First Polyimide Layer

A 32 μm thick polyimide film (PI-2611, HD Microsystems®) was then spin-coated, soft-baked, and cured on top of the aluminum, which forms the base of the neural microprobe, as shown in Figure 3.3 (b). Before coating the polyimide, oxygen plasma treatment was conducted on March® Asher, as shown in Figure 3.6 (a), to make the surface hydrophilic, thereby increasing

the adhesion strength between Al and polyimide. In addition, the organosilane adhesion promoter VM652 was also used to strengthen metallization adhesion, which requires an oxide with which to bind. The coating thickness of the polyimide layer directly depends on the spin speed and time. Longer spinning time improves the coating uniformity but reduces the film thickness. Figure 3.7 shows the polyimide film thicknesses obtained with various spin speeds on the silicon wafer. Curing the PI-2611 requires a soft-bake on a hotplate followed by a full cure. The full cure is performed above 350 °C using TMS Blue-M programmable oven, as shown in Figure 3.6 (b), to convert the polyamic acid precursor into a fully aromatic, insoluble polyimide film and drive off the NMP(N-Methyl-2-pyrrolidone) solvent carrier. The curing process should be performed in inert nitrogen ambient. Otherwise, the polyimide will crack and turn to brown color due to oxidation. After full curing, the thickness of the polyimide film will be reduced to approximately 70%-80% before cure, as shown in Figure 3.7.

(a)



(b)



Figure 3.6 (a) March Asher, (b) TMS Blue-M programmable oven.

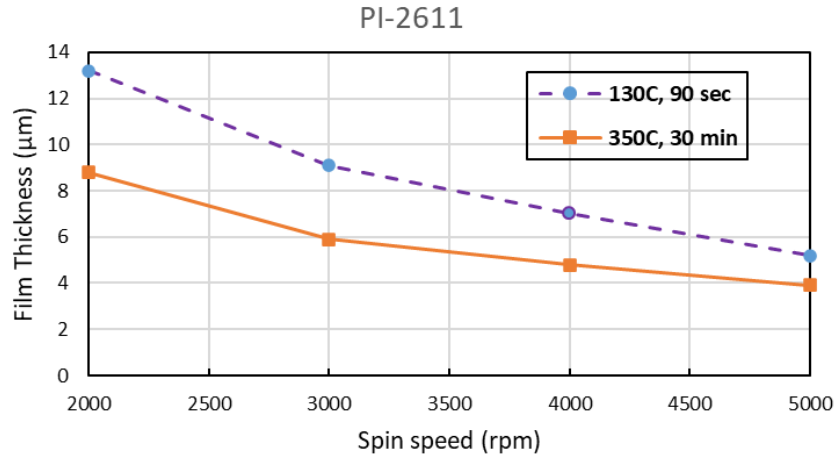


Figure 3.7 Spin speed curve of polyimide PI-2611.

Although PI-2611 has a high degree of viscosity that allows the obtention of thick film, too thick coating before curing would eventually result in a complete failure to cure due to NMP (N-Methyl-2-pyrrolidone) trapping in the film, as shown in Figure 3.8. To achieve a total thickness of 32 µm, four 8 µm polyimide sub-layers were coated with a full cure. When performing multiple cures, each 5°C lowered than the previous baking temperature is required to prevent any possible outgassing. Importantly, an oxygen plasma pretreatment is applied to achieve stronger adhesion between two polyimide sublayers. Otherwise, it would result in delayering of two full cured polyimide layers [85], reducing the neural microprobe life. Figure 3.9 shows the four stages of a fully cured polyimide film. It can be found that a visible ring occurs at the edge of the wafer, resulting from the uneven coating on the edge. Since the spin coating makes the film thicker on the edge than on the center, an edge bead removal or backside rinse would be recommended during the spin coating. Because of no crucial features near the edge, we did not apply the edge bead removal to our work.

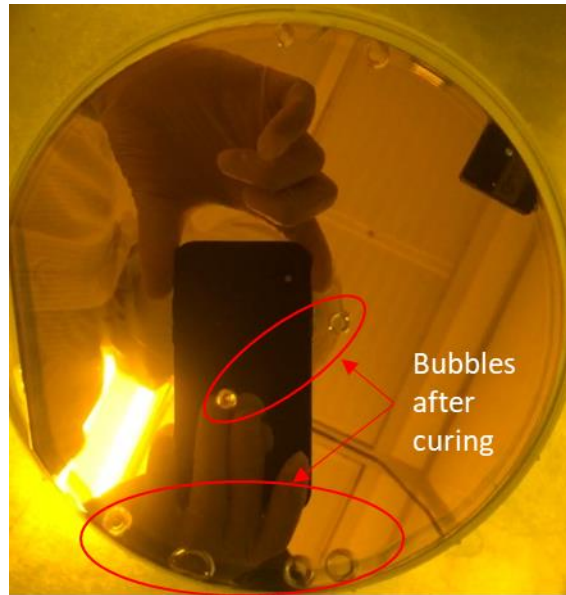


Figure 3.8 Photo of the failed polyimide coating.

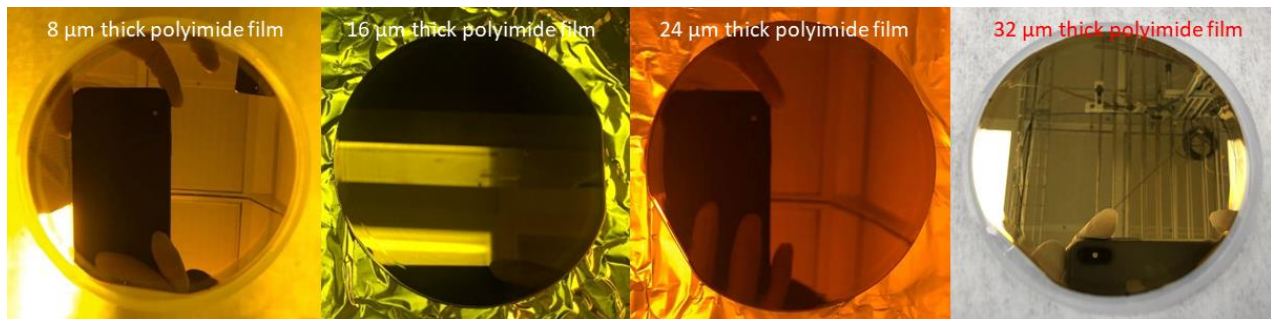


Figure 3.9 Photo of the four-stages full cured polyimide layer.

3.3.3 Reinforcement layer

To improve the stiffness of the microprobe while maintaining its flexibility, a 200 nm thick Cr layer was deposited as a reinforcement layer and patterned as a needle shape, as shown in Figure 3.3 (c). Prior to the deposition, low-pressure oxygen plasma treatment was applied to improve the mechanical adhesion of the metallization layer. The oxygen plasma pretreatment is able to significantly increase the surface roughness, surface free energy value, and decrease the contact angle of polyimide [45]. Then, a dehydration bake was performed on the 115 °C hot plate

for 3 minutes to remove the moisture absorption of the cured polyimide. The reinforcement layer deposition was also done in the DC sputter shown in Figure 3.4. A dummy deposition was conducted before the actual deposition to seal the metal contamination in the DC sputter chamber to ensure no MRI incompatible metals were exposed. The deposition rate of Cr is 4.97 nm/min, and a total of 45 minutes of deposition was performed, including 5 minutes pre-deposition. The deposited 200 nm thick reinforcement Cr layer is shown in Figure 3.10.

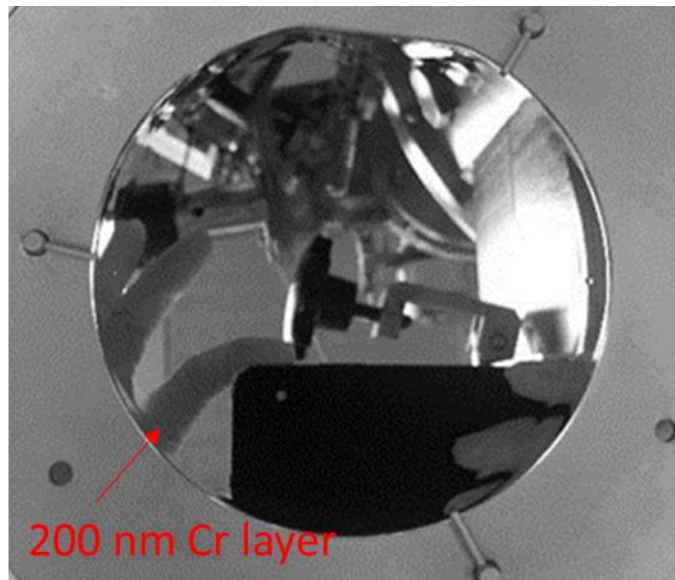


Figure 3.10 Photo of deposited Cr layer on the polyimide base.

Wet etching with masking resist was adopted to pattern the reinforcement layer. The S1813 (Microposit®) was employed as the masking resist, a photo-definable polymer and suitable for most wet etching processes. The S1813 (Microposit®) can be used as either the positive or the negative photoresist. In patterning the reinforcement layer, the S1813 was used as a negative photoresist with an image reversal process. The image reversed S1813 photoresist can be easily removed with acetone and IPA to ensure that no photoresist residuals affect the adhesion to the next polyimide layer. HDMS (Hexamethyldisilazane) was vapor primed to make the substrate

surface hydrophobic to provide excellent wetting and adhesion to photoresists. The HDMS pretreatment was performed directly in the primer oven (YES® ClassOne), as shown in Figure 3.11 (a). The photolithography was then conducted on the contact aligner MA6 (Suss MicroTec®) with i-line exposure optics (365 nm UV light), as shown in Figure 3.11(b). After first pattern exposure, an image reversal baking was performed in the ammonia environment using the primer oven (YES® ClassOne), followed by five seconds of flood exposure to make the initially unexposed area to be developable. The development process was done using the MF-319 (Microposit®) developer that is specifically formulated for use with Microposit S1800 series photoresists. The CR-7S (KMG Electronic Chemicals®) chrome etchant that can operate at room temperature with a high etching rate was chosen to pattern the reinforcement Cr layer. The patterned needle shape reinforcement layer is shown in Figure 3.12.

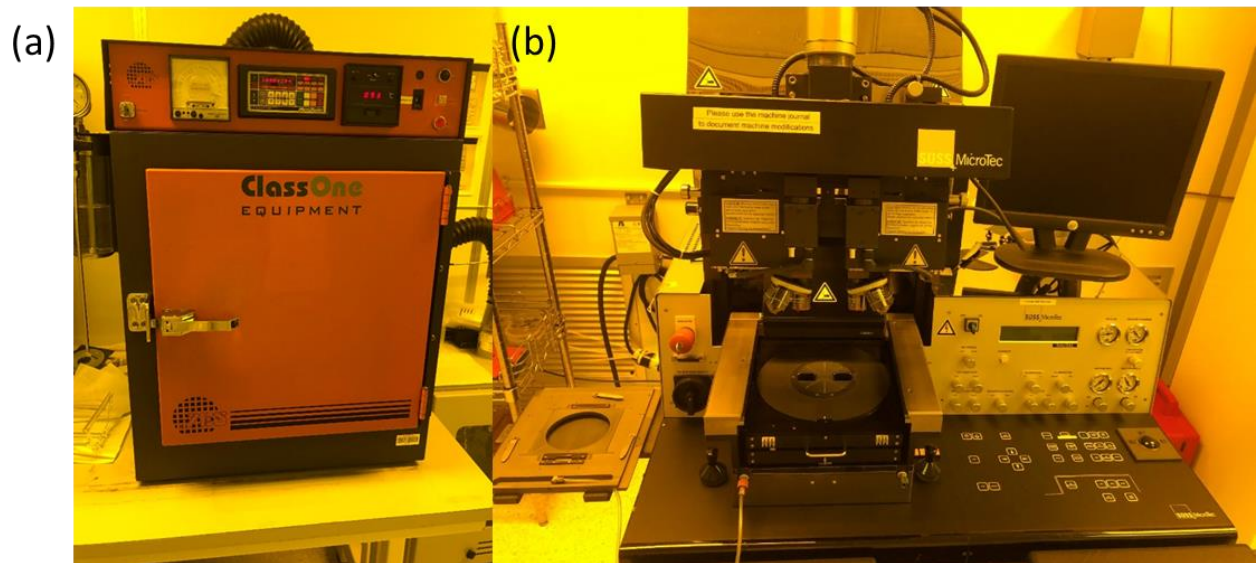


Figure 3.11 (a) YES® ClassOne primer oven, (b) MA6 (Suss MicroTec) contact aligner.

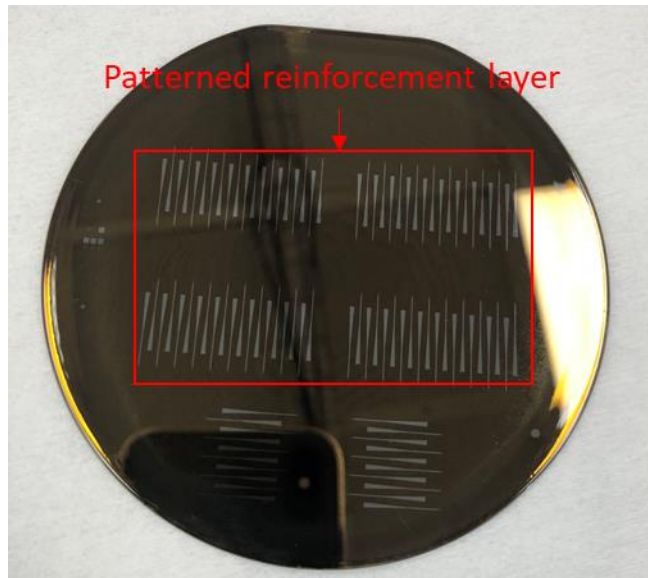


Figure 3.12 Photo of patterned Cr reinforcement layer.

3.3.4 Second Polyimide Layer

The second 24 μm thick polyimide layer (PI-2611, HD Microsystems®), which separates the reinforcement layer and circuit layer, was spun on and likewise cured, as shown in Figure 3.3 (d). The VM652 promoter was spin-dried on the chromium reinforcement layer before polyimide coating. The completed 24 μm thick polyimide layer was achieved by three 8 μm thick polyimide sub-layers with full cure, as shown in Figure 3.13. We designed the unbalanced thickness of the two polyimide layers structure to counteract the bending of the neural probe after releasing due to the residual thermal stress.

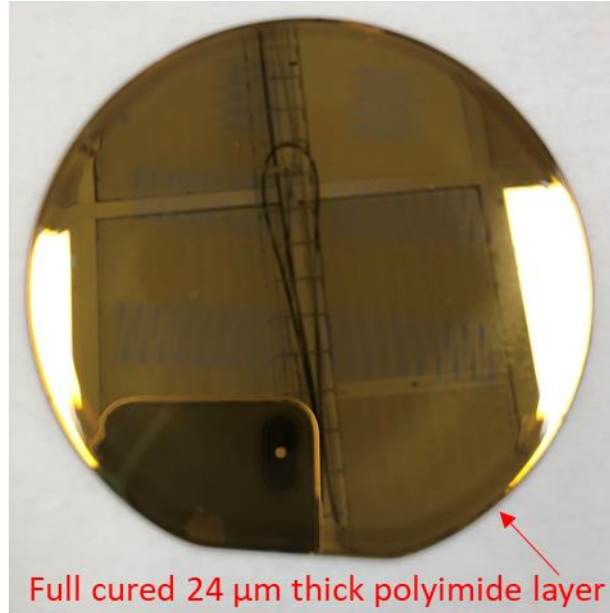


Figure 3.13 Photo of the second 24 μm thick polyimide layer.

3.3.5 Circuit Trace Layer

A metal stack [Cr/Cu/Au (100/700/100 nm)] was sequentially deposited using E-beam evaporation, followed by a lift-off process to pattern the circuit trace layer, as shown in Figure 3.3 (e). While the 100 nm thick chromium layer was used as an adhesion layer for copper, an oxygen plasma treatment is still needed to enhance the adhesion of polyimide metallization, which increases the surface roughness, produces functional groups that facilitate bonding to the metal, and increase surface free energy [37]. The 100 nm thin layer of gold deposited on copper acts as the gold electroplating seed layer to improve the corrosion resistance of copper. A 3.7 μm SPR220 photoresist was spin-coated with an image reversal process to create a retrograde resist profile that provides good separation within the deposited metal thin film. The thickness ratio between the photoresist to the metal stack is about 4:1. The E-beam evaporation was performed in Thermionics® VE-100 Electron Beam Evaporator, which provides a directional metal deposition

for an easier lift-off process. The patterned circuit trace layer with a lift-off process is shown in Figure 3.14.

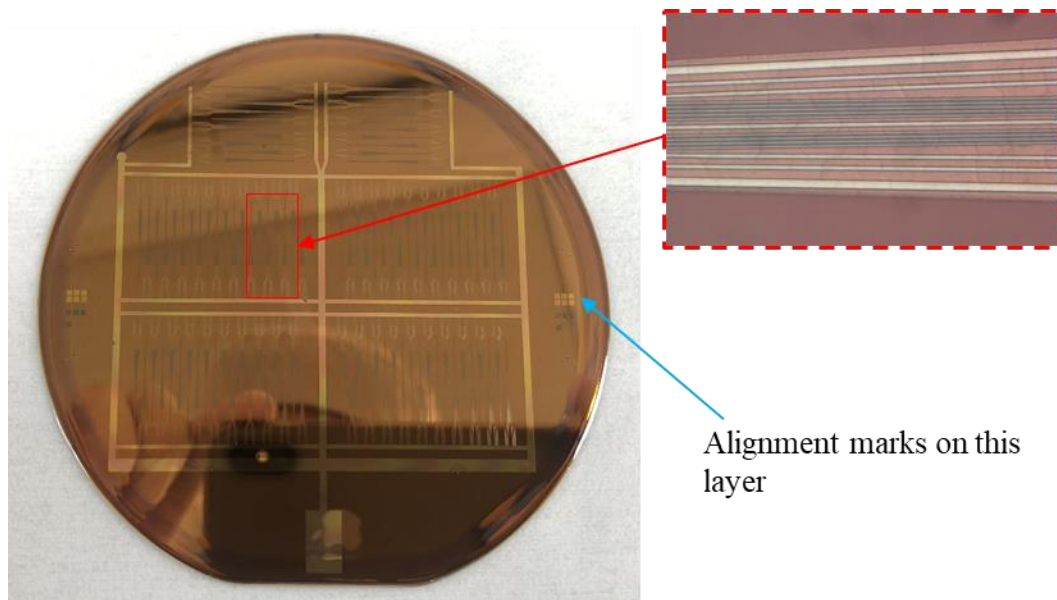


Figure 3.14 Photo of patterned circuit traces layer with a lift-off process.

To fabricate the circuit trace layer, both the wet etching process and the lift-off process are tested in order to obtain high resolution. Although the wet etching process is easier to perform, it is difficult to precisely control the etching rate and depth. Importantly, most chromium etchants (e.g., Transene® Chromium Cermet Etchant TFE) compatible with copper are incompatible with a positive photoresist. While the initial patterned top metal layers can be used as a hard mask for wet etching the bottom chromium layer, the residual positive photoresist would be attacked and stuck to the surface, which is more difficult to remove after dried, as shown in Figure 3.15. Furthermore, in the wet etching process, the metal stack was firstly sputter-deposited followed by photolithography with S1813 photoresist, resulting in no alignment marks created for the next layer patterning, as shown in Figure 3.15. To pattern the top layer, only the alignment marks on the reinforcement layer can be used. However, the thick polyimide film between the

reinforcement layer and top layer increases the alignment difficulty and reduces the accuracy due to the refraction.

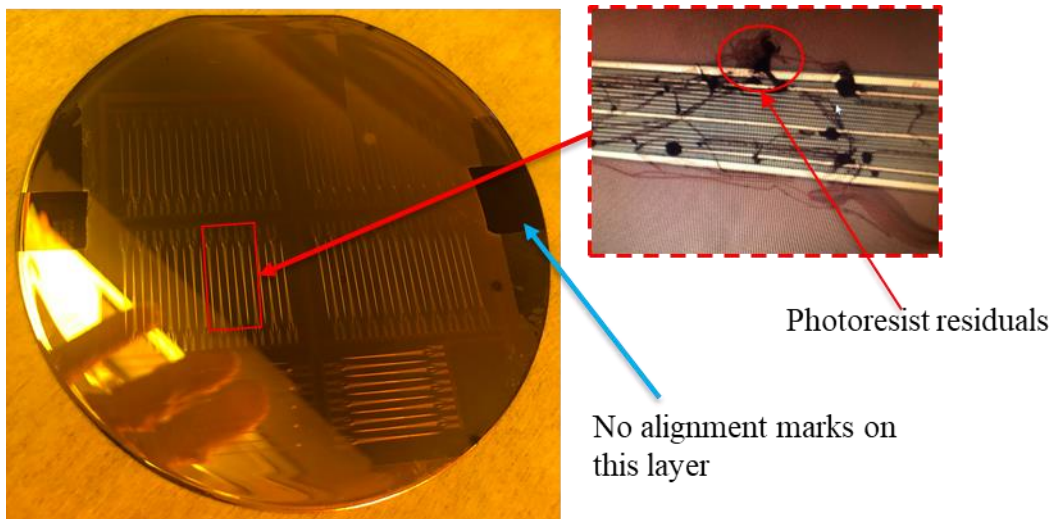


Figure 3.15 Photo of deposited Cr/Cu circuit layer.

3.3.6 Third Polyimide Layer

The third 4 μm thick polyimide layer (PI-2611, HD Microsystems®) was coated to encapsulate the circuit layer, as shown in Figure 3.3 (f). To obtain a better coating uniformity, a longer spin coating time was set. The spin coating parameters were explored on a dummy wafer to get the spin speed curve. The film thickness after cured was measured by the Dektak®150 surface profilometer. The relationship between the film thickness and spin speed for 45 seconds spinning time is shown in Figure 3.16. The third polyimide layer was soft-baked, followed by a fully cured similar to the previous polyimide cure steps. The final 4 μm thick polyimide layer is shown in Figure 3.17.

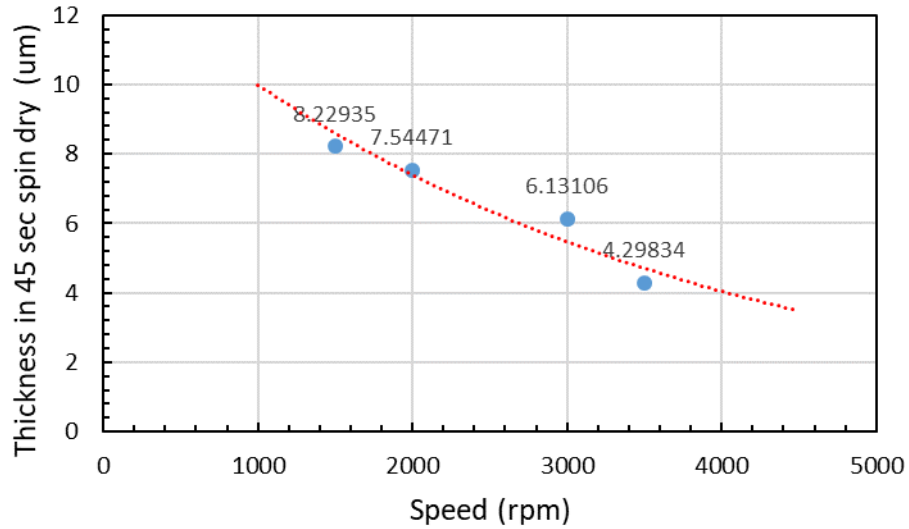


Figure 3.16 The spin curve of polyimide PI-2611 coated for 45 seconds.

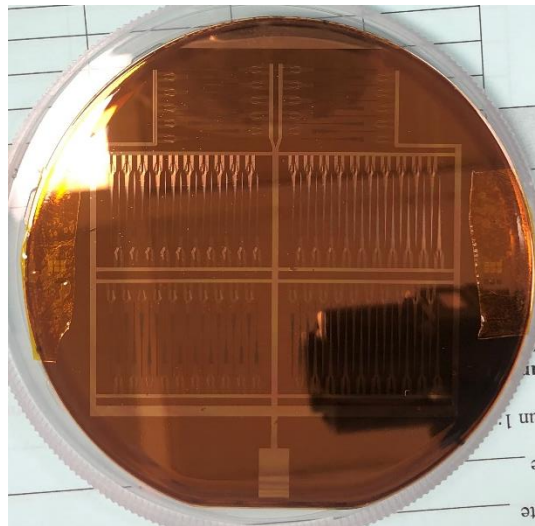


Figure 3.17 Photo of the third polyimide layer.

3.3.7 Dry Etching Openings

Dry etching using O_2 gas alone or in combination with CF_4 [86], CHF_3 [87], SF_6 [88,89] gases is the most effective way to remove or etch polyimide. In this work, the electrode sites, vias, and contact pads on the top polyimide layer were etched in a reactive ion etching (RIE) etching step with mixtures of O_2 and CHF_3 gasses. Oxford NGP80 RIE etcher was used, as shown in

Figure 3.18. Lower chamber pressure was reported to get more verticle sidewalls while reducing the etching rate [90]. The combination ratio of gases also influences the etching rate and quality. A lower mixing ratio of CHF_3 would cause a more verticle sidewall [90], while it reduces the etching rate. After balancing the etching rate and quality, in this work, the chamber pressure is set to 100 mTorr with an etch gas composition of 80% oxygen and 20% CHF_3 .

To dry etch the 4 μm thick polyimide, a hard mask is required. Some metal masks, such as Al, Ni, and non-metal masks, such as silicon oxide, silicon carbide, and silicon nitride [91], have been reported to be suitable for the hard mask of polyimide dry etching. Although the silicon oxide mask generates lower residual stress and better adhesion, depositing silicon dioxide on the polyimide requires a low processing temperature due to the relatively low glass transition temperature of PI-2611. Patterning the SiO_2 hard mask with wet etching requires an HF-based solution which will attack the Al sacrificial layer. A 200 nm thick Al mask was deposited in the DC sputter and patterned using the wet etching technique. The adhesion between the Al and polyimide was tested on a dummy wafer using a simple peeling off test, showing that the adhesion strength is sufficient without using an adhesion layer. The selectivity of the Al mask to the polyimide is about 1:30 in our dry etching condition. The total etching time is about 15 minutes. The openings after dry etching are shown in Figure 3.19.



Figure 3.18 Oxford NGP80 RIE etcher.

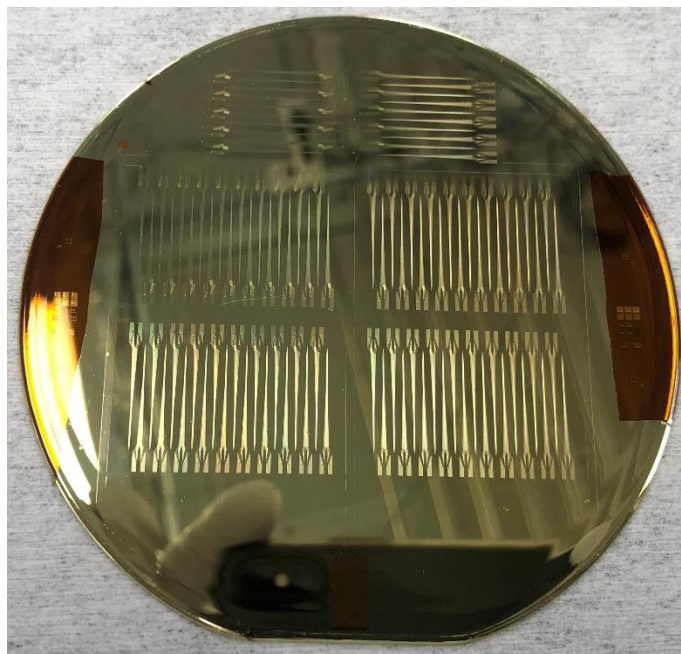


Figure 3.19 Photo of etched polyimide openings with the Al mask.

3.3.8 Gold Electroplating

After etching the openings, the exposed electrode sites are below the top polyimide layer, resulting in bad contact with brain tissues. Gold electroplating is performed in this paper to create a 3D mushroom shape coating above the top polyimide layer, as shown in Figure 3.20. Compared to other deposition methods, electroplating is able to obtain a thicker coating up to several microns to entirely fill in the deep openings (4 μm). Electroplating is a maskless process, which is difficult to achieve by other physical deposition methods. Importantly, the electroplated gold surface is rougher and more porous [92], increasing the effective contact area between the electrodes and tissues. That can reduce the electrode impedance and increase the electrode sensitivity.

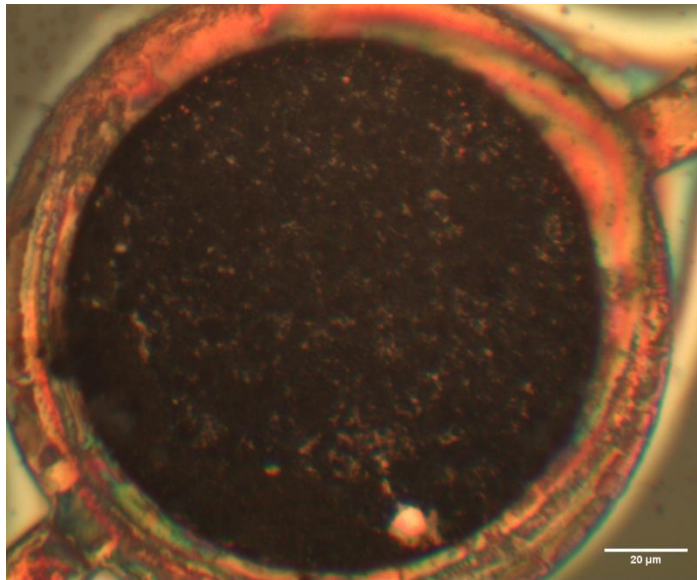


Figure 3.20 Electroplated gold 3D mushroom-shaped electrode site.

The electroplating was performed using a housemade electroplating device with 24K gold electroplating solution, as shown in Figure 3.21. A constant positive potential was applied to the platinized titanium anode, and the working end (cathode) was connected to the wafer common electrode end. The electroplating time is related to the applied voltage. Too high power will

generate lots of bubbles around the electrode sites during electroplating. The bombardment of the bubbles would cause the polyimide to detach around the electrode sites. In this work, we applied 2.7 V constant potential to the anode for 15 minutes.

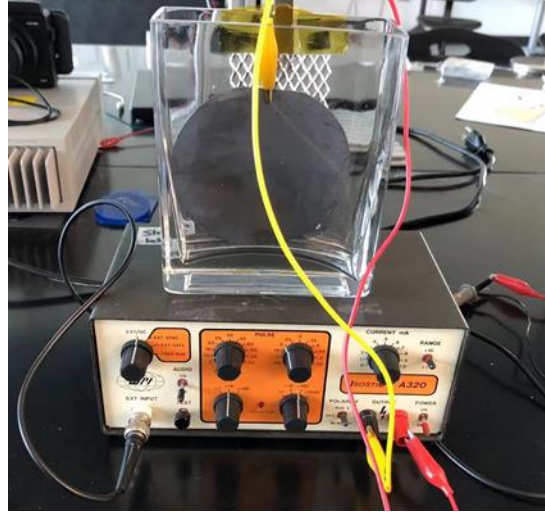


Figure 3.21 Setup of the homemade gold electroplating tool.

3.3.9 Laser Ablation of the Neural Microprobe Profile

To define the profile of the neural microprobes that is about 60 μm in thickness, laser ablation was used to remove all unnecessary areas and expose the sacrificial layer. Even though polyimides are commonly removed by dry etching techniques, it is difficult to apply to our case due to the large thickness. To deep dry etch the 60 μm thick polyimide using the DRIE tool, a thick hard mask is required. It is challenging to deposit several microns thick metal or oxide hard masks using the physical deposition method. Using PECVD is a good way to deposit a few microns of a silicon oxide film. But, to pattern such thick oxide hard mask, most of the wet etching solutions, such as HF, buffered oxide etch (BOE) [89], would attack the Al sacrificial layer, resulting in the failure of the fabrication. Although dry etching also can pattern the silicon oxide hard mask, that still needs a very thick mask for dry etching the silicon oxide hard mask. Therefore,

in this work, we use the UV laser ablation to remove the thick polyimide without using an additional physical mask. After laser cutting, carbonization residues are left on the edge of the microprobe, as shown in Figure 3.22. We found that the carbonization line is conductive, which may cause a shorting when bonding the neural microprobe to the PCB. Therefore, a clean process was performed after releasing the microprobe from the wafer.

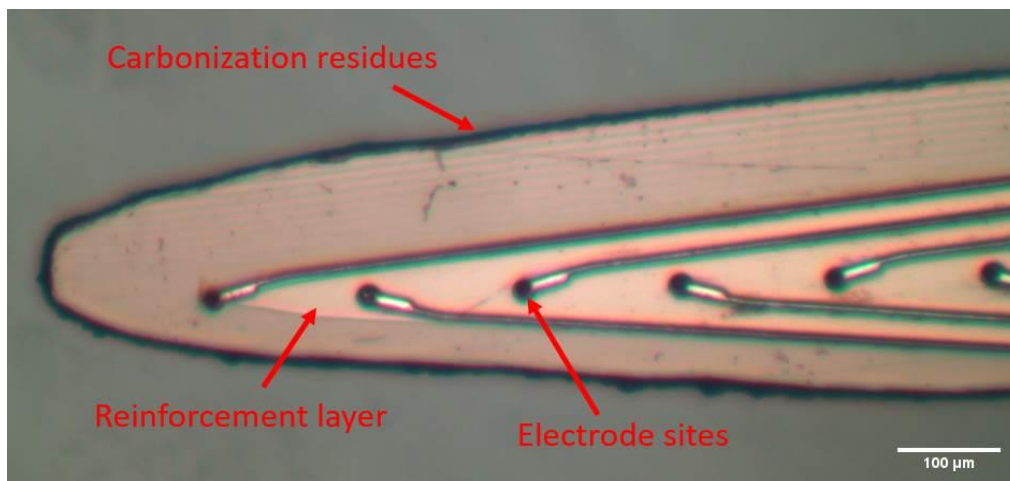


Figure 3.22 Carbonization line on the edge of the neural microprobe.

3.3.10 Microprobes Releasing

Finally, the neural microprobes were released by the anodic dissolution of sacrificial aluminum. The process is isotropic, a lot faster, and environment-friendly. The selectivity of the material removal is adjustable by choosing the appropriate salt solution and applied potential. For our case (Cr/Al), the wafer needs to be immersed in a sodium chloride solution (~2% NaCl) with a Pt counter electrode. Constant positive potential is applied to the aluminum layer (0.1-0.8 V, 0.5 V preferred) by a constant laboratory voltage. We use the same setup as the gold electroplating for the electrochemical release. The released neural microprobes are shown in Figure 3.23.



Figure 3.23 Photo of a fabricated flexible neural microprobe after releasing.

3.4 Microprobe Packaging

The released neural microprobe was packaged with a custom-designed printed circuit board (PCB) connecting to an Omnetic® connector, as shown in Figure 3.24. We found that a carbonization line (See Figure 3.22) on the edge of the microprobe caused by laser ablation is conductive, which would cause a circuit shorting when bonding the neural microprobe to the PCB. A clean process with acetone and IPA was performed after releasing the microprobe from the wafer. Since it is still difficult to be removed, the insulated epoxy was dip-coated on the edge to prevent shorting. The neural microprobe was wire-bonded to the PCB using Westbond 7476E wedge-wedge bonder with 1 mil gold wire. The bonding area is also sealed using epoxy after bonding, as shown in Figure 3.24.

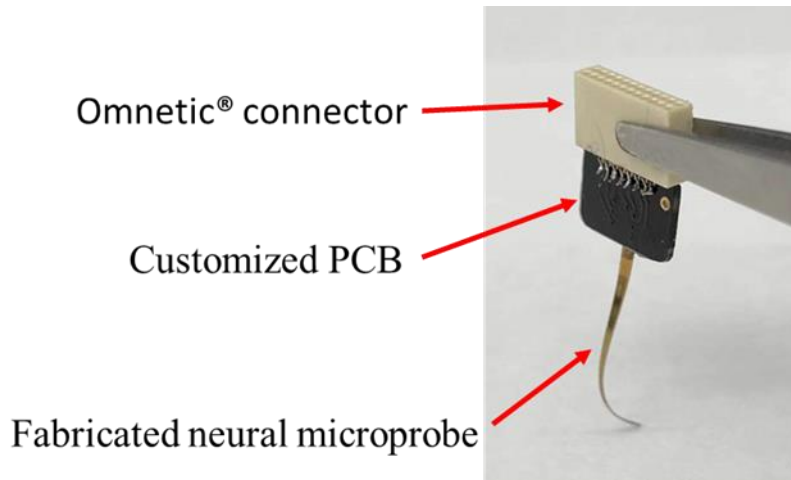


Figure 3.24 Illustration of the PCB for connecting the neural microprobe and Omnetic connector.

3.5 Summary

This chapter presents the design and the fabrication processes of our designed MRI-compatible flexible neural microprobe that can be used under fMRI to map the brain and neural functions system. The materials of the neural microprobe are carefully selected to minimize the MRI artifacts. Polyimide was adopted for the substrate of the neural microprobe, which has good biocompatibility and a relatively lower Young's modulus. A 200 nm chromium reinforcement layer was embedded in the probe to attenuate its implantation stiffness while remaining flexible. Gold electroplating was employed to modify the electrode sites to improve the signal quality and sensitivity. The neural microprobe was fabricated in our NNF cleanroom and bonded to a customized PCB. In the next chapter, the characterization of the fabricated neural microprobes is presented.

CHAPTER 4

CHARACTERIZATION OF NEURAL MICROPROBE

In this chapter, characterization of the fabricated neural microprobe is presented. Scanning electron microscopy (SEM) measurements, electrochemical impedance spectroscopy (EIS) measurement, and mechanical testing were performed to evaluate the mechanical and electrochemical properties of our fabricated flexible neural microprobes.

4.1 Scanning Electron Microscopy (SEM) Measurement

Scanning electron microscopy (SEM) measurements were performed on Thermo Scientific™ Helios 5 Hydra CX DualBeam to structurally evaluate the fabricated neural microprobe. The SEM images of the top view and detailed views of the neural microprobe are shown in Figure 4.1. In Figure 4.1 (a), no charge drift on the edge of the neural microprobe (bright color region) was observed during SEM, which also confirms the carbonation residue is electrically conductive caused by the laser ablation of polyimide. In Figure 4.1(b), an overburning can be observed on the top edge of the neural microprobe. That is because the laser ablation focused on the top of the neural microprobe, and the top polyimide layer is also thinner (4 μm) than other polyimide layers. Some additional fine-tuned laser ablation parameter needs to be further investigated.

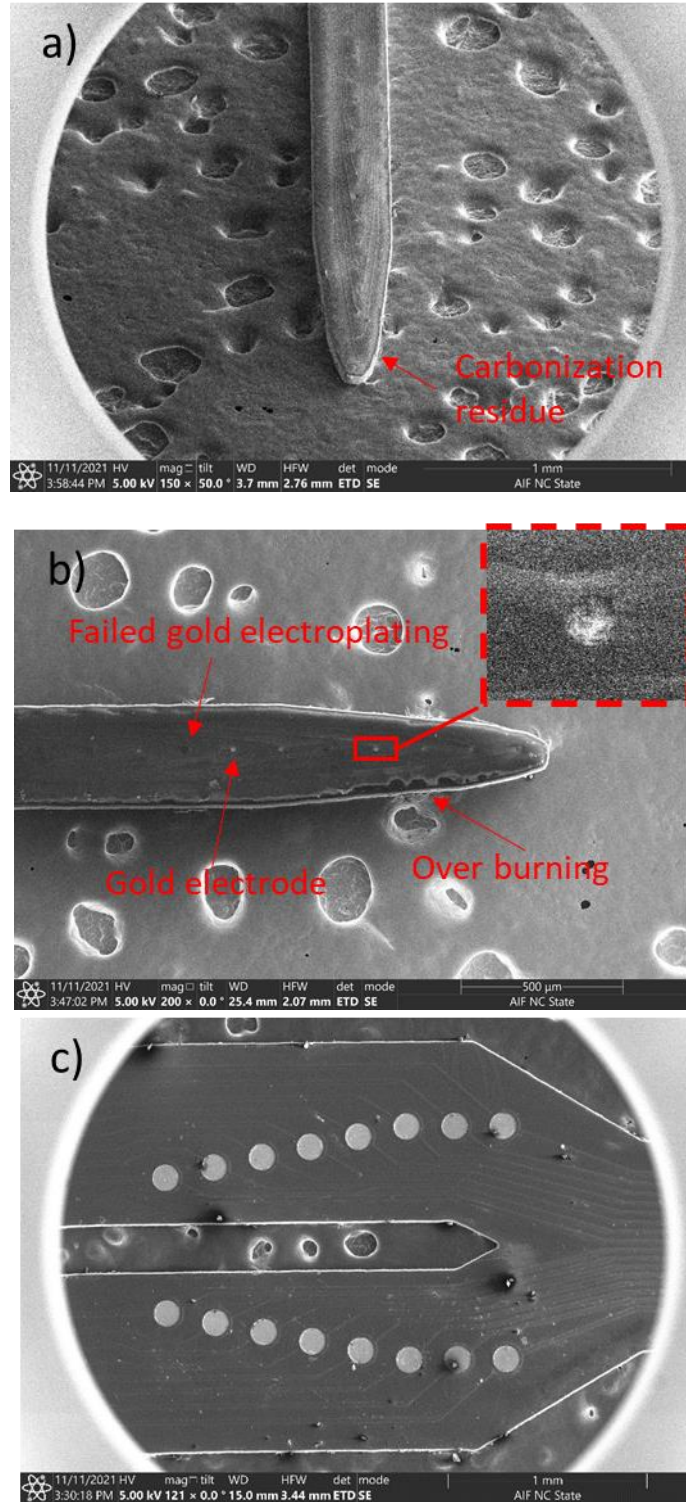


Figure 4.1 The SEM images of the top view of the neural microprobe.

Figure 4.1(b) shows the 3D mushroom-shaped gold electrode over the 4 μ m step of the polyimide encapsulation layer. The gold electroplating is a maskless process, capable of achieving a thicker gold deposition (4 μ m). The electroplated gold electrodes have a rougher and porous surface, which can significantly reduce the impedance and improve the measurement selectivity due to the increased surface area. We also found some failed gold electroplating regions on the neural microprobe, as shown in Figure 4.1(b). Simple peel-off experiments were conducted using Kapton® tape, which shows a weak adhesion of the electroplated gold due to the dry-etching polymeric residues left on the surface. Some chemical post-etch residue removers are needed in the future to remove all the residues before gold electroplating [71]. Figure 4.1(c) shows the detailed view of the contact pads of the microprobe.

Energy-dispersive x-ray spectroscopy (EDS) was also performed during SEM measurements to chemically evaluate the element composition on the surface of the neural microprobe, as shown in Figure 4.2. The measuring area was selected around the electrode site, as shown in Figure 4.2. The EDS analysis shows that there is no copper (Cu) element detected on the surface after the electroplating. This also confirms that the copper electrodes are entirely encapsulated by gold after electroplating, avoiding the corrosion of the copper after implantation. The EDS results reveal that only three major elements, carbon (C), oxygen (O), and gold (Au), were detected during the EDS. Carbon (C) is the most prevalent element on the surface of the neural microprobe with a weight percentage of 74.1%. All of the exposed three elements (C, O, Au) are biocompatible and no MR-incompatible elements exist on the neural probe.

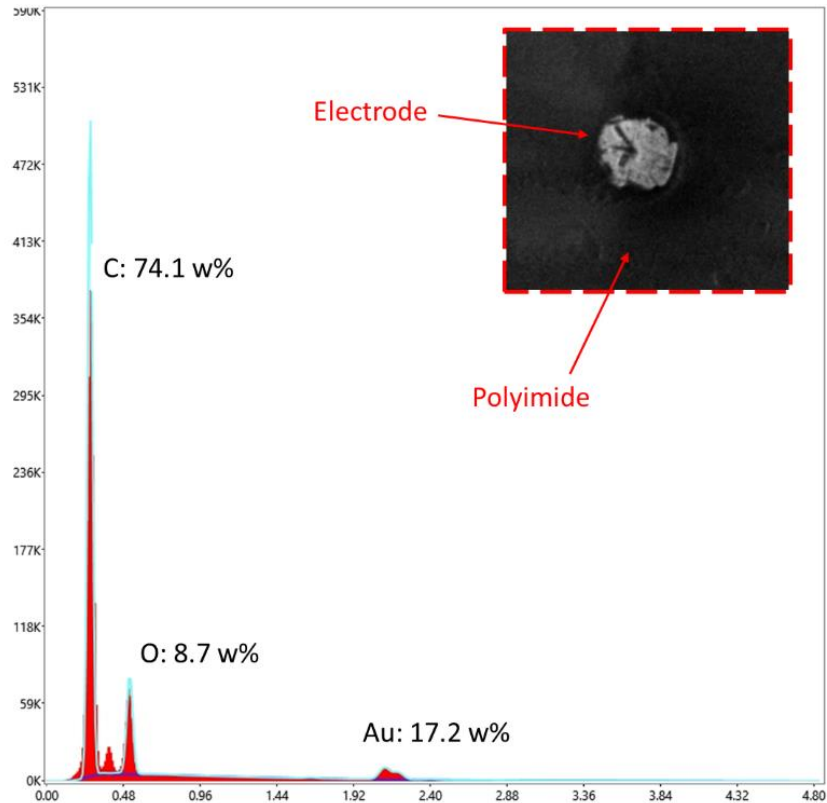


Figure 4.2 The EDS results of the neural microprobe.

4.2 Electrochemical Impedance Spectroscopy Measurement

Electrochemical impedance spectroscopy measurements were performed with a NanoZ® impedance tester in 0.9% saline electrolyte, as shown in Figure 4.3. A sinusoidal signal with a frequency between 100 Hz and 5,000 Hz was applied, and the average impedance measurement results of channels are shown in Table 4.1. Particularly, the impedance at 1 kHz that we are interested in is 1.033 MOhm with a phase of -89.3° , which is comparable to the reported existing neural microprobes. The low impedance of our fabricated neural microprobe allows it for DBS and action potential recordings.

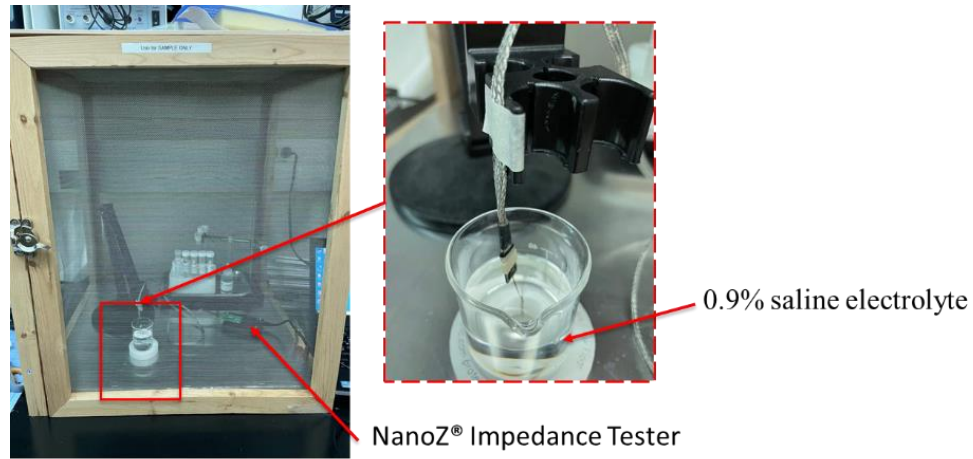


Figure 4.3 Laboratory setup for electrochemical impedance spectroscopy measurements.

Table 4.1 Electrochemical impedance spectroscopy measurement results.

Frequency	100.2 Hz	200.3 Hz	502 Hz	1004 Hz
Impedance (MΩ)	10.226	5.085	2.048	1.032
Phase (°)	-86.8	-89.5	-89.7	-89.4

4.3 Mechanical Characterization

To evaluate the mechanical properties of the fabricated neural microprobe, the tensile test and compressive test were performed using a DTS® delaminator, as shown in Figure 4.4. For the tensile testing, the two ends of the neural microprobe were fixed and stretched until failure. The motion speed is 100 μm/min. The average cross-section area of the shank of the neural microprobe is about (220 μm x 60 μm). The strain-stress curve of the tensile test is shown in Figure 4.5. The elastic modulus can be computed by computing the slope of the linear elastic region of its corresponding strain-stress curve. The elastic modulus of the neural microprobe is about 5.7 GPa, which is much less than the reported silicon-based neural implants 130-185 GPa [26]. Using the same method, The elastic modulus of a neural microprobe without the reinforcement layer was also measured, which is about 4.7 GPa. Although we embedded a Cr

reinforcement layer to facilitate the insertion, the elastic modulus of the neural microprobe does not increase much.

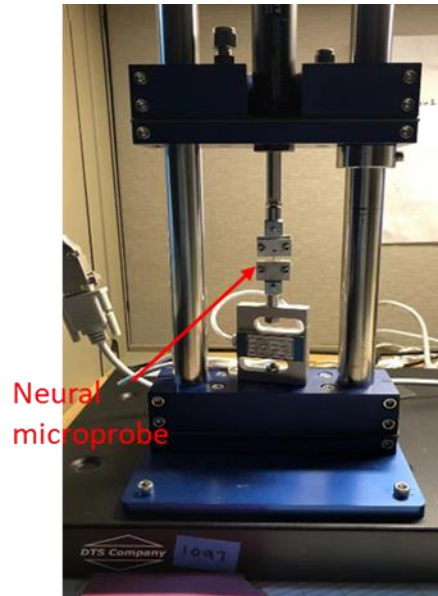


Figure 4.4 Lab Setup of tensile testing and compressive testing.

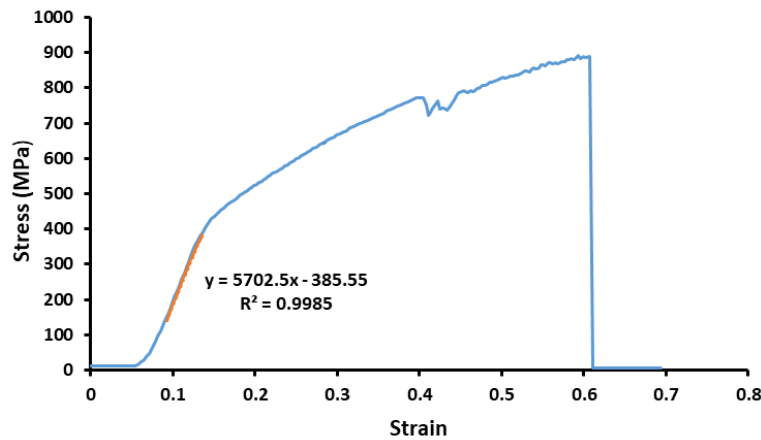


Figure 4.5 Strain-stress curve of the neural microprobe tensile testing.

In the compressive test, the microprobe with reinforcement layer occurs bending at 0.12 N, which indicates the critical force of the neural microprobe. We also compared the critical force of the neural microprobe with and without the reinforcement layer, as shown in Figure 4.6. The

results show that the reinforcement layer improves the stiffness of the neural microprobe by about 100 %. This indicates that the thin metal reinforcement layer is able to significantly improve the stiffness of the microprobe while maintaining good flexibility. In the future, different thicknesses of the reinforcement layer can be further investigated to balance the stiffness and flexibility.

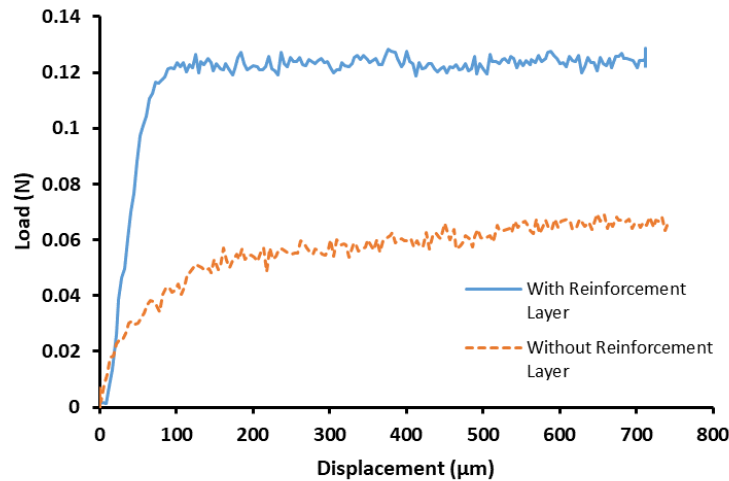


Figure 4.6 Neural microprobe compressive testing.

4.4 Summary

In this chapter, the neural microprobe was characterized to validate its effectiveness before being implanted. SEM with EDS measurements was performed to structurally and chemically evaluate the neural microprobe. The measurement results show that the electroplated electrode sites possess a 3D mushroom shape which entirely encapsulates the electrode sites to increase the measurement sensitivity and corrosion resistance. Electrochemical impedance spectroscopy measurements show that the fabricated neural microprobe has low impedance for DBS and action potential recordings. Tensile test and compressive test show that the embedded reinforcement layer is able to significantly improve the stiffness while maintaining good flexibility. To

overcome the challenges of buckling and deflection of flexible neural microprobes implantation, new techniques are discussed in the next chapter.

CHAPTER 5

DESIGN AND 3D PRINTED LONGITUDINAL-TORSIONAL TRANSDUCER FOR FLEXIBLE MICROPROBE INSERTION

This chapter presents a new waveguide-based longitudinal-torsional (L&T) ultrasonic transducer for a vibration-assisted insertion device. An array of helical structures is designed as effective waveguides to constrain wave propagations to achieve harmonic L&T vibration. The metal additive manufacturing process is employed to fabricate the complex geometric structures of the new L&T ultrasonic transducer. Finite element (FE) analysis and laboratory experiments are conducted and presented. The results show that the proposed new waveguide-based transducer is promising to deliver synchronized L&T vibration with high vibrational power efficiency.

5.1 Introduction

Hybrid longitudinal-torsional ultrasonic vibration has attracted a lot of attention recently for its possibility of providing more favorable effects than conventional longitudinal vibration. In the last few years, hybrid L&T transducers have been reported to be used in ultrasonic welding [93], ultrasonic-assisted machining [93,94], ultrasonic motors [95,96], medical insertion for treatment [78], etc. As discussed in Chapter 2, an L&T vibration has the potentials to further improve the insertion performance in comparison to conventional longitudinal only vibration.

To generate a hybrid L&T ultrasonic vibration, a traditional way is to utilize two pairs of piezo-ceramic rings with perpendicular polarization directions. For example, axially and tangentially polarized PZT rings were stacked together [97], or in another example, two special treated axially polarized PZT stacks are orientated in two mutually perpendicular quadrants [94]. While this method can control the vibration locus by adjusting the amplitudes and phases of two

applied signals, which is a computationally challenging task, unfortunately, the resultant power systems are relatively inefficient, and the driving circuits require much trials and compensations in operations.

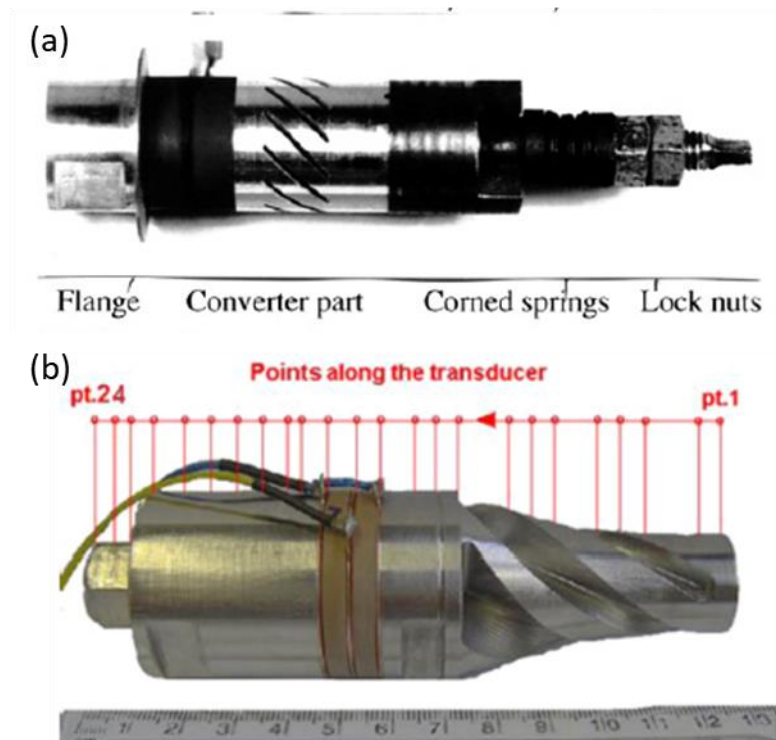


Figure 5.1 Typical longitudinal-excited L&T ultrasonic transducers: (a) diagonal slits type [87,92]; (b) helical grooves type [93,94].

The ultrasonic transducer is a critical component for vibration amplification and mode conversion. Modifying the transducer structure is another possible way to achieve L&T vibration. Figure 5.1 shows two examples of typical L&T ultrasonic transducers, by adding diagonal slits [93,98] or using helical grooves [99,100] on a longitudinal-excited transducer. The modified structures were cut around the circumference of the transducer while the inner cylindrical part remained solid. This type of transducer uses the partial reflection and superposition of the propagated waves to achieve hybrid vibration near the tip of the transducer [100]. Although several modeling and simulation techniques have been used to guide the design, it still remains

an error-prone process to find the correct synchronous node planes for both the longitudinal and the torsional vibration modes. This approach also suffers from another drawback that, only modifying the external structure of a cylindrical transducer makes the axial vibration dominate the superimposed vibration, which limits the effectiveness of synchronous both L&T conversions. In our previous study, a freeform shape of the transducer [101] is also capable of converting a one-dimensional vibration to an elliptical vibration. Although the freeform shape transducer is able to achieve desired vibration direction, the limitation of the traditional machining method constrains the geometric design and vibration conversion efficiency.

Additive manufacture (AM) or 3D printing can be used to fabricate complex geometries through layer-by-layer build-up processing, which provides a new promising way to design and fabricate novel power ultrasonic transducers. The Selective Laser Melting (SLM) process, one of the 3D metal printing processes, uses high power-density laser selectively to melt and fuse metallic powders, such as iron, titanium, nickel, aluminum, copper, etc. [102]. The SLM fabricated parts have high density and good mechanical properties, which are comparable to that of wrought materials [103–105]. The SLM fabricated parts possess excellent fatigue performance, which can meet the dynamic characteristic required for ultrasonic vibration applications. In this paper, we explore the possibility of the SLM process to fabricate the complex geometric structures of the new L&T ultrasonic transducer for the vibratory insertion system [106].

5.2 Design Principles

In this paper, the acoustic waveguide concept is investigated in L&T transducer design to convert a longitudinal excitation to an L&T hybrid vibration. An acoustic waveguide is a structure that can directly guide the wave propagation direction with minimal loss of energy. The output vibration is strongly dependent on the shape and direction of the waveguide structure. The

longitudinal excited vibration is the most widely used and straightforward vibration form. To convert a longitudinal vibration to an L&T hybrid vibration, we proposed a helical structure as the waveguide to guide the propagation direction between the input and output ends to a certain degree, as shown in Figure 5.2 red highlighted structure. A circular array of the helical structures is designed to obtain a symmetrical L&T vibration output. Figure 5.2 shows an illustration of the proposed hybrid L&T ultrasonic transducer concept.

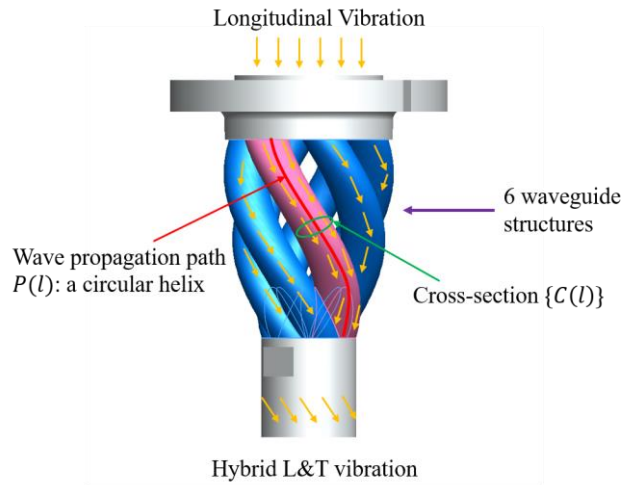


Figure 5.2 Illustration of the concept of the waveguide-based L&T transducer.

To parameterize the waveguide design for hybrid L&T vibration, we look into the working principles of curved transducers [107]. As shown in Figure 5.2, a waveguide can be defined as a wave propagation path $P(l)$ with an infinite number of cross-sections $\{C(l)\}$ along and perpendicular to the path, and l is the parameter along the curved waveguide. $G \in P(l)$ represents any point along the propagation path $P(l)$. Therefore, the vibration displacement \vec{u}_N for any surface point N on one cross-section $N \in \{C(l)\}$ can be represented as:

$$\vec{u}_N = \vec{u}_G + \vec{\varphi} \times \vec{GN} \quad (5.1)$$

Where \vec{u}_G is the displacement vector of point G , $\vec{\varphi}$ is the rotation vector of the cross-section $\{C(l)\}$, and \vec{GN} is the vector from point G to a surface point N . In Equation (5.1), we neglect the in-plane displacement of point N since the displacement of radial vibration is extremely small.

The wave propagation in the medium is a form of energy propagation, which can be studied by force exerted on the displacement. A hybrid L&T vibration can be represented by the combination of a longitudinal force and a torsional moment. Using the vibration displacement \vec{u}_N in Equation (5.1), the exertion force F_{ext} and the exertion torsional moment M_{ext} at a surface point N can be represented by applying Newton's second law and the laws of linear momentum and angular momentum. The exertion force F_{ext} and the exertion torsional moment M_{ext} between any two adjacent cross-sections $\{C(l)\}$ and $\{C(l + \Delta l)\}$ along the path $P(l)$ can be presented as follows, respectively:

$$\mathbf{F}_{ext} = \frac{\partial(\iiint \rho \frac{\partial \vec{u}_N}{\partial t} dV)}{\partial t} \quad (5.2)$$

$$\mathbf{M}_{ext} = \frac{\partial(\iiint \rho \vec{GN} \times \frac{\partial \vec{u}_N}{\partial t} dV)}{\partial t} \quad (5.3)$$

Where ρ is the mass density of the waveguide material, V is the corresponding volume. Due to the derivative of time $\partial/\partial t$ can be discrete and approximated to $1/\Delta t$, when the Δt is very small, Equations (5.2) and (5.3) can be simplified by using the ultrasonic frequency f that is equivalent to $1/\Delta t$. Thus, the above Equations (5.2) and (5.3) can be simplified as follows:

$$\mathbf{F}_{ext} = \frac{\partial(\iiint \rho \frac{\partial \vec{u}_N}{\partial t} dV)}{\partial t} \approx -f^2 \rho \iiint (\vec{u}_G + \vec{\varphi} \times \vec{GN}) dV \quad (5.4)$$

$$\mathbf{M}_{ext} = \frac{\partial(\iiint \rho \vec{GN} \times \frac{\partial \vec{u}_N}{\partial t} dV)}{\partial t} \approx -f^2 \rho \iiint (\vec{GN} \times (\vec{u}_G + \vec{\varphi} \times \vec{GN})) dV = -f^2 \rho \iiint (\vec{GN} \times \vec{u}_G + \vec{GN}^2 \vec{\varphi} - (\vec{GN} \cdot \vec{\varphi}) \vec{GN}) dV \quad (5.5)$$

Equations (5.4) and (5.5) indicate that the vibration exertion force and torsional moment, along with a propagation path $P(l)$, are determined by the waveguide path vector \vec{u}_G and the

waveguide cross-section shape vector \overline{GN} . To achieve the desired wave propagation direction with a certain angle, the wave propagation path needs to be first defined. Based on the above analyses, we proposed a circular helix curve as the propagation path that can be expressed in a cylindrical coordinate, as shown in the following Equation (5.6).

$$P(l) = \begin{cases} x(\theta) = \frac{d}{2} \cos\theta \\ y(\theta) = \frac{d}{2} \sin\theta, \theta \in [0, \pi] \\ z = \frac{L}{2\pi} \theta \end{cases} \quad (5.6)$$

Where d is the diameter of the circular helix, α is the rotational angle, and L is the height of the helix. The circular helix has a constant band curvature and constant torsion, which allows delivering a stable longitudinal and torsional vibration conversion. To achieve a symmetrical high-efficiency L&T vibration at the output surface of the transducer, a circular array of such helix paths was also designed. Importantly, when the rotational angle θ starts from 0 degrees and ends at 180 degrees, the circular array of helical paths can form a tapered shape that boosts the synchronous vibration to achieve a harmonic L&T vibration at the front output end, as shown in Figure 5.2. The ultimate exertion forces and torsional moment vectors are combined at the end of the transducer, which is the resultant exertion forces F_{ext_end} and the resultant exertion moments M_{ext_end} from the array of waveguides, shown as follows:

$$\mathbf{F}_{ext_end} = \frac{\partial(\iiint \rho \frac{\partial \mathbf{u}_{M'}^T}{\partial t} dV)}{\partial t} = \sum_{i=1}^n \mathbf{F}_{ext_i} \quad (5.7)$$

$$\mathbf{M}_{ext_end} = \frac{\partial(\iiint \rho \overline{GM'} \times \frac{\partial \mathbf{u}_{M'}^T}{\partial t} dV)}{\partial t} = \sum_{i=1}^n \mathbf{M}_{ext_i} \quad (5.8)$$

Where n represents the number of waveguides. Equations (5.7) and (5.8) can be used to guide the design of an array of waveguide structures for the objective of delivering harmonic joined vibration. Details are discussed in the next two sections.

5.3 Geometric Design and Configuration of the L&T Transducers

The detailed design and geometric specifications of the waveguide-based L&T transducer are shown in Figure 5.3. To achieve high electromechanical conversion efficiency and stable vibration performance, a bolt-clamped type Langevin longitudinal excited transducer was applied (see Figure 5.3). To minimize the size of the transducer and ensure the vibration amplitude, we used axial polarized Lead Zirconate Titanate (PZT-8) piezoelectric ceramic rings with an outer diameter of 15 mm and an inner diameter of 10 mm. In the design, every two adjacent piezoceramics rings are oriented in the opposing direction from each other. And among them, the copper electrodes are alternatively sandwiched. The piezo-ceramics stacks and copper rings are compressed by connecting bolt and back mass nut. For safety concerns, the mass bolt and transducer are connected to the ground while another pair of copper electrodes are connected to the ultrasonic driver, as shown in Figure 5.3. When sinusoidal voltages are applied to the PZT rings, all the PZT ceramic rings synchronously generate a longitudinal vibration. Since we developed this L&T transducer for later vibratory microprobe insertion devices (see Chapter 6), the diameter of the front end of the transducer is designed as 10 mm to fit a commercial Luer connector. Based on the size of the piezoelectric ceramic rings and the Luer connector, we designed a 4.5 mm diameter circular cross-section $\{C(l)\}$ waveguide structure along the helix path with a diameter of 10 mm (d in Equation (6)) and a height of 20 mm (L in Equation (6)). The CAD model of the new transducer was built in Solidworks® 2021. To determine the number of helical waveguides, finite element analysis is conducted to optimize the design discussed in the following section.

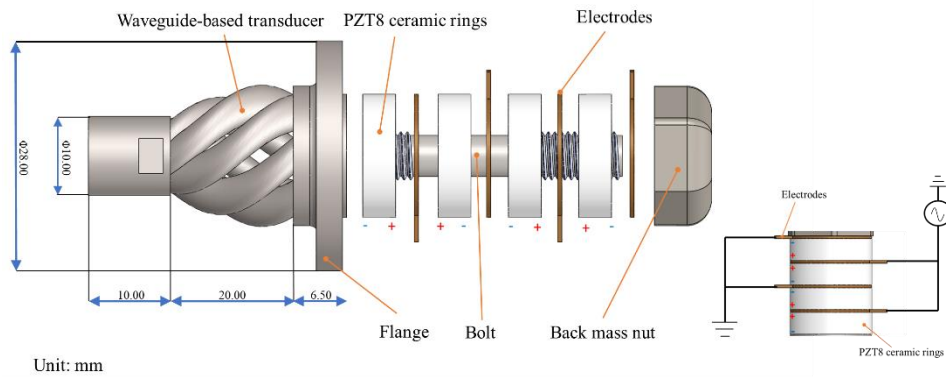


Figure 5.3 Design and configuration of the waveguide-based L&T ultrasonic system.

5.4 Finite Element Analysis

Finite element (FE) models of the new design were constructed for analyzing the natural frequencies, modal vibration shapes, and steady-state behaviors using ANSYS® 19.1 Workbench FE analysis software. The materials properties used in the FE models are first defined. The material used for the transducer is AlSi10Mg aluminum alloy that can be 3D printed using the SLM process. The connecting bolt and back mass nut are made of heavier material, 1045 steel, to transfer waves forward efficiently. The Lead Zirconate Titanate (PZT-8) was selected as the material used for the piezoelectric ceramics, which possesses a high mechanical quality factor, elastic property, and stability of piezoelectricity. The relevant parameters of PZT-8 are provided by the piezoelectric ceramics manufacturer. Table 5.1 lists the parameters of the material properties for the FE model analysis.

Table 5.1 Material properties for the FE model of the ultrasonic transducer.

Material	Density (kg/m ³)	Young's modulus (GPa)	Poisson's ratio
AlSi10Mg	2670	75	0.33
1045 Steel	7800	210	0.3
PZT-8	7600	/	0.32

For the FE analysis, the detailed vibration-related parameters of the PZT-8 are defined in the following Equations (5.9)-(5.11). The compliance matrix $[C^E]$ and the piezoelectric coupling matrix $[d]$ of the PZT-8 are given as follows:

$$[C^E] = \begin{bmatrix} 11 & -3.5 & -2.9 & 0 & 0 & 0 \\ -3.5 & 11 & -2.9 & 0 & 0 & 0 \\ -2.9 & -2.9 & 8.5 & 0 & 0 & 0 \\ 0 & 0 & 0 & 21 & 0 & 0 \\ 0 & 0 & 0 & 0 & 21 & 0 \\ 0 & 0 & 0 & 0 & 0 & 29 \end{bmatrix} * 10^{-12} \frac{m^2}{N} \quad (5.9)$$

$$[d] = \begin{bmatrix} 0 & 0 & 0 & 0 & 450 & 0 \\ 0 & 0 & 0 & 450 & 0 & 0 \\ -100 & -100 & 225 & 0 & 0 & 0 \end{bmatrix} * 10^{-12} \frac{C}{N} \quad (5.10)$$

And the relative permittivity matrix $\left[\frac{\varepsilon^T}{\varepsilon_0}\right]$ of the PZT-8 can be found as follows:

$$\frac{\varepsilon^T}{\varepsilon_0} = \begin{bmatrix} 1400 & 0 & 0 \\ 0 & 1400 & 0 \\ 0 & 0 & 1025 \end{bmatrix} \quad (5.11)$$

5.4.1 Harmonic Response Analysis

Harmonic response analysis was conducted to predict the vibration output. The Piezo and MEMS module embedded in the ANSYS® 19.1 Workbench was used for FE simulation of the piezoelectric ceramics. An exciting voltage of 45 Vrms (Root-Mean-Squared voltage) was applied to the piezoelectric ceramic rings to simulate the actual power level in vibrations. The selected 45 Vrms is roughly about the peak-to-peak voltage $V_{p-p} = 64$ V. In the FE analysis, a fixed constraint was added at the flange of the transducer as the boundary condition. To simplify the FE modeling, the four pieces of copper electrodes were neglected in the FE electromechanical coupling model, due to their thin thickness and much less mass weight.

1) Number of Waveguides

According to Equations (5.7) and (5.8), the number of waveguide structures influences the synchronous L&T vibration conversion efficiency. We investigate the relationship between the vibration outputs and the number of waveguides designed in Section 5.3. The simulation frequencies are specified in a widely used ultrasonic frequency range of 20 kHz – 30 kHz for most ultrasonic applications. In the FE analysis, all these transducers are able to achieve a steady-state hybrid L&T vibration output at the tip of the transducer. The resonant frequency and L&T conversion ratio were obtained for each scenario, as shown in Figure 5.4. The waveguide-based transducer with six waveguides achieves excellent L&T performance. This can be explained from two aspects. The decrease in the number of waveguides reduces the effective energy propagated from the transducer's input end to the output end, resulting in a reduction in final output amplitudes. On the other hand, as the number of waveguides increases, the mass and the rigidity of the transducer increase, which requires more driving power to achieve the same vibration amplitude. As the number of waveguides increases until the waveguide structures join together, the longitudinal vibration becomes the primary vibration component, similar to the traditional L&T ultrasonic transducer in Figure 5.1. In Figure 5.4, it can be noticed that as the number of waveguides increases, the resonant frequency also increases.

We finally designed the transducer with six helical waveguides. Its corresponding harmonic response analysis results are shown in Figure 5.5. In Figure 5.5(b), the vibration displacement vectors demonstrate that the waves propagate along the six helical waveguides. The longitudinal vibration is gradually guided to an L&T vibration and synchronized at the tip of the transducer. Importantly, The peaks of longitudinal and torsional vibrations occur at the same

frequency, as shown in Figure 5.5 (a), indicating that the transducer's longitudinal and torsional vibrations resonate at the same frequency.

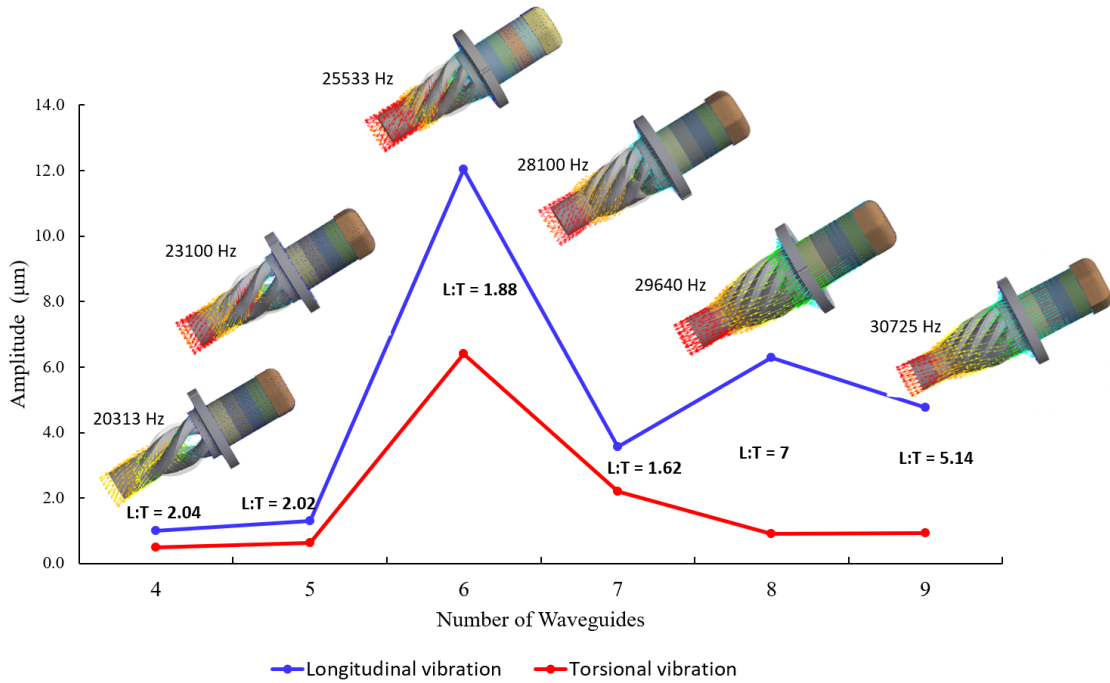


Figure 5.4 Relationship between the number of waveguides and output vibrations.

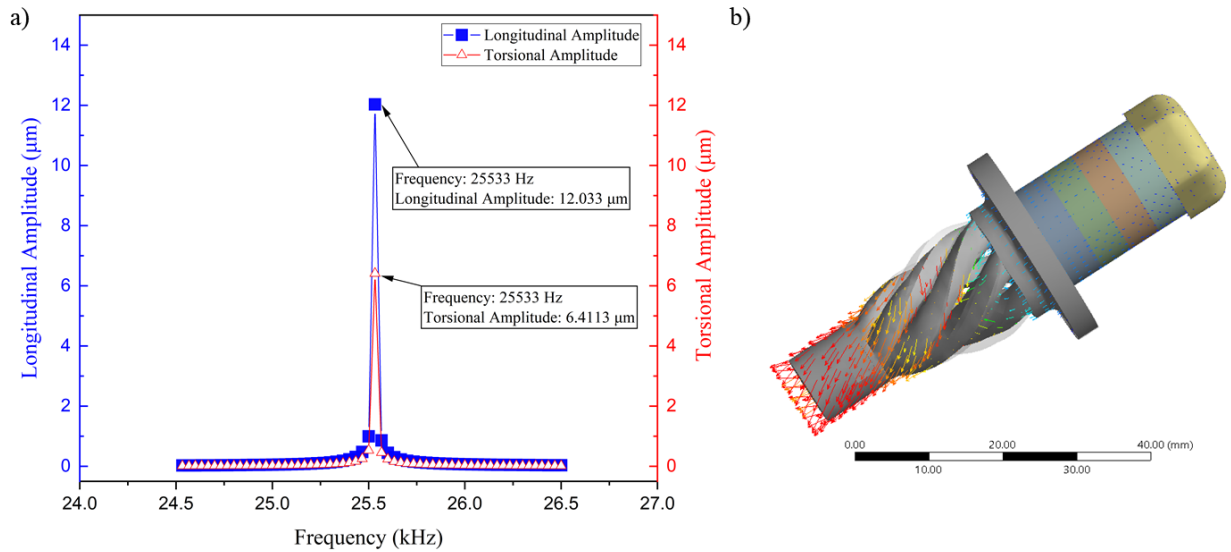


Figure 5.5 Harmonic response simulation results: (a) vibration amplitudes under the analysis frequency 25 kHz to 27 kHz, (b) working at the resonant frequency 25,514 Hz.

2) Other Resonant Frequencies

In addition to the 20 kHz – 30 kHz frequency range, we also explored the resonant vibration of the new transducer in other frequency ranges. In Figure 5.6, it was identified that the transducer has another steady-state resonant frequency at 59.0 kHz. At the tip of the transducer, a steady-state hybrid L&T vibration can be obtained. Both longitudinal and torsional vibrations are still resonating at the same frequency. Importantly, the primary vibration components swap between 25.514 kHz and 59.0 kHz. At the frequencies of 25.514 kHz, the longitudinal vibration is the dominant vibration component with an L-T conversion ratio of (2.1299:1.3602), as shown in Figure 5.5 (a). On the other hand, at the frequencies of 59.0 kHz, the torsional vibration becomes the dominant vibration component with an L-T conversion ratio of (2.5139:8.2555), as shown in Figure 5.6 (a). This advantage enables the L-T conversion ratio to be adjustable to meet more needs of various applications by adjusting the frequency.

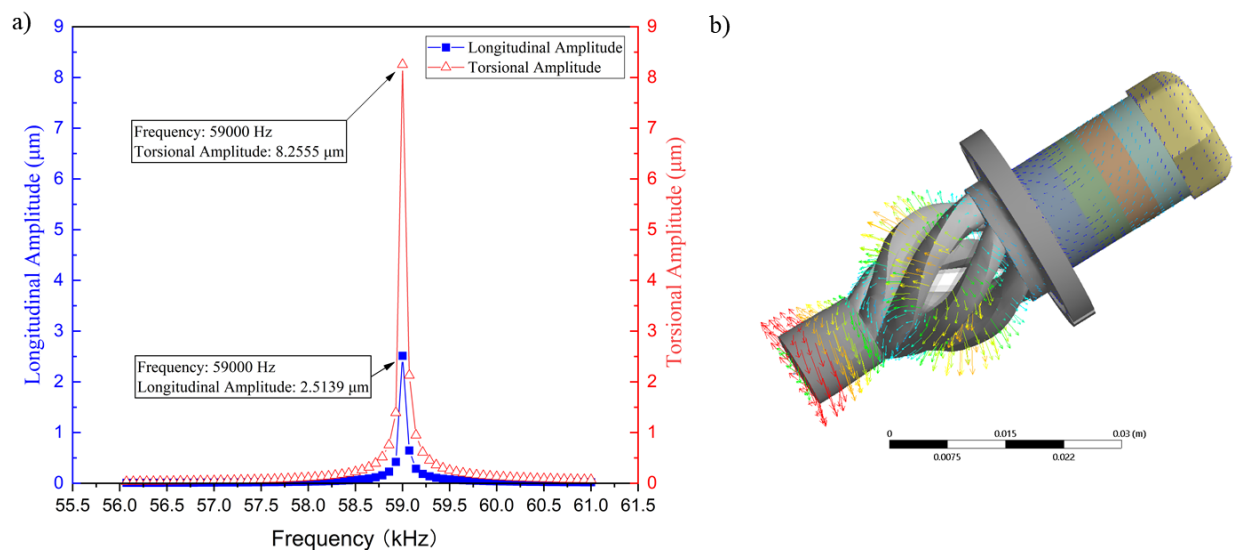


Figure 5.6 Harmonic response simulation results: (a) vibration amplitudes under the analysis frequency 56 kHz to 61 kHz, (b) working at the resonant frequency 59,000 Hz.

3) Other Cross-section Shapes

According to Equations (5.4) and (5.5), the waveguide's cross-section shape $\{C(l)\}$ is another factor that affects the vibration performance of the transducer. In addition to the circular cross-section shape, we tested rectangle and triangle cross-section shapes in the FE model simulation. For the comparison, we only modified the cross-section shape $\{C(l)\}$ and kept all the other parameters the same. Figure 5.7 shows that both the rectangular and triangular cross-section shapes were still able to achieve harmonic L&T vibration resonance. This also demonstrates the effectiveness of the waveguide structure. However, the maximum deformation appears on the edges of waveguide structures instead of the output end of the transducer, as shown in Figure 5.7. The concentrated stress increases the fatigue of the waveguide structures and reduces output vibration efficiency. Among the three cross-section shapes in Figures 5.5 – 5.7, it seems the symmetrical round shape delivers the best resonant vibration result at the tip of the transducer.

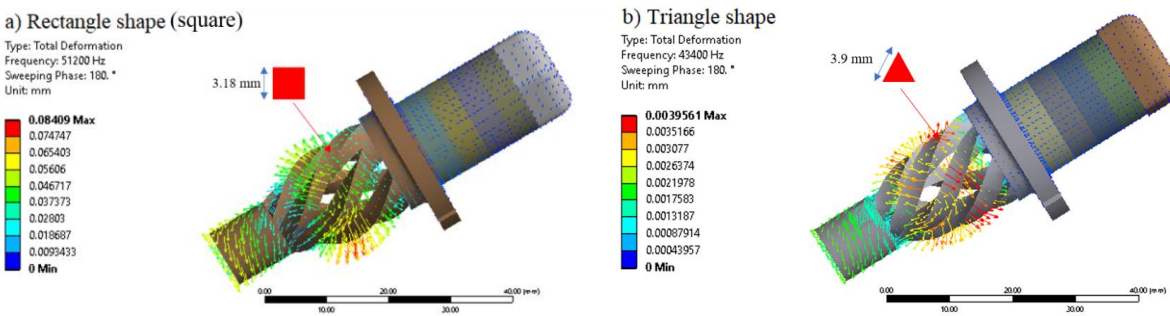


Figure 5.7 Harmonic response simulation results of different cross-section shapes of the waveguide: (a) rectangle shape, (b) triangle shape.

4) Fatigue Behavior

The high-frequency vibration may cause the failure of the transducer due to the fatigue of the structure. To validate the fatigue behavior of the transducer, we also analyze the maximum stress of the transducer generated at the resonant frequency. That is particularly important to 3D

printed applications due to the potential defects in the actual part. The maximum principal stress method was employed in the FE simulation to analyze the stress distribution, as shown in Figure 5.8. The maximum stress linearly increases with the increased driving voltage, as shown in Figure 5.9. At the 60 Vrms driving voltage, the maximum stress is only about 25 MPa on the waveguide structure. It is known that the less stress applied to the structure, the longer the life of the part. According to the reported stress-life behavior of the SLM-AM AlSi10Mg parts, it can withstand 10^8 and more cycles under the stress 60MPa [104]. After heat treatment, the SLM-AM AlSi10Mg builds can sustain longer cycles under higher stress [103]. In our case, since the predicted stress is far less than which in fatigue testing, the theoretical fatigue life would be long enough for ultrasonic transducer applications.

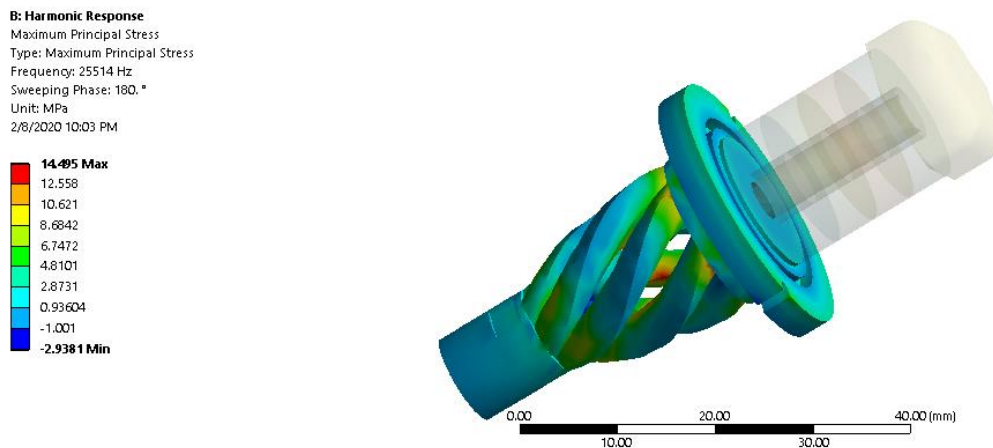


Figure 5.8 Maximum stress analysis at its corresponding resonant frequency.

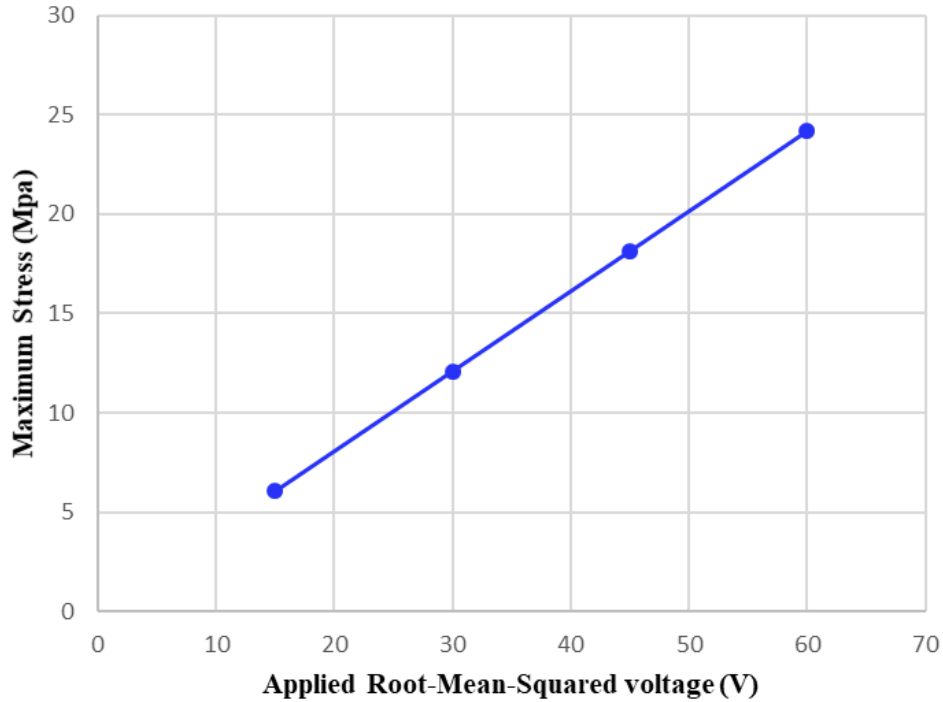


Figure 5.9 Maximum stresses under different applied drive voltages.

5.4.2 L&T Vibration Modal Analysis

To better analyze the vibration characteristics of the waveguide-based ultrasonic transducer, modal analysis was performed based on the previous harmonic analysis. Figure 5.10 and Figure 5.11 show the 1st to 3rd modal responses under the frequency range of 20 kHz – 30 kHz and 55 kHz – 65 kHz, respectively. The desired hybrid L&T vibration modes appear around their resonant frequencies. The largest L&T deformation concentrates on the output end of the transducer. This L&T modal shape demonstrates that the waveguide structure is able to achieve a synchronous L&T vibration, instead of only relying on the superimposition of different modes. Similar to the harmonic response analysis results, the dominant vibration component at 25.502 kHz is longitudinal vibration, while the dominant vibration component at 57.285 kHz is torsional vibration, as shown in Figure 5.10(c) and Figure 5.11(a).

In addition to the low-order L&T vibration mode, the other two modal shapes, which are always a pair of flexing vibrations, contribute to the final vibration, as shown in Figure 5.10(a) - (b) and Figure 5.11(b) - (c). They have similar modal frequencies, while their vibration directions are perpendicular to each other. The small frequency discrepancy of each pair of flexing vibrations enables one resonance frequency to efficiently excite two vibration modes. In the meanwhile, each pair of flexing vibrations shares the same synchronous node plane at the joint position of the helical structures. These conditions lead to the synchronization of the pair of flexing vibration modes to an L&T vibration with perfect frequency-matching. Since the actual vibration is superimposed by its corresponding modes, both the L&T mode and the paired flexing modes contribute to achieving a synchronized L&T vibration, resulting in high conversion efficiency.

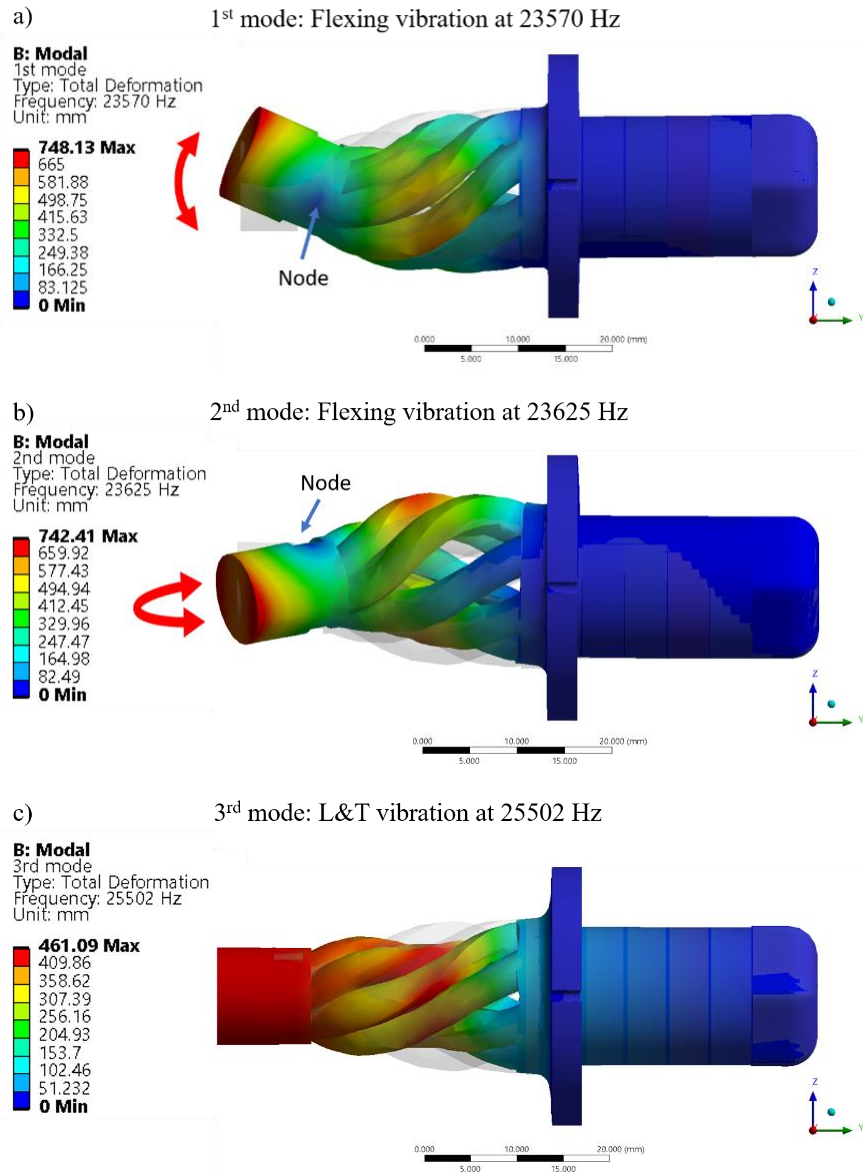


Figure 5.10 Modal analysis results of the waveguide-based L&T transducer under 20 kHz to 30 kHz. (a) and (b) are a pair of flexing vibrations with a frequency difference of 26 Hz. (c) is an L&T vibration.

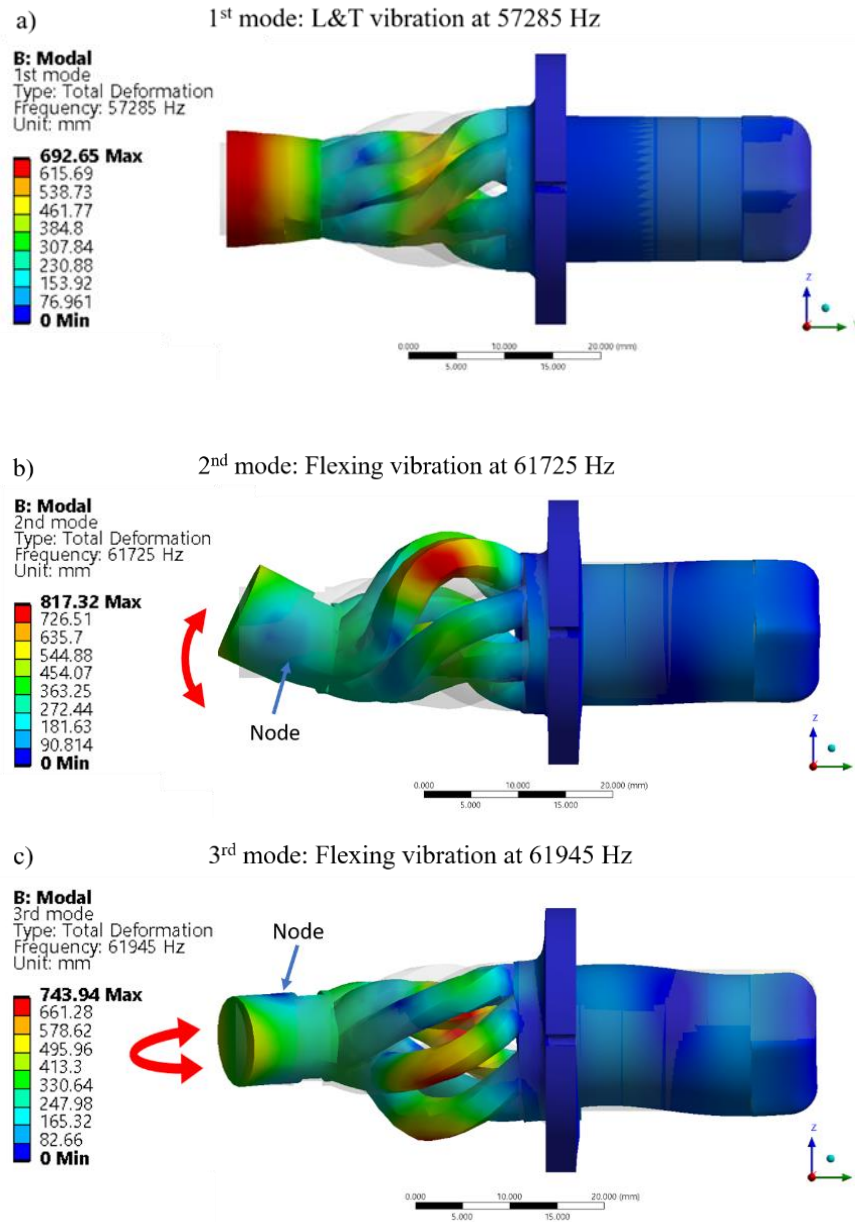


Figure 5.11 Modal analysis results of the waveguide-based L&T transducer under 55 kHz to 65 kHz. (a) is an L&T vibration. (b) and (c) are a pair of flexing vibrations with a frequency difference of 220 Hz.

5.5 3D Printed Prototype of the Waveguide-based Transducer

The novel transducer with six waveguides was fabricated for laboratory experiments and validation. Due to the complexity and challenges of the geometric shape in the new L&T

transducer design, the new transducer was fabricated by using a 3D metal SLM process at the lab. The laser-based SLM-AM process can fabricate complex geometric components with good mechanical properties. For the experiments, the L&T transducers were fabricated by using SimpNeed SLM 280 AM machine with the AlSi10Mg metal powder. The particle size of AlSi10Mg powder is within the range of 24.0 - 45.0 μm . Table II shows the SLM process parameters used in the metal AM of the designed transducer. Figure 5.12(a) shows a 3D printed waveguide-based transducer fabricated by the SLM process.

Table 5.2 SLM machining parameters.

Parameters	Values
Laser beam power	80 W
Laser beam diameter	80 μm
Layer thickness	0.06 mm
Laser scanning speed	900 mm/s

Because of the relatively rough surface finish and tolerance of the as-built SLM components (± 0.1 mm), the L&T transducer was first fabricated without the connecting hole and threads. A 0.5 mm allowance was assigned to the flange region for further finishing operations. Subsequently, a turning process was applied to finish the back end and the outer surface of the flange for later assembly. Except for the flange surface, no other finishing operation was conducted on the rest of the 3D printed regions. If needed, some additional potential finishing methods, such as electrochemical polishing, or abrasive flow machining, could be used in the future for a better finish. A drilling process was performed, followed by a threading operation with an M5x0.5 tap for the connecting bolt. Figure 5.12(b) shows the prototype of the 3D printed L&T transducer after machining and assembly.

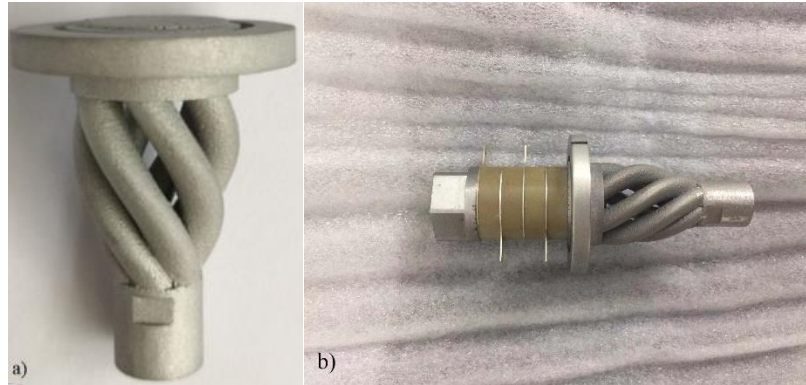


Figure 5.12 The prototype of the waveguide-based transducer fabricated by SLM-AM (a) original 3D printed part, (b) after assembly.

To ensure the integrity of the fabricated transducers, the SLM printed transducers were further inspected. The microscopic exam of the SLM printed part shows the fabricated transducer possesses fine cellular dendritic microstructure, and some typical porosities were observed in the SLM printed parts. The level of porosity could affect the density and mechanical performance of the components, thereby affecting the acoustic characteristics of the transducer, such as resonance frequency. Although we did not exam the impact of material porosity in the vibration resonance performance, we did exam the material porosity. The porosity and density of the transducer were investigated by examining the fabricated parts. The relative density in the as-built AlSi10Mg part material is 99.85 %, with a porosity of 0.15%. In this paper, we did not apply any heat treatment to the SLM printed parts. If higher part material density or lower porosity is needed, some heat treatments or hot isostatic pressing methods could be used to reduce the porosity in materials after SLM processes. The fabricated transducer with its assembly was measured to evaluate its vibration performance. Details are presented in the next section.

5.6 Characterization of the 3D Printed L&T Transducer

5.6.1 Experiments on Impedance Analysis

To validate the performance of the fabricated waveguide-based L&T transducer, an impedance analysis was first conducted. Figure 5.13 shows the lab experimental setup with a Wayne Kerr 6500B precision impedance analyzer used in the test. Based on the parameters analyzed earlier in the FE analysis, the transducer impedance characteristics were tested within the frequency ranges of 24 kHz to 27 kHz and 57 kHz to 65 kHz, respectively.

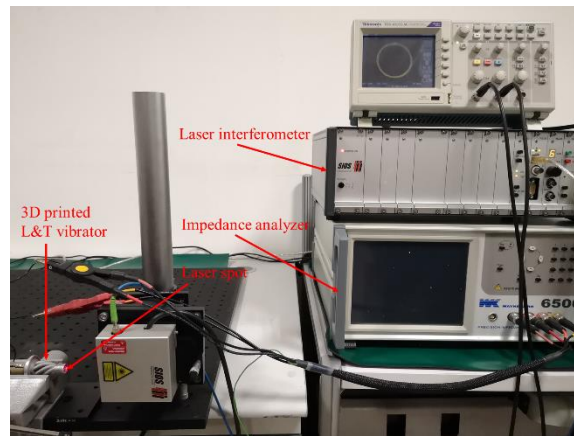


Figure 5.13 Laboratory setup for measurement of the L&T transducer.

The measurement results of the impedance and phase angle are shown in Figure 5.14. In the corresponding scanning period, only one minimum impedance occurred at 25.350 kHz and 59.629 kHz, respectively. The minimum impedance is known as the series resonance f_s , which indicates the mechanical resonant frequency of the transducer. The maximum impedance occurs at 25.623 kHz and 62.713 kHz, also known as the parallel resonance f_p . The electromechanical coupling factor k can be calculated by the following Equation:

$$k = \sqrt{\frac{f_p^2 - f_s^2}{f_p^2}} \quad (5.14)$$

According to Equation (5.14) and the measured data, the electromechanical coupling factor k was found to be 14.5% and 31.0% in the experiments. As shown in Figure 5.14, the corresponding phase angle is 23.7° and 13.9° , respectively, which means the entire system is inductive. Later, an extra capacitance can be applied to compensate for the measured phase angle. The measured resonant frequency is in good agreement with the simulation result. The discrepancies between the simulation results and the actual measured results are less than 1% off from the FE analysis. This is a small discrepancy and is considered acceptable, given there are some inherited defective variables from the SLM part material (porosity in the material), dimensional and geometric tolerance errors, and the PZT stacks assembly tightened force difference. For future improvement of the FE modeling, additional variables can be further included in the consideration, like the material characteristics of the PZT, more accurate boundary conditions in the FE modeling and simulation, etc.

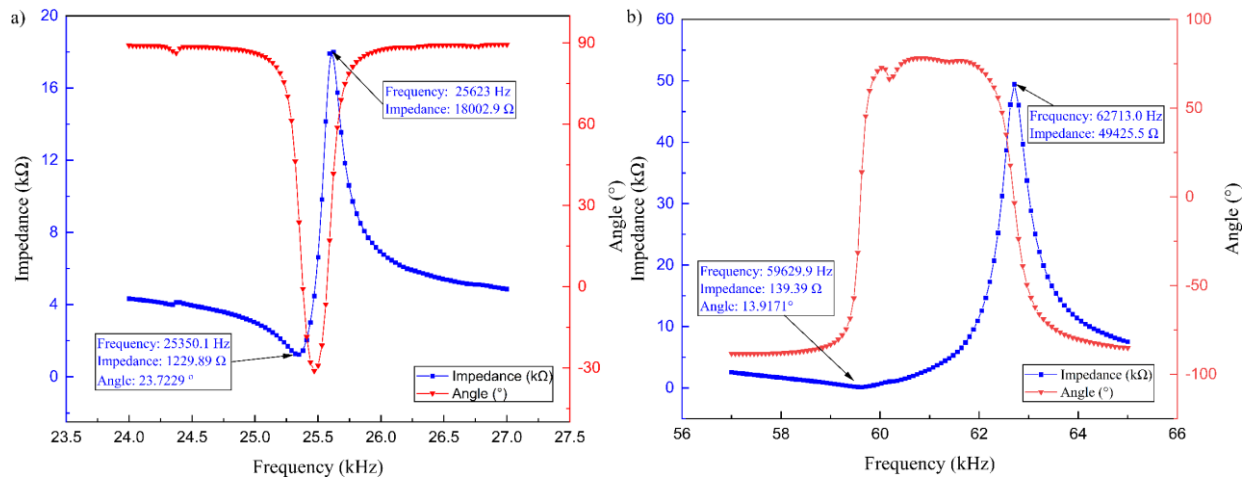


Figure 5.14 Impedance measurement results of the prototype of the waveguide-based ultrasonic transducer: (a) 24 kHz to 27 kHz; (b) 57 kHz to 65 kHz.

5.6.2 Experiments on Vibrational Characterization

To measure the vibration amplitudes along with longitudinal and torsional directions, a SIOS Meßtechnik GmbH laser interferometer was used in the experimental measurements. The lab experimental measurement setup is shown in Figure 5.15. The transducer was clamped by a table vise on the flange. Due to the limited capability of our laser interferometer, it is difficult to measure the torsional amplitude (torsional arc length) directly. To overcome this limit, a small rectangular block was attached to the tip of the transducer to assist the measurement, as shown in Figure 5.15(b). The block was aligned with the center of the transducer tip. The distance between the measuring laser spot and the center of the transducer is 4.0 mm. The measured tangential amplitudes are used to approximate the torsional amplitude.

Figure 5.16 shows the measured longitudinal and the torsional vibration amplitudes under different levels of driving voltages (16V, 32V, 48V, and 64V) within the frequency ranges of 24.0 kHz to 26.5 kHz and 56 kHz to 62 kHz, respectively. The measured vibrational characteristics are also in good agreement with the impedance analysis and the predictive simulation results. Figure 5.16 shows there is about a 0.40 kHz frequency shift between the longitudinal resonant vibration frequency and the torsional resonant vibration frequency. Since there is no such discrepancy occurs during the FE analysis and impedance analysis, a possible reason may come from the measurement inaccuracy resulting from the attachment of an additional block at the transducer tip for laser torsion measurement. The attached block affects the natural frequency of the transducer. In future studies, some additional fine-tune and calibration procedures might be used to reduce the discrepancy between longitudinal resonant frequency and the torsional resonant frequency.

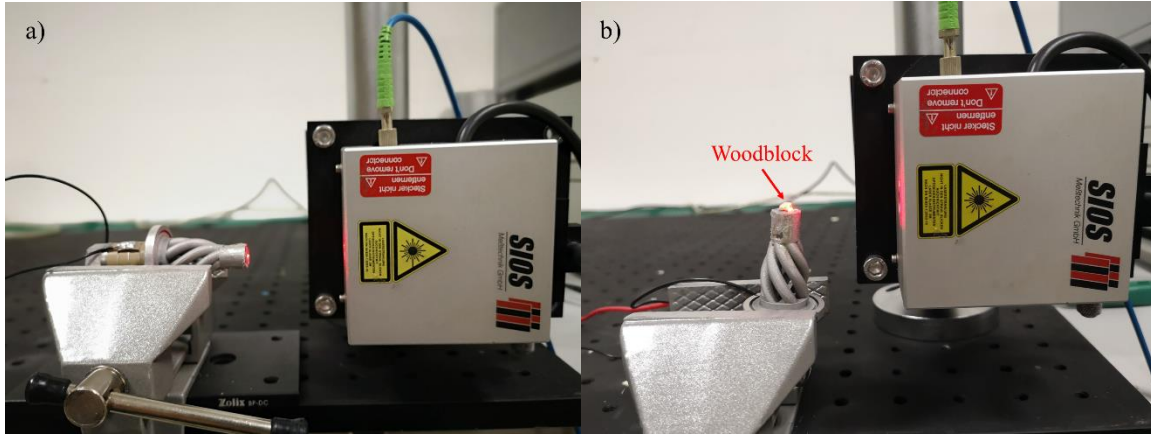


Figure 5.15 Experimental setups to measure the vibration amplitudes: (a) longitudinal direction (b) torsional direction.

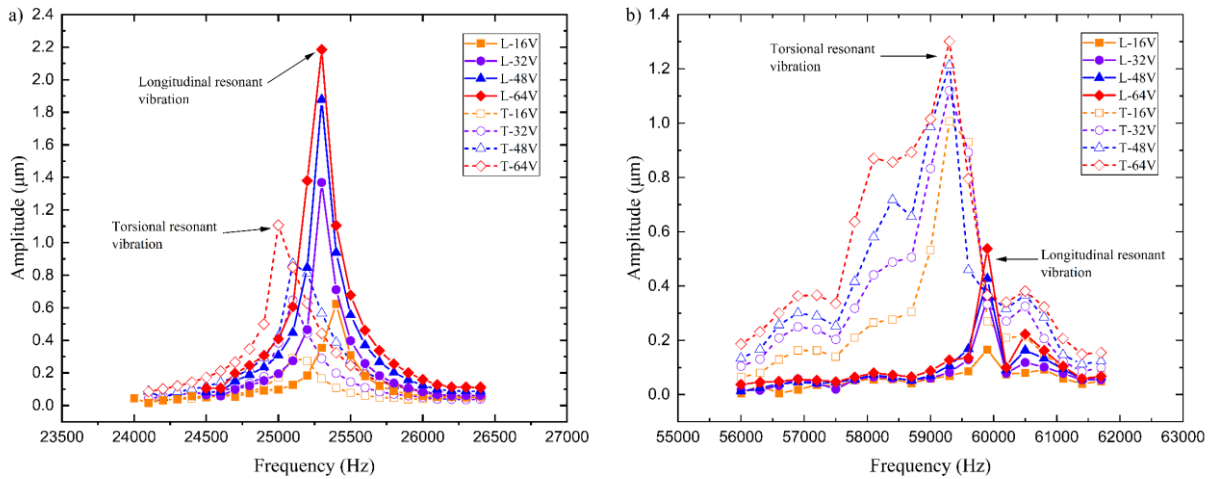


Figure 5.16 The plot of the L&T displacement amplitudes versus the frequency: (a) 24.0 kHz to 26.5 kHz; (b) 56 kHz to 62 kHz.

Figure 5.17 shows the relationship between the input voltage and vibration amplitudes under two resonant frequencies. Both the longitudinal and the torsional amplitudes sustain an almost linear change with the increase of driving voltage. This observation makes the vibration amplitudes predictable, which is good for the future applications of the waveguide-based transducer.

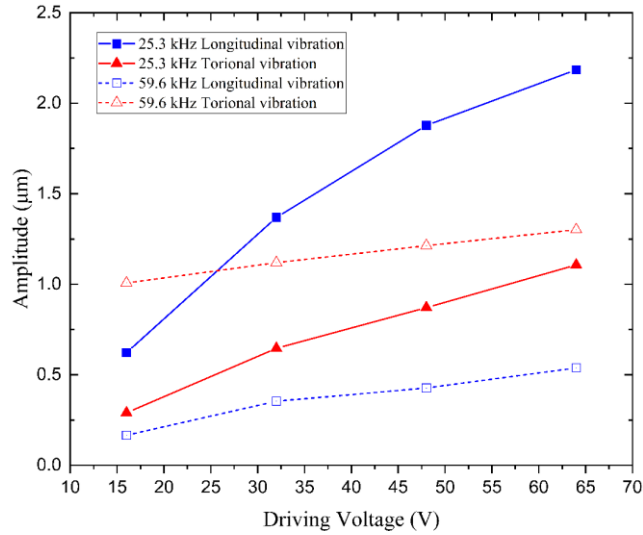


Figure 5.17 The plot of vibration amplitudes versus driving voltage.

5.7 Summary

A waveguide-based longitudinal-excited L&T ultrasonic transducer has been presented in this chapter. Analytical modeling of the waveguide-based L&T transducer design was discussed. Due to the complex geometric shape, the SLM-AM was used to fabricate the L&T transducer with AlSi10Mg metal powders. Both the simulation and the laboratory experiments have demonstrated that the new waveguide-based L&T transducer can deliver synchronized longitudinal and torsional vibrations at the same corresponding resonant frequency. The L&T conversion ratio varies at different resonant frequencies, which provide more application potentials. Impedance analysis and vibration characteristics of the SLM-AM prototype exhibited excellent electromechanical performance and acoustics characteristics. The presented waveguide-based L&T transducer can be possibly used for applications in medical treatment applications, such as vibratory neural microelectrode implantation. In the next chapter, we will discuss more details about using the presented L&T ultrasonic transducer to assist the microprobe implantation to soft tissues.

CHAPTER 6

IMPLANTATION STRATEGIES FOR FLEXIBLE NEURAL MICROPROBE

This chapter presents a promising implantation strategy for inserting the fabricated flexible neural microprobe to deliver accurate insertion with minimized tissue damage and deflection. Inspired by the mosquito biting process in nature, longitudinal and twisting (L&T) ultrasonic vibration with bio-dissolvable guides are applied to assist the insertion. This method also can be scaled up for other types of flexible neural microelectrodes implantation. Details are discussed in the following sections.

6.1 Introduction

Although flexible neural microprobes mitigate the unfavorable mechanical mismatch, they are more susceptible to bending and buckling during implantation due to the decrease of stiffness. The bending and buckling lead to a deflection and even failure of the implantation to reach the deep brain target. To deal with this dilemma, various strategies were developed to assist the implantation of flexible neural microelectrodes, described in Chapter 2. Among them, a stiffer shuttle structure is a common and useful way to guide the probe insertion by temporarily attaching a rigid backbone or needle [56–58]. While the straightforward shuttle strategy allows a deeper insertion, it could cause larger insertion trauma, noticeable displacement during shuttle retraction, and a clearance between the electrode and tissue after shuttle removal. Attaching the stiffer shuttle with a neural probe to an ultrasonic vibration device shows another promising implantation strategy, which further improves the insertion performance and reduces chronic inflammatory

response [73,108]. Since this method still uses a stiffer shuttle actuated by ultrasonic vibration, similar potential unfavorable consequences are still introduced during insertion.

To increase the stiffness and implantation success rate, some insertion guide structures were inspired by the mosquito bite process where a mosquito's two labium are initially inserted into the skin, providing a guide and support for its central labrum [67,109]. By bracing the labrum at its end during insertion, the critical buckling force of the central labrum can be significantly improved. Andrew et al. [68] proposed a guide structure to aid the implantation of ultra-flexible microprobes. This biomimetic guide successfully raises the critical buckling force of the microprobe up to 3.8-fold, leading to a 100% insertion success rate. That plastic guide structure has to be physically removed after use, which may cause secondary damage and interference to the already implanted neural probe during surgery. In this chapter, we explored directly implanting our fabricated flexible neural probe with a longitudinal and twisting ultrasonic vibration and bio-dissolvable insertion guide to deliver an accurate insertion.

6.2 Vibration Assisted Insertion

6.2.1 Influence of Ultrasonic Vibration

Inspired by the mosquitos in nature, vibration is able to assist the flexible tube in penetrating tissues. A number of studies have demonstrated that vibration-assisted rigid needle insertion can effectively lower the insertion force by reducing the friction force [73,78,108]. Friction acted to resist the motion of the neural microprobe is the primary force component during insertion. As the neural microprobe is inserted deeper, the friction force increases dramatically due to the increase of clamping force and contact areas with the surrounding tissue. Reducing the insertion friction force plays a critical role in the implantation performance [73,78].

The macroscopic friction force reduction under the influence of vibration can be explained by the cyclic and instantaneous change of the resultant sliding velocity vector (in-plane vibration) and the change in the magnitude of the normal load (out-plane vibration) [110,111]. The conventional longitudinal vibration is an in-plane vibration, which reduces friction by changing the resultant sliding velocity (\vec{v}). Based on Coulomb's law of friction, the friction force f acting on both sides of a flat and flexible neural electrode probe can be expressed as follows:

$$f = -2\mu_0 F_n \frac{\vec{v}}{|\vec{v}|} \quad (6.1)$$

where μ_0 is the coefficient of static friction, F_n is the clamping force, \vec{v} is the relative velocity between the microprobe and the contacted tissue surfaces. When a longitudinal direction vibration is applied to the electrode probe, its motion function can be described as:

$$u_l = A_l \sin(\omega t) \quad (6.2)$$

where A_l is the longitudinal vibration amplitude along the insertion direction, and ω is the vibration frequency, and t is the time. Since the vibrational velocity function can be derived from its motion equation of Equation (6.2), the relative velocity of the electrode probe can be derived from Equation (6.2) as follows:

$$\vec{v} = v_0 + A_l \omega \cos(\omega t) \quad (6.3)$$

where v_0 is the sliding velocity (insertion velocity) and $A_l \omega$ is the vibration velocity as defined in Equation (6.3). By substituting Equation (6.3) into Equation (6.1), the friction force f on the electrode probe can be represented as follows:

$$f(t) = -2\mu_0 F_n \frac{v_0 + A_l \omega \cos(\omega t)}{\sqrt{v_0^2 + (A_l \omega)^2}} \quad (6.4)$$

The effective friction force to be measured is actually a time-average friction force [111], which can be calculated by Equation (6.5) as follows:

$$\bar{f} = \frac{1}{T} \int_0^T f(t) dt \quad (6.5)$$

Where T is the period of the vibration oscillation.

In an earlier study, Littmann et al. [112] found that a friction force reduction can be formulated as a function related to the velocity ratio ζ , shown as follows:

$$\zeta = \frac{v_0}{A_f \omega} \quad (6.6)$$

In Chapter 5, when using the piezoelectric ceramic PZT-8 and the developed ultrasonic transducer to generate a vibration, there is a good linear relation between the driving voltage and vibration amplitude based on the actual reported measurements [100,113]. Therefore, the velocity ratio ζ can be represented as follow:

$$\zeta = \frac{v_0}{cE\omega} \quad (6.7)$$

Where c is the conversion coefficient between the driving voltage and the vibration amplitude, and E is the driving voltage. The conversion coefficient c is the inherent property related to the transducer and piezoelectric components, which is determined by the device itself. When the vibration device is working at its resonant frequency, one can adjust the insertion speed and driving voltage to change the velocity ratio ζ .

Using Equation (6.4) to (6.7), the friction force reduction γ can be computed and shown as follows:

$$\gamma = \frac{\bar{f}}{\mu_0 F_n} = \begin{cases} 1 & \text{if } \zeta > 1 \\ \frac{2}{\pi} \sin^{-1} \zeta & \text{if } 0 < \zeta < 1 \end{cases} \quad (6.8)$$

According to Equation (6.8), the friction reduction tends to no change at $\zeta > 1.0$, which means the change of resultant sliding velocity is too small to affect the total friction. On the other hand, the friction force \bar{f} can be reduced when the oscillation velocity is faster than the sliding velocity. This is the case that requires either a larger amplitude (higher driving voltage) and/or

higher resonant frequency (like ultrasonic vibration). It is difficult to achieve both high-frequency and large-amplitude vibration due to its related high mechanical impedance. In addition, large-amplitude and high-frequency vibration may lead to an increase in tissue temperature and tissue damage during the insertion.

To further reduce the friction force without only increasing the vibration amplitude, we proposed to apply a three-dimensional longitudinal-twisting vibration on the flexible neural microprobe, to achieve both the in-plane and the out-plane vibrations. When additional twisting vibration is applied to the planar microprobe, both the velocity and the clamping force on the electrode probe surface are cyclic changing. This leads to further friction reduction. Based on Kyle's [114] model of tissues, the tissue element can be assumed as a pair of stiffness springs and damper, as shown in Figure 6.1. The change of clamping force ΔF_n acting on each side can be formulated as a linear relation to the deformation of the tissue.

$$\Delta F_n = kA_t \sin(\omega't) \quad (6.9)$$

Where k is the spring constant of the tissue, A_t is the actual twisting vibration amplitude in the tissue, which equals the largest deformation of the tissue, ω' is the tissue deformation frequency.

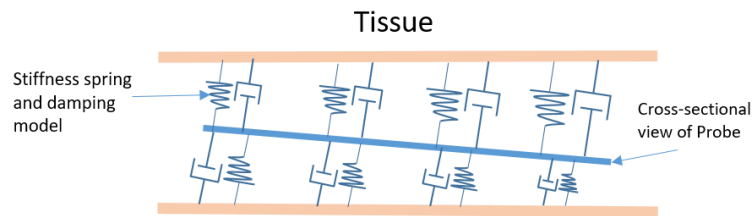


Figure 6.1 The interaction model of planar electrode probe and tissue under the influence of Longitudinal-Twisting vibration.

When the twisting vibration is superposed on the flexible electrode probe, the tissue will be cyclically compressed and released at a deformation frequency ω' . While the clamping force

on one side of the probe is increased by compressing the tissue, the clamping force on the other side decreases due to the stress release of tissue tension. Assuming there is no separation between the electrode probe and the tissue ($\omega' = \omega$), the increased amount of the force should equal the reduced force, according to Equation (6.9). The model can be equivalent to an oscillating clamping force superposed onto the probe surface, as expressed in Equation (6.10). According to the research presented in [115], this out-of-plane ultrasonic oscillation is able to further reduce the friction force f shown as follows:

$$f = -2\mu_0(F_n - kA_t \sin(\omega't)) \frac{\bar{v}}{|\bar{v}|} \quad (6.10)$$

On another note, if there is a time lag of tissue restoring from the twisting vibration, making $\omega' < \omega$, a separation between probe and tissue may occur. This makes the clamping force asymmetrical on both sides of the probe. The asymmetrical changes reduce the total clamping force, thereby further lowering the macroscopic friction force.

6.2.2 Devices Development

In this study, the longitudinal (L) vibration device and the longitudinal-twisting (L-T) vibration device were both developed for comparison of their effects on flexible microprobe implantation. Due to the long planar shaft topology of our developed neural microprobe, the longitudinal-twisting harmonic vibration can be actuated using a longitudinal-torsional transducer developed in Chapter 5 and [113,116], as shown in Figure 6.2 (a). An aluminum shell was designed to fix the transducer at its flange region. The longitudinal (L) vibration transducer was also designed with the same critical dimensions, as shown in Figure 6.2 (b). We used the same size of flange and the total length, only replacing the waveguide structures with a solid cylinder, as shown in Figure 6.2 (b). The same four pieces of longitudinal polarized piezoelectric ceramics were used in the longitudinal vibration transducer. The longitudinal transducer was fabricated

using conventional machining methods with Al 6061. The commercial Luer lock connector was used for both devices to adapt various neural microprobes by clamping their printed circuit board (PCB).

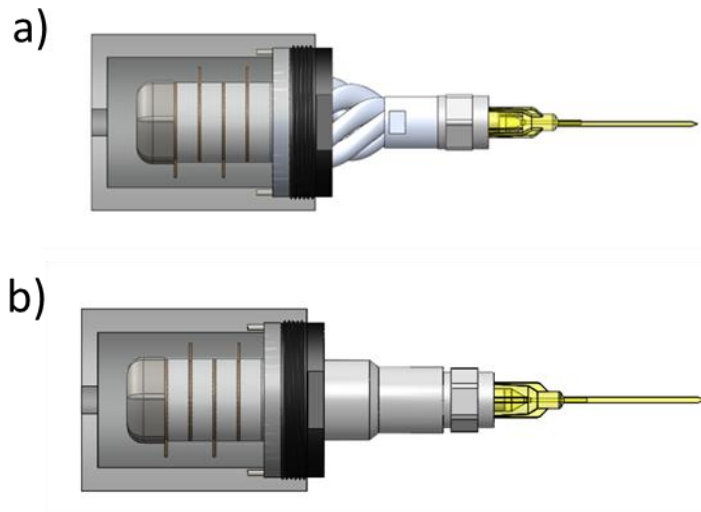


Figure 6.2 Models of vibration-assisted neural probe insertion devices. (a) Longitudinal-Twisting (L-T) vibration, (b) Longitudinal (L) vibration.

6.2.3 Finite Element Analysis

To explore the ultrasonic vibration performance of the flexible neural microprobe, finite element (FE) models were conducted for analyzing the steady-state behaviors using ANSYS 19.2 Workbench FE analysis software. To analyze the three-dimensional vibration of the probe vibration design, FE modeling is used to analyze the harmonic response and to predict the vibration shape and resonance frequency. Table 6.1 shows the material properties used for FE analysis.

Table 6.1 Material properties for the FE models of the ultrasonic devices.

Material	Density (kg/m ³)	Young's modulus (GPa)	Poisson's ratio
Al 6061	2700	76	0.33
AlSi10Mg	2670	75	0.33
1045 Steel	7800	210	0.3
PZT-8	7600	/	0.32
PET Film	958	1.08	0.418

In this paper, a 0.5 mm thick Polyester (PET) dummy probe with a height-to-width ratio of 14.5 was first designed and used in the FE models. This dummy probe will be laser-cut and used in the following experiments. In the vibrational FE analysis, one of the boundary conditions assumed is that the flange of the transducer is fixed. The Piezo and MEMS module embedded in the ANSYS 19.2 Workbench was used for FE piezoelectrical simulation. An exciting voltage of 200 V_{p-p} (Peak-to-Peak voltage) was applied to the piezoelectric ceramic rings to simulate the actual power level in vibrations.

Figure 6.3 shows an example of the harmonic response analysis results for both longitudinal-twisting and longitudinal ultrasonic vibration devices. The transducers frequencies for both devices were set at their resonant frequency. The flexible electrode probes were driven to achieve the highest longitudinal-twisting vibration and the longitudinal vibration, as shown in Figure 6.3. The oscillation wave propagates along with the long shaft structure of the probe, forming multiple oscillation sections. At around 58.5 kHz, the longitudinal vibration and longitudinal-twisting vibration have a similar vibration amplitude. These two vibration devices are used in the experiments discussed in later sections.

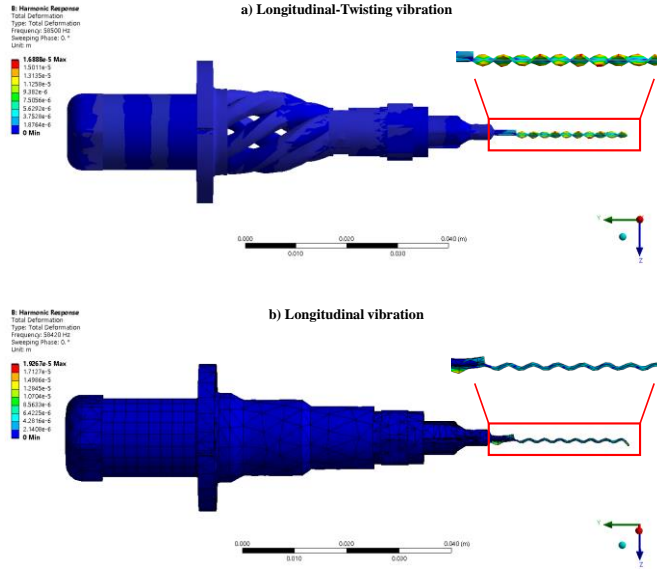


Figure 6.3 The harmonic response analysis results for both ultrasonic devices. (a) Longitudinal-Twisting vibration, (b) Longitudinal vibration.

6.3 Improve Insertion Stiffness with Bio-dissolvable PEG Guide

To increase the stiffness and implantation success rate, in this paper, a bio-dissolvable insertion guide is also proposed by using bio-dissolvable material, Polyethylene glycol (PEG), that can be easily dissolved by adding saline after flexible neural microprobe implantation. The insertion guide serves a similar function as the labium to guide and strengthen the flexible needle during insertion, as shown in Figure 6.4. The insertion guide first provides a guide function at the entry position. Due to the internal stress generated during the fabrication process discussed in Chapter 3, the real flexible neural microprobes are usually not really straight after being released from the wafer fabrication, as an example shown in Figure 6.5. The curved neural probe also worsens the bending and difficulty in implantation. The critical buckling load $F_{critical}$ of the microprobe can be analyzed by assuming it as an ideal beam (see Figure 6.4). The critical buckling load $F_{critical}$ of an electrode can be formulated as follow:

$$F_{critical} = \frac{\pi^2 EI}{(KL)^2} \quad (6.11)$$

Where E is Young's modulus of the probe, I is the area moment of inertia of the cross-section of the planar probe, KL is the effective length. By bracing the flexible neural microprobe at its end position using the insertion guide (see Figure 6.4), its equivalent effective length KL can be reduced, thereby enhancing the stiffness of the flexible neural probe.

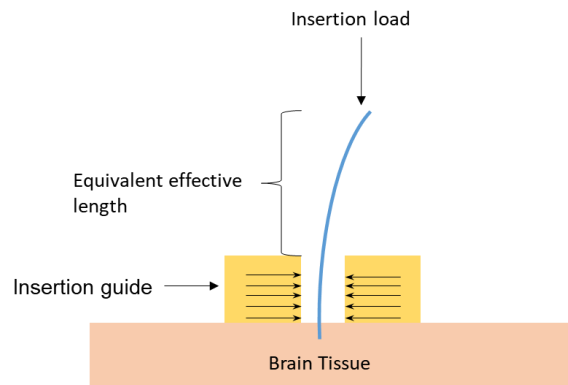


Figure 6.4 Illustration of an insertion guide reducing the equivalent effective length.

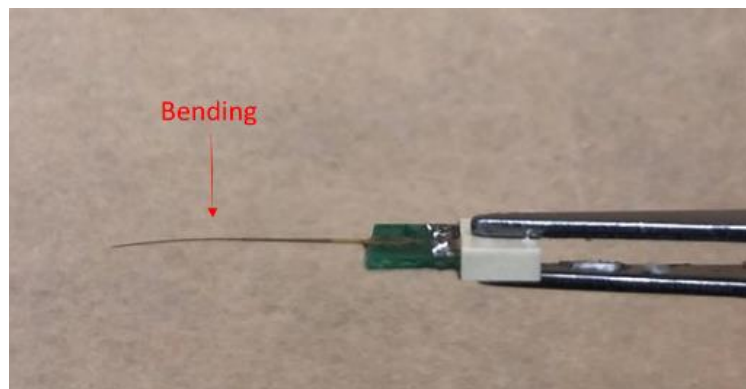


Figure 6.5 An example of a real bent neural microprobe.

Since the neural microprobe needs to remain in the brain after implantation, physically removing the guide after implantation is another challenge during the surgery to avoid any further brain tissue damage. To solve the issue, bio-dissolvable materials are a good choice to fabricate the guide structure, which can be removed by dissolving it during the surgery.

Polyethylene glycol (PEG) is a polyether compound with favorable biocompatibility and dissolvability, which is widely employed in biological and medical applications. The unique dissolvability of PEG allows it to be easily dissolved by saline. Depending on its molecular weight, the PEG shows different physical forms and mechanical properties. To balance the strength and dissolvability of the guide structure, Carbowax™ PEG 4000 is selected as the guide material, which is a waxy solid form at room temperature. The waxy property also provides a lubrication function during the insertion. The PEG guide design used in electrode probe brain insertion is shown in Figure 6.6. By using the guide, the lateral deflections of the flexible microprobe can be prevented during probe insertion. The Carbowax™ PEG 4000 has a low melting point of around 53 °C. This favorable property allows the PEG guide to be fabricated by a casting process. This reproducible method can be scaled up easily for various types of flexible neural microprobes to improve their implantation success rate. Based on the size of flexible neural microprobes, the PEG guide can be made to various diameters and thicknesses. Detailed fabrication information of the PEG guide is discussed later in Section 6.4.2. Once the insertion procedure is complete, the phosphate-buffered saline (PBS) can be used to dissolve and flush the PEG guide away.

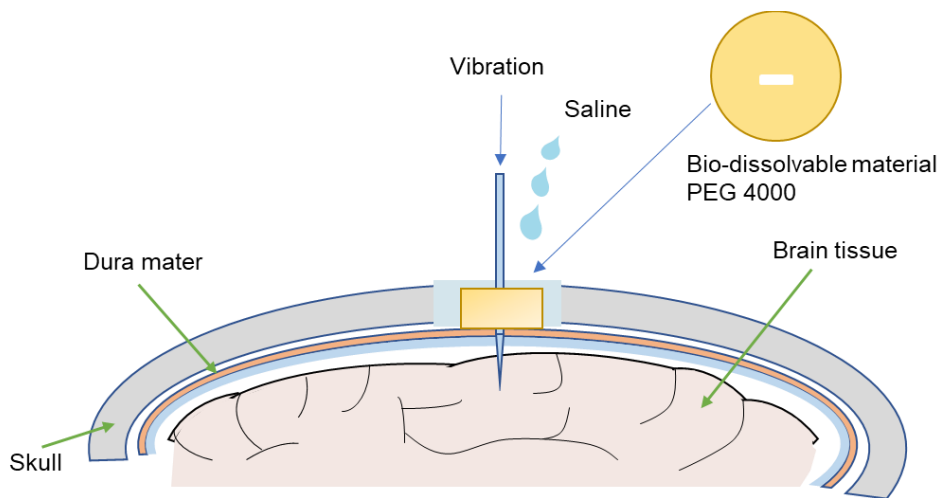


Figure 6.6 The illustration of the PEG insertion guide.

6.4 Experiments and Discussions

Laboratory experiments were first conducted to validate the design and development of our device. As shown in Figure 6.7, an experimental neural probe implantation platform was developed at our lab. A six-axis force sensor (ATI® gamma series, 60Hz) was used to record the force data during the insertion experiments. A 3D printed plastic fixture was mounted on the force sensor to hold a phantom tissue. To perform the insertion process, a linear motor (FUYU® FLS40) was controlled using a Raspberry Pi programmed with Python language. The vibratory insertion device was built on a linear guide with a 3D-printed plastic fixture. A PiezoDrive® PDUS210 driver was used to analyze the on-site impedance and to drive the ultrasonic transducer with adjustable variant voltages. The ultrasonic driver can continuously track the frequency shift during the insertion to ensure the ultrasonic device operating at full performance. For the in vitro experiments, agarose gels have been widely considered to be a viable model of the physical characteristics of the brain [117,118]. In this paper, 4% agarose gel was used to make the tissue phantom to mimic the brain tissue strength property. A PET dummy probe cut by laser (Glowforge 3D laser printer) was used and connected to the ultrasonic transducer (see Figure 6.7) for experiments.

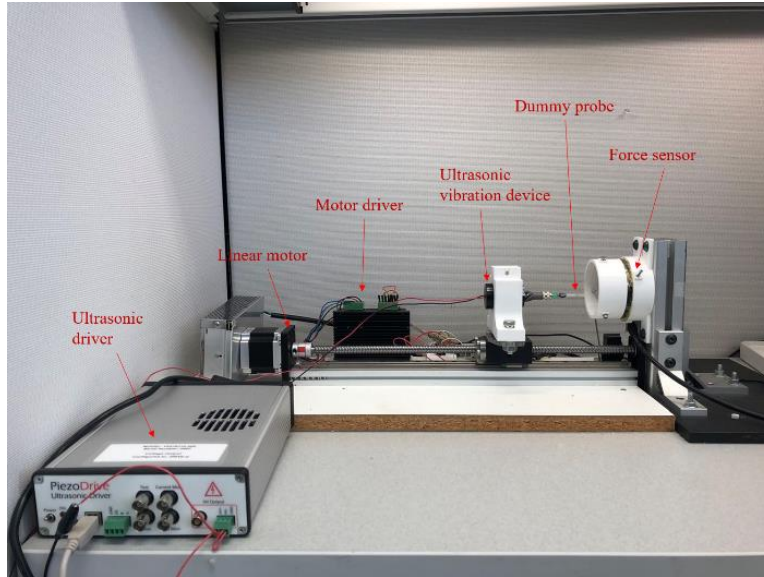


Figure 6.7 The experiment setup for neural probe implantation.

6.4.1 Insertion Force under the Ultrasonic Vibration

Insertion forces were investigated under three scenarios: (i) with longitudinal (L) vibration, (ii) with longitudinal-twisting (L-T) vibration, and (iii) without vibration. Given the friction force is affected by the velocity ratio ζ mentioned earlier in Equation (6.7), four different insertion speeds of 0.2 mm/s, 0.4 mm/s, 0.8 mm/s, and 2.0 mm/s were selected for experiments based on the operations in the real surgery [119], while regulating the vibration power constant at 200 V. For each condition, the experiments were repeated three times each for sampling.

The experiment results and their comparisons are shown in Figure 6.8, Figure 6.9, and Figure 6.10. Figure 6.8 shows the measured insertion force vs. probe insertion depth for three mentioned different scenarios (using 0.4 mm/sec for comparison). As shown in Figure 6.8, three typical puncture phases can be successfully identified during the insertion procedure. In Figure 6.8, the first phase is a pre-puncture, which begins with the probe touching the tissue phantom before a puncture occurs. The pre-puncture force continuously increases until the tissue phantom is cut through by the inserted electrode probe. In this phase, the puncture force can be reduced by

both the longitudinal vibration (45.4%) and the longitudinal-twisting vibration (47.9%) with an insertion speed of 0.4 mm/s, as shown in Figure 6.9. Figure 6.9 shows, as the insertion speed increase, the puncture force reduction rate decrease. The puncture force can be reduced as high as 48% with the longitudinal-twisting vibration at 0.4 mm/s. The puncture force reduction rate at 0.2 mm/s is not better than which at 0.4 mm/s, while theoretically lower speed has a higher reduction rate. This may be due to the fact that the original puncture force is already small, and other factors contributed to the puncture force cannot be reduced by the ultrasonic, such as the axial pressure of the probe.

In the second phase of the puncture (see Figure 6.8), the probe punctures and continuously inserts into the tissue phantom. As shown in Figure 6.8, there is a drop in the insertion force caused by surface membrane stress release. The third phase is the post-puncture phase (see Figure 6.8). In this phase, the insertion force continuously increased to the maximum insertion force, which is primarily caused by the increase of friction force. As the flexible electrode probe penetrates deeper with increasing friction force, buckling may occur when the insertion force is larger than the critical force of the probe. The buckling can be detected by the wavy shape insertion force, as shown in Figure 6.8. From Figure 6.8, it is clear that the insertion with the longitudinal-twisting vibration has the lowest overall insertion force than the other two scenarios. Other insertion speed experiments also confirm the same observation.

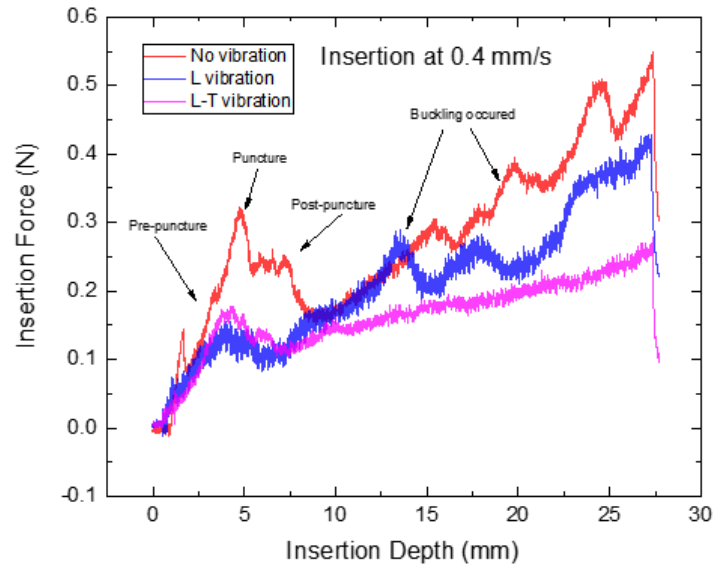


Figure 6.8 Insertion force measurements at 0.4 mm/s insertion speeds with longitudinal vibration, longitudinal-twisting vibration, and no vibration.

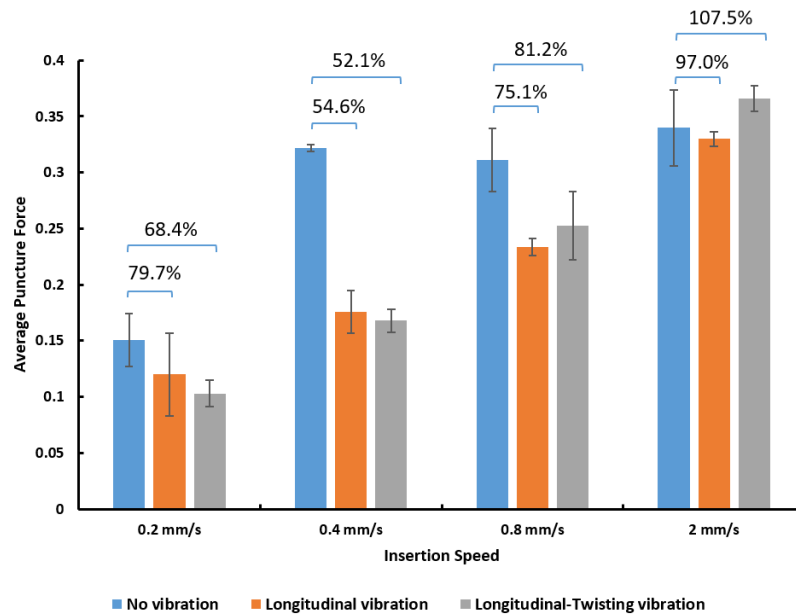


Figure 6.9 Relationship between the puncture force and insertion force.

Figure 6.10 shows the comparison of the recorded maximum insertion forces of three different scenarios with different insertion speeds. As shown in Figure 6.10, the longitudinal-twisting vibration has the largest insertion force reduction rate among all three scenarios with

different insertion speeds. In the comparison shown in Figure 6.10, the longitudinal-twisting vibration can achieve a 48.9% reduction of insertion force at 0.4 mm/s insertion speed.

From Figure 6.10, it is noticed that, when the insertion speed exceeds 2.0 mm/s, the ultrasonic vibration has comparatively less effective in reducing the insertion force. This observation actually confirms our Equation (6.8) when a high-velocity ratio ζ becomes large ($\zeta > 1.0$), the friction force reduction effect is reduced. To use ultrasonic vibration to reduce the flexible probe insertion, the velocity ratio ζ should be less than 1.0 ($\zeta < 1.0$).

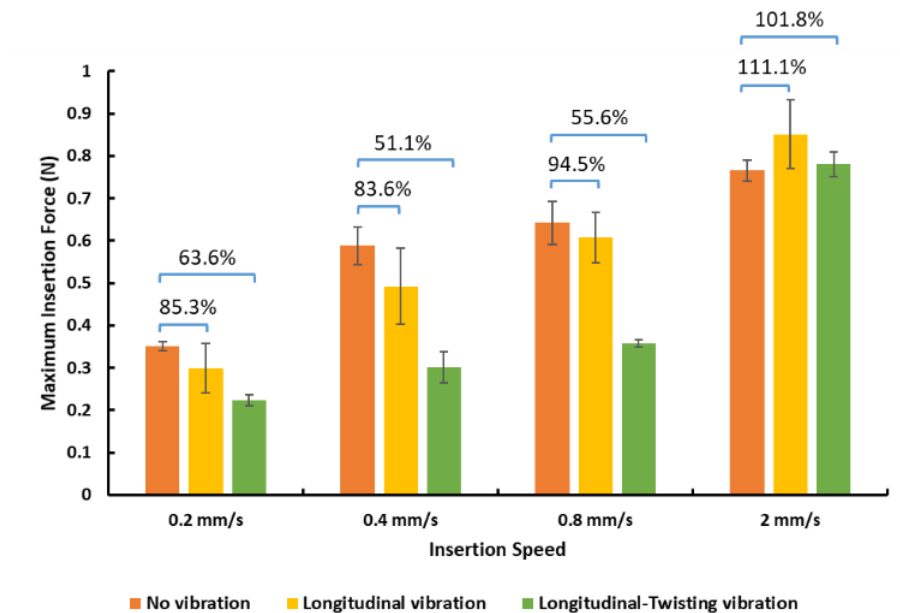


Figure 6.10 Maximum insertion force at different insertion speeds.

Figure 6.11 shows the insertion force reduction under different voltages (i.e., output power level) of ultrasonic vibrations. We used the output of 50 V, 100V, 150V, and 200V driving voltages for experiments. Figure 6.11 shows that as the driving voltage increases, the L&T ultrasonic vibration achieves a better insertion force reduction. This observation confirms the same reasoning earlier by Equation (6.7) and Equation (6.10). Using higher driving voltage

generates higher vibration amplitudes in both longitudinal and twisting directions, and that leads to better force reduction.

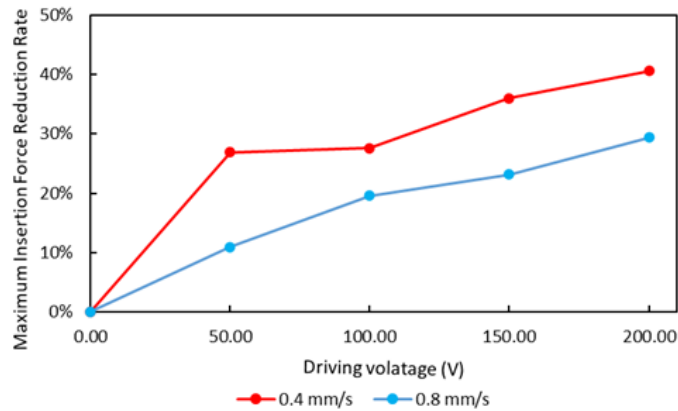


Figure 6.11 Relative reductions of insertion forces at different ultrasonic driving voltages.

6.4.2 Insertion with Bio-dissolvable Guides

The PEG guide structure was fabricated using a casting process. The material of Carbowax™ PEG 4000 was melted at around 53°C on the hot plate and poured into a pre-machined acrylic mold to cool and solidify at room temperature. Figure 6.12 shows an example PEG guide compared to the size of a nickel. The objective of this experiment is to prove our idea with a comparatively larger guide ratio of (guide thickness/probe length). The exact guide size for surgery can be smaller using the same fabrication method.



Figure 6.12 The casted PEG insertion guide.

As discussed above, the insertion PEG guide can increase the stiffness of the flexible probe by reducing its equivalent effective length in buckling. To investigate their relation, a six-axis force sensor was used to perform and record data from the compression buckling experiments at our lab, as shown in Figure 6.13. A dummy probe was compressed 2 mm axially at a constant speed of 0.2 mm/s with different thick insertion guides. The PEG guide thicknesses of 0.1", 0.2", 0.3", and 0.4" were used and tested in the experiments.

Figure 6.14 shows the critical buckling starting points of the same probe with different guide thicknesses. In Figure 6.14, the compression load increases rapidly to nearly the peak value where buckling starts, and then reaches a plateau in force. The buckling starting point represents the first buckling critical load of the probe, as mentioned earlier in Equation (6.11). As the thickness of the guide increases, the total compression loads required to buckle the probe also increase. In other words, the stiffness of the probe is proportional to the increase of the guide thickness.

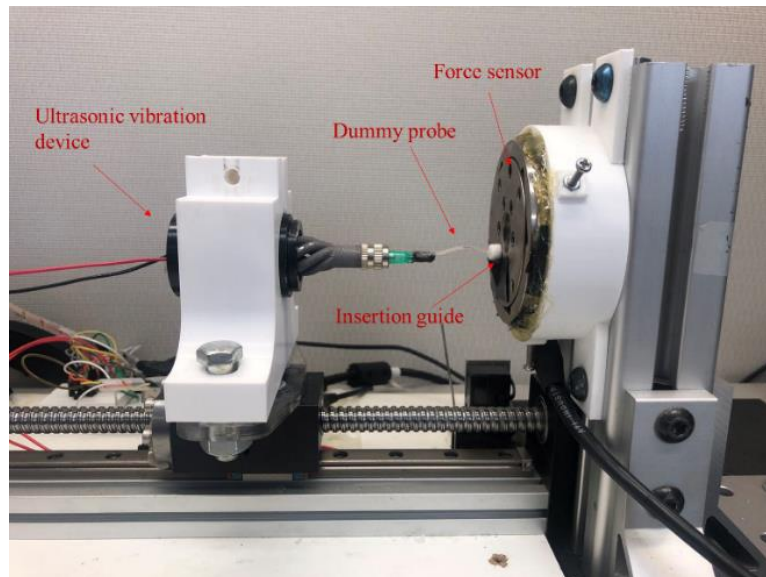


Figure 6.13 Experiment setup of probe compression test with a six-axis force sensor.

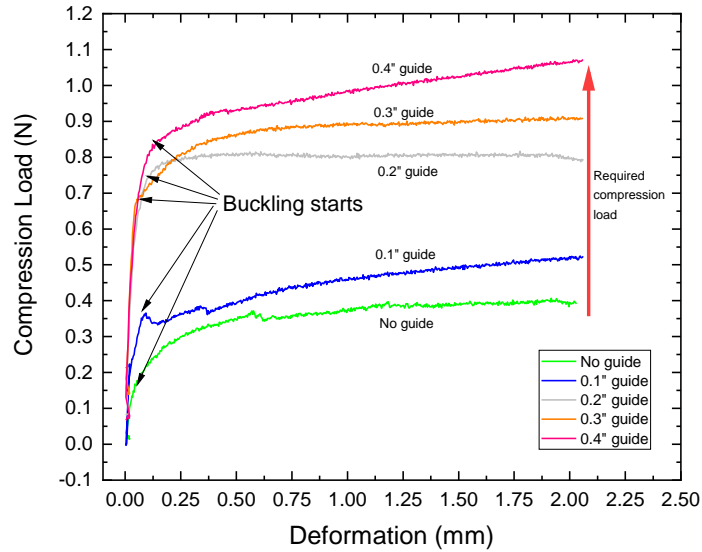


Figure 6.14 Compression buckling testing results with different thick guides.

Figure 6.15 shows the strong co-relationship between the force reduction enhancement versus the guide ratio of (guide thickness/probe length). As shown in Figure 6.15, there is a strong linear relation (Mean Square Error R-Square = 0.9895) between the force enhancement (vertical axis) and the horizontal axis of the support length ratio of (guide thickness/probe length). Although the thicker PEG guide can improve the stiffness of the probe, it also may limit the probe's feasible implantation depth. A good solution is using a thick bio-dissolvable PEG guide but dissolving it during the insertion.

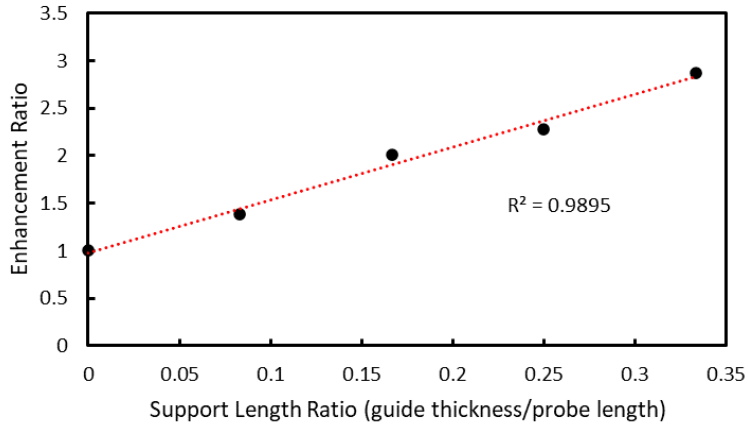


Figure 6.15 The relationship between the enhancement ratio and the support length ratio (guide thickness/probe length).

Figure 6.16 shows the influence of using the longitudinal-twisting vibration and the PEG guide on the compression buckling force. From Figure 6.16, one can find that the probe insertion with the L&T vibration and PEG guides can prevent buckling with a higher critical buckling load of the probe. In other words, by combining the L&T vibration and the insertion guide in flexible electrode insertion, one can improve the chance of the flexible electrode probe accurately reaching the target locations of brain tissue during flexible probe insertion.

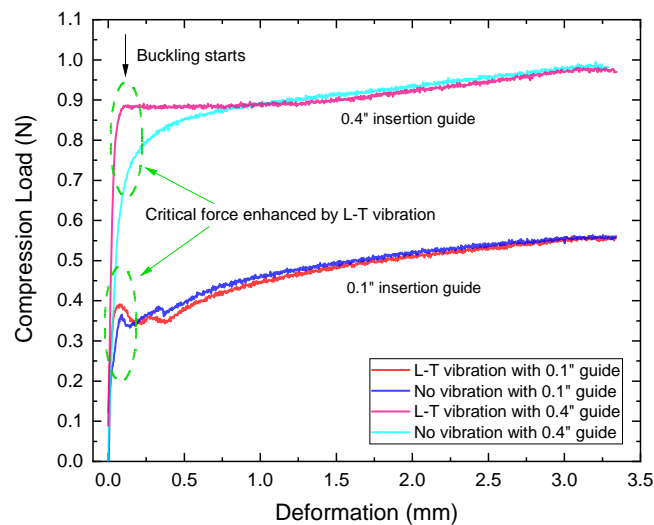


Figure 6.16 Compression buckling test under the influence of L&T vibration.

6.4.3 Insertion Performance with Two Strategies

Figure 6.17 shows a comparison of flexible probe insertions with the mentioned different scenarios. As shown in Figure 6.17, flexible probe insertion with both longitudinal-twisting vibration and insertion guide achieves the best result. The other scenarios show pretty serious tissue damages and probe deflection during the probe insertions (see Figure 6.17). The dummy probe was inserted into a 4% agarose tissue phantom to 25 mm in depth at 0.4 mm/s, then retracted at 1.0 mm/s. The longitudinal-twisting vibration was driven at 200 V. The thickness of the guide structure is 0.3", which is around 25% of the dummy probe. As shown in Figure 6.17, without using any vibration or without using a guide, the insertion traces have the largest fracture regions (about 2.09 mm width measured by microscope) and random variant deflection directions. That is because as the probe insertion depth increases, the probe bent multiple times due to the increase in friction. At the same time, the bent probe enlarged the opening by pushing one side of the phantom tissue, and it also changed the probe tip direction, causing a larger fracture. When a longitudinal-twisting vibration was applied, the result was between the previous two scenarios. The width of fracture regions under the effects of L&T vibration is about 0.87 mm.

It is observed that, while the ultrasonic vibration reduces the insertion force and slightly increases the stiffness, there is still a deflection during insertion due to the initial entry position and slight buckling. Without using any insertion guide, the deflection of the probe is around 4°-7°, as shown in Figure 6.17. When both the guide and ultrasonic L&T vibration were applied, an almost perfect insertion was achieved (only about 1° in deflection), as shown in Figure 6.17. This observation confirms that the proposed guide structure directs the entry position and reduces the equivalent effective length, thereby preventing buckling. At the same time, the ultrasonic vibration reduces friction force and insertion force. No obvious phantom tissue damage appeared.

The width of the insertion trace is about 0.52 mm, which is almost the same as the dummy probe thickness. Therefore, the combined strategy greatly can effectively improve the insertion performance of the flexible probe.

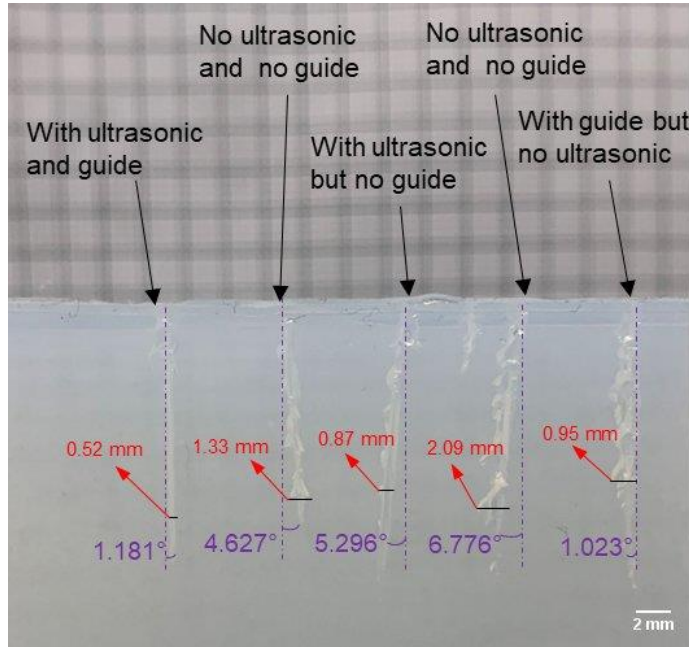


Figure 6.17 Insertion experiments in 4% Agarose gel with different implantation strategies.

As shown in Figure 6.18, the fabricated neural microprobes were also tested to be inserted with and without L&T ultrasonic vibrations on 0.7% agarose tissue phantom. The stiffness of the agarose tissue phantom is slightly tougher than the stiffness of the neural microprobe, which mimics the dura mater. The insertion speed is 0.1 mm/s. It can be seen in Figure 6.18(a) that without ultrasonic vibration, the neural microprobe can't penetrate the phantom tissue. On the other hand, with the assistance of L&T vibration (200 V at 56 kHz), the neural microprobe is able to be inserted into the phantom tissue, as shown in Figure 6.18(b). Although there is a deflection of insertion, this could be due to the original bending of the neural microprobe and the

initial insertion position. The results shown in Figure 6.18 demonstrate the feasibility of the ultrasonic vibration-assisted insertion of flexible needles into soft tissues.

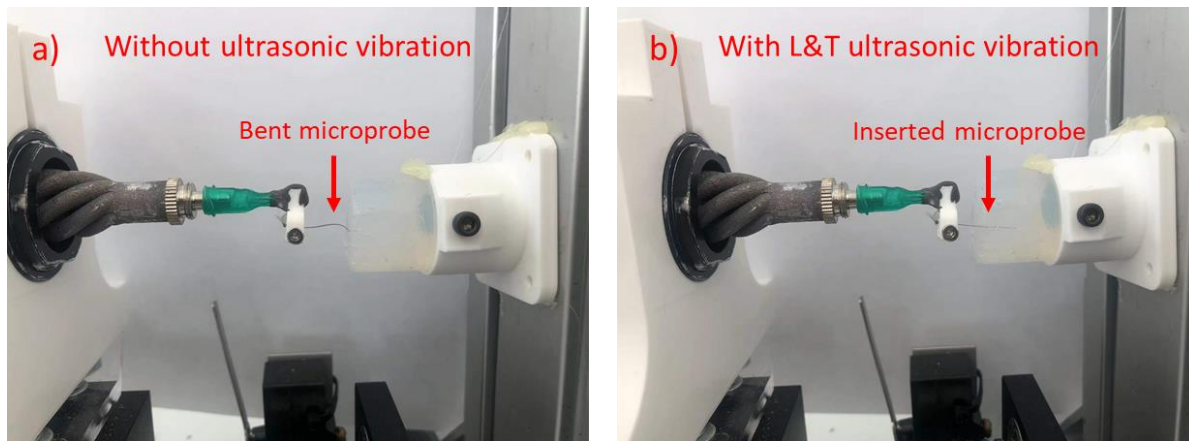


Figure 6.18 Insertion experiments using fabricated neural microprobe.

6.4.4 In Vivo Experiments of Neural Microprobe Insertion

To further evaluate the effectiveness of our proposed techniques, in vivo implantation experiments were conducted on a female rat's brain, as shown in Figure 6.19. The experiment was carried out at the UNC Neurology and MRI Laboratory following the approved animal experiments protocol. Figure 6.19 shows the surgery set up at the lab. The presented longitudinal and torsional (L&T) vibration-assisted insertion device was mounted on a commercial stereotaxic frame (KOPF®) with a 3D printed plastic fixture, as shown in Figure 6.19. A neural microprobe holder with a Luer connector was designed and 3D printed to fix our neural microprobe shown earlier in Chapter 3. The neural probe was implanted at 0.1 mm/s. The L&T ultrasonic vibration

was applied with a power of 8.5 W (110 V) at 52 kHz. A camera was used in the surgery room to record the implantation procedure during the operations.

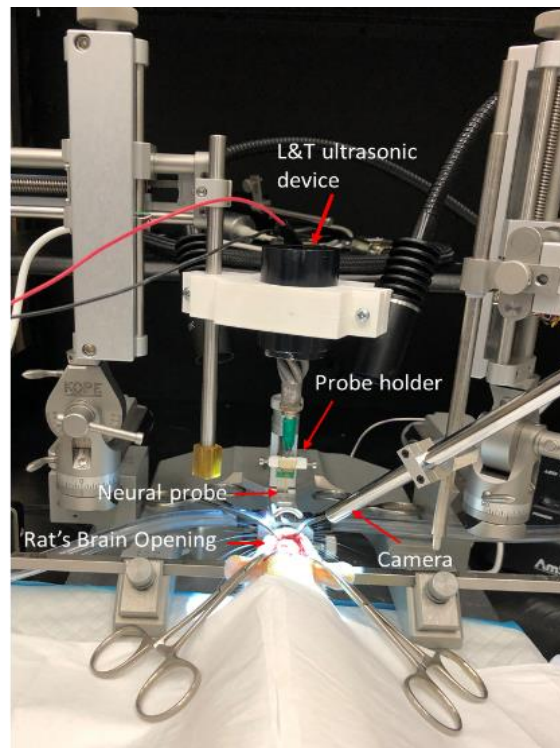


Figure 6.19 In Vivo experiment setup for neural probe implantation (at UNC neurology surgery room).

Figure 6.20 shows the screenshots taken from the recorded video of the neural probe insertions. Figure 6.20(a) shows the implantation without using vibration. Figure 6.20(b) shows the implantation by using the presented L&T ultrasonic vibration. Figure 6.20(c) shows a larger surface dimpling area without using the presented method, indicating larger tissue deformation and tissue damage caused by a large puncture force. Figure 6.20(d) shows a much smaller surface dimpling area on a rat's brain by using the presented longitudinal-twisting ultrasonic vibration assistance. A larger surface dimpling area indicates larger tissue deformation and corresponding stored energy, which will cause large puncture force and tissue damage after the puncture. The in vivo experiments clearly show the difference of neural microprobe insertions on rat brain tissue,

as shown in Figures 6.20(c) and (d). The in vivo result and comparison are shown in Figure 6.20 and also agree with our in vitro experiment results shown earlier in Section 6.4.1.

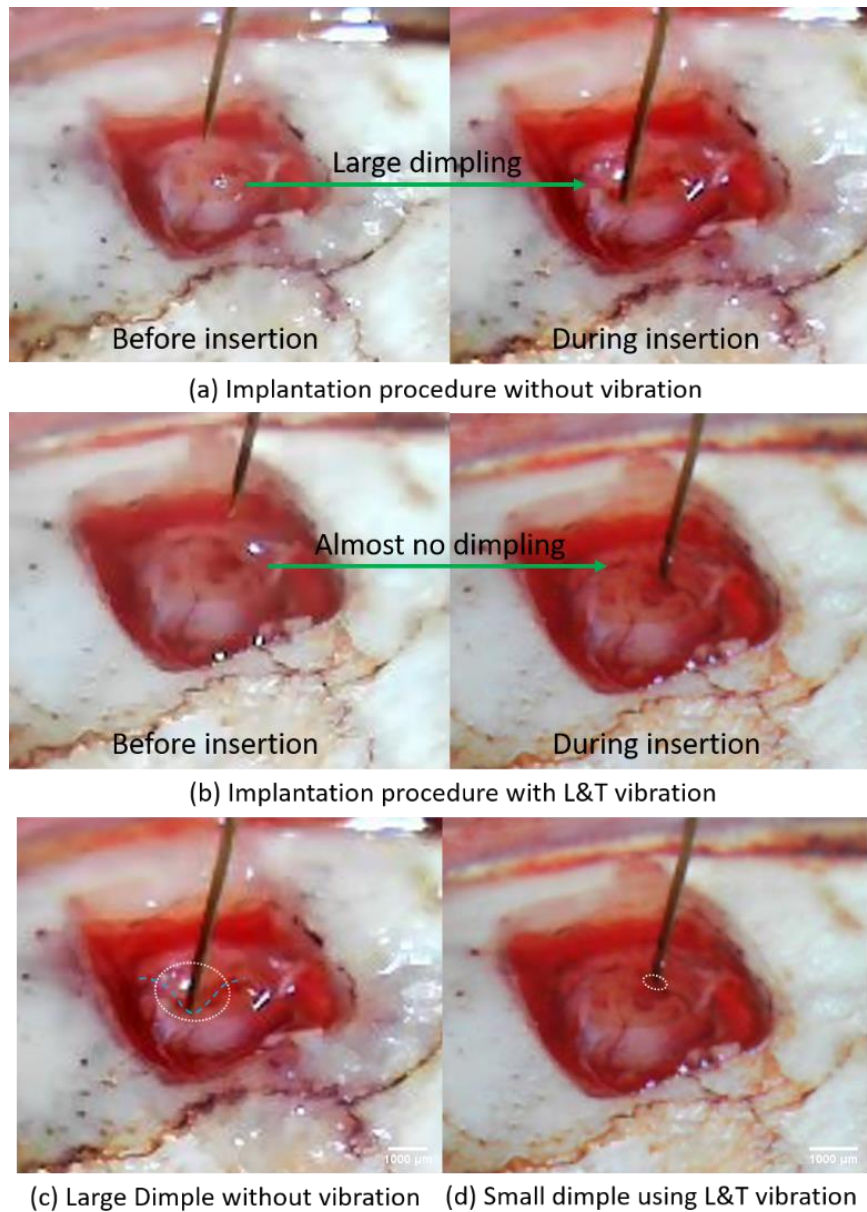


Figure 6.20 In vivo Implantation of Flexible neural probes on a rat's brain during surgery (at UNC neurology surgery room).

Figures 6.21-6.23 show the simultaneous DBS with fMRI performed to test the effectiveness of the fabricated neural microprobe. The neural microprobe was implanted on a rat's

brain and the experiment data was conducted and provided by Dr. SungHo Lee and Dr. Ian Shih at the Biomedical Research Imaging Center at UNC at Chapel Hill [84]. The experiments were conducted under the required Guide for the Care and Use of Laboratory Animals, as adopted by the National Institutes of Health, and with approval of the Institutional Animal Care and Use Committee at the University of North Carolina (UNC). The target brain area is the infralimbic area (IL, A25), subdivision of medial prefrontal cortex, to replicate the well-established brain activation pattern from the previous study [120] to validate its usefulness in brain modulation under an fMRI environment., as shown in Figures 6.21 – 6.23. In Figure 6.21, the thin black line indicates where the implanted microprobe is. During the fMRI, there are no large shadow artifacts shown, which also validates the fMRI compatibility of the fabricated neural microprobes.

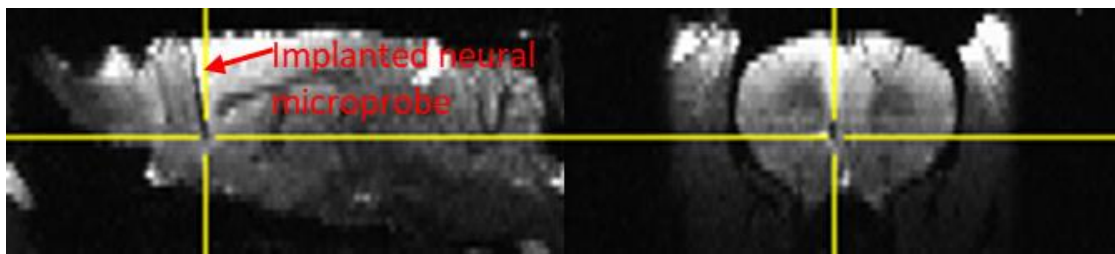


Figure 6.21 fMRI Image of the implanted neural microprobe.

In the experiments, we stimulated the deep brain target (IL, A25) and conducted fMRI. The fMRI was performed using a 9.4 T Bruker BioSpec system with a BGA-9S gradient insert (Bruker Corp., Billerica, MA) at the UNC Biomedical Research Imaging Center (BRIC). In this procedure, the rat was anesthetized with 0.5% isoflurane and 0.05 mg/kg/hour of dexmedetomidine. To compare the rest and stimulation period of the nervous system, a total of 3 stimuli were conducted. The current of each stimulus is 200 μ A with a frequency of 120 Hz and pulse width of 1 ms. The simulation period is 10 seconds followed by a 20 second resting period, as shown in Figure 6.22. Figure 6.22 shows the expected blood-oxygen-level-depend (BOLD)

responses measured by the fMRI. Figure 6.23 shows the images of fMRI results. The red regions indicate the high-level BOLD response during the stimulation. The activations of the anterior cingulate cortex (ACC), insula cortex, and mPFC contribute to the related cognitive function when stimulating the infralimbic area. This is a good way to help us map the network-level connectivity of the nervous system for future neuroscience studies and medical diagnosis.

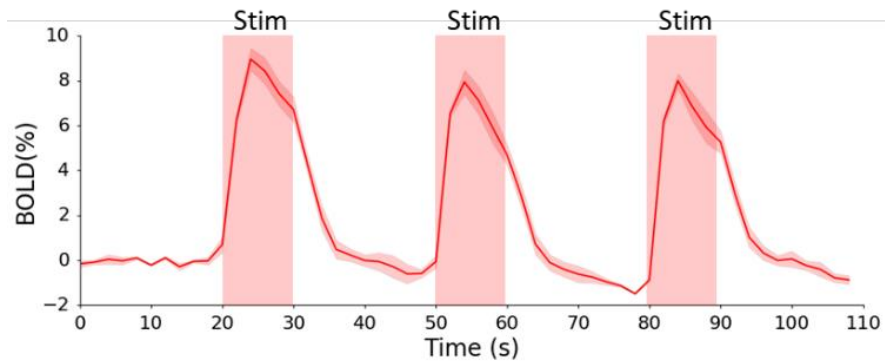


Figure 6.22 Results of simultaneous DBS and fMRI.

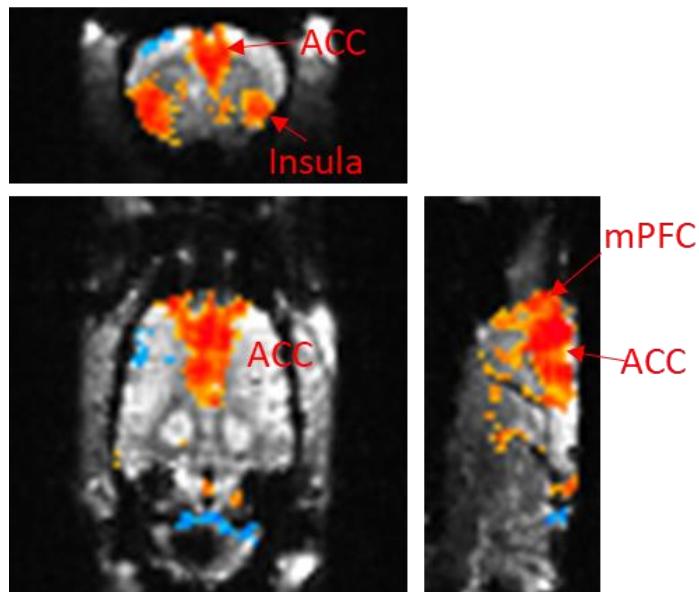


Figure 6.23 fMRI image during DBS on the infralimbic area (IL, A25).

6.5 Summary

In this chapter, we present a new strategy of using ultrasonic longitudinal-twisting vibration with a bio-dissolvable insertion guide for accurate flexible neural microprobe insertions. Using the three-dimensional longitudinal-twisting vibration can periodically change the resultant insertion velocity and the normal clamping force, and thus it can reduce the friction force of flexible electrode insertion. Analytic modeling and FE analysis of the design were presented. Using the waveguide-based L&T ultrasonic transducer in Chapter 5, an insertion device was developed for tissue insertion. To improve the stiffness of the flexible microprobe during insertion, a bio-dissolvable PEG guide was also proposed for flexible neural microelectrodes insertion. In vitro experiments demonstrate the effectiveness of the presented method. The experiments and observation also confirm that. Combining the L&T ultrasonic vibration and insertion guide, a minimum deflection and much less damaged implantation can be achieved. Both the in vitro and the in vivo experiments were conducted to validate the effectiveness of the presented longitudinal-twisting ultrasonic vibration, which demonstrates that our longitudinal-twisting vibration can minimize the surface dimpling, thereby reducing puncture force. The in-vivo experiments validate the effectiveness of our fabricated neural microprobes that can be used for the simultaneous DBS-fMRI for neuroscience studies and medical applications.

CHAPTER 7

CONCLUSIONS AND FUTURE WORKS

This chapter provides conclusions and limitations of the presented works, followed by the suggested future work directions.

7.1 Conclusions

This paper presents the design, fabrication, and implantation control of fMRI-compatible flexible neural microprobes that can be used under fMRI for neuroscience studies. The flexible neural microprobes can be used to investigate circuit-level modulation in a whole-brain scale. With the aim to develop an fMRI compatible flexible neural microprobe, the new design, material selection, and feasible microfabrication processes are investigated and presented in this paper.

Polyimide PI-2611 was adopted for the substrate and insulation layer of the neural microprobe. The cured PI-2611 has excellent mechanical properties, chemical properties, biocompatibility, and MRI compatibility. A compromised way of embedding a thin chromium reinforcement layer is adopted to slightly attenuate the stiffness of our microprobe for penetration while maintaining flexibility. According to the electrophysiological recording and fMRI compatibility requirements, the metals used for our microprobe are limited to very small solution possibilities. Because of the high chemical reactivity of chromium, chromium was adopted as reinforcement layer and adhesion layer of copper. Although copper has excellent electrical conductivity, it is not a good biocompatible metal and is easy to be corroded in the brain. Gold was deposited to encapsulate the copper layer due to its good biocompatibility and electrical conductivity, which also serve as the seed layer of gold electroplating for the electrode

modification. The gold electroplating generates a 3D mushroom shape on the electrode sites, which can improve the signal quality and selectivity. Due to the large thickness of the neural microprobe, laser ablation was used to define the profile. The neural microprobes were detached from the silicon carrier wafer by the anodic dissolution of sacrificial aluminum in a 10 wt% sodium chloride solution at a constant positive potential.

The neural microprobes were fabricated at our NNF cleanroom and bonded to customized PCB boards. The fabricated neural microprobes were then characterized before being implanted. Both SEM with EDS measurements was performed to structurally and chemically evaluate the neural microprobe. The measurement results show that the electroplated electrode sites possess a 3D mushroom shape which entirely encapsulates the electrode sites to increase the measurement sensitivity and corrosion resistance. Electrochemical impedance spectroscopy measurements show that the fabricated neural microprobe has low impedance for DBS and electrophysiological recordings. Tensile test and compressive test show that the embedded reinforcement layer is able to significantly improve the stiffness while maintaining good flexibility.

To overcome the implantation challenges of inserting a flexible neural microprobe, a waveguide-based longitudinal-excited L&T ultrasonic transducer was proposed and developed for ultrasonic vibration-assisted flexible microprobe implantation. For synchronization of both the longitudinal and the torsional vibrations, a new circular array of helical structures was designed as an effective waveguide, constraining wave propagations to achieve harmonic longitudinal and torsional vibration. Analytical modeling of the waveguide-based L&T transducer design was discussed. Due to the complex geometric shape, the SLM-AM was used to fabricate the L&T transducer with AlSi10Mg metal powders. Both the FE simulation and the laboratory experiments have demonstrated that the new waveguide-based L&T transducer can deliver

synchronized longitudinal and torsional vibrations at the same resonant frequency. The L&T conversion ratio varies at different resonant frequencies, which provide more application potentials. Impedance analysis and vibration characteristics of the SLM-AM prototype exhibits excellent electromechanical performance and acoustics characteristics.

The developed new L&T ultrasonic transducer is then integrated with a commercial Luer lock connector to adapt to ultrasonic vibratory implantation of various neural microprobes. The three-dimensional ultrasonic vibration periodically changes the resultant insertion velocity and the normal clamping force, and thus reduces the friction force of flexible microprobe insertion. Analytic modeling and FE analysis were presented in Chapter 6. To improve the stiffness of the flexible microprobe for deep implantation, a bio-dissolvable PEG guide was also proposed for flexible neural microelectrodes insertion, which can be fabricated using a casting process. The experiments and observation also confirm the effectiveness. Combining the longitudinal-twisting ultrasonic vibration and insertion guide, a minimum deflection and much less damaged implantation can be achieved. Both the in vitro and the in vivo experiments were conducted to validate the effectiveness of the presented longitudinal-twisting ultrasonic vibration. The developed neural microprobe can successfully be implanted into the rat's brain by combining the L&T ultrasonic vibration and bio-dissolvable insertion guide. The promising strategy is readily scaled up for various types of flexible neural probes to improve the implantation performance and success rate.

7.2 Limitations

Although the fMRI compatible flexible neural microprobe was presented and successfully implanted into the rat's brain, some limitations are still worth mentioning as below.

Based on the current fabrication procedure, the fabrication yield rate is about 50-60%, which is less than what we expected. The main issue occurs at the circuit trace layer patterning. To ensure a low impedance of electrodes, a total of 900 nm thick metal stack [100 nm Cr/ 700 nm Cu/ 100 nm Au] was sequentially deposited. The thick metal stake increases the difficulty of deposition and patterning. To pattern the circuit layer with a lift-off process, E-beam deposition was used to obtain a directional deposition for a better lift-off result. However, metals deposited by the E-beam evaporator have weak adhesion to polyimide, resulting in a failure of the patterning. Due to the large thickness of the metal layer, the thickness ratio between the lift-off photoresist and the metal layer is relatively low, which decreases the success rate of the lift-off process. Later, a bi-layer lift-off process with a sputtering deposition can be tested to increase the fabrication success rate.



Figure 7.1 Photo of a failed lift-off circuit trace layer.

To define the profile of our microprobes, we are currently using the UV laser ablation process. Although laser ablation is a maskless process, the processing accuracy is still lower than the deep dry etching process due to the diameter of the laser spot and the positioning accuracy of the tool. In addition, during the ablation, a carbonization line was generated, which may cause circuit shorting when bonding the microprobe to PCB. A feasible DRIE process still needs to be explored, including the etching gases composition, hard mask patterning, hard mask selectivity, and sidewall slope control. It is worth noting that the quality of the sidewall may also affect insertion performance and tissue damage. More related research is necessary to be conducted in the future.

In this paper, the commercial Luer lock connector was used to adapt various types of neural microelectrodes or needles [121]. When high power was applied to the L&T ultrasonic transducer, the temperature at the Luer lock connector joint rapidly rose, as shown in Figure 7.2. The high-frequency and large-amplitude vibration generates a lot of heat in the joint region, due to the large acoustic resistance of the interface between different materials (metal male Luer connector and 3D printed female Luer connectors). To avoid this, in the future, the assembly

design between the neural microprobes and ultrasonic transducer needs to be optimized, and the metal Luer connector could be used for similar ultrasonic applications.



Figure 7.2 High power ultrasonic vibration causes the failure of a plastic Luer connector.

7.3 Future Works

The design and manufacturing of diverse neural microelectrodes and peripheral devices (e.g., implantation devices, headstage, etc.) for various neural-related applications are one of the pilot research topics, showing significant growth potentials. In the future, there are still many valuable research works to be explored. Some potential research directions are listed below.

1) Electrode Modification

Owing to the surface quality of the electrode directly associated with the signal quality and immune response, electrode modification techniques need to be further explored. Currently, we only applied the gold electroplating to modify the electrode sites, but other materials and techniques could be studied to further decrease the impedance and increase measurement selectivity. As mentioned in Chapter 2, some biocompatible and conductive polymers are excellent candidates, which also enable a longer electrode life. For instance, PEDOT can be deposited on our electroplated gold electrodes to further improve the signal quality and electrode

life. One of future research is to study the materials and modification methods to further improve the neural microelectrode performance.

2) Clinical Study

More clinical studies are needed to further validate the effectiveness of our developed neural microprobe and presented strategies. Since the neural microprobe requires remaining in the brain for the long term, the stability of the neural microprobe and chronic response need to be tested. Immunohistological assessment is a useful indicator to validate the effectiveness of our implanted neural microprobe. For example, the change in the presence of reactive astrocytes (GFAP+) and macrophages (CD68+) can be investigated after the neural microprobe implantation. In addition, the signal quality of the implanted microprobe can be measured regularly to estimate its life span. Clinical studies are able to provide us with more information to further improve our neural microprobe fabrication and implantation strategies.

3) Other Types of Neural Microprobes and Applications

In this paper, only one fMRI compatible flexible neural microprobe was designed and developed. In the future, more advanced neural microelectrodes and wearable flexible biosensors for the brain-computer interface and neural medical applications can be developed based on the current fabrication foundation. These types of neural microelectrodes would be potentially applied in different scenarios, such as DBS, drug delivery, and other brain-machine interfaces. In addition, advanced smaller flexible neural microprobe with denser electrodes could be developed for higher measurement accuracy for neuroscience and medical applications.

REFERENCES

- [1] Cheung, K. C., 2007, “Implantable Microscale Neural Interfaces,” *Biomedical Microdevices*, 9(6), pp. 923–938.
- [2] Albaugh, D. L., and Shih, Y.-Y. I., 2013, “Neural Circuit Modulation During Deep Brain Stimulation at the Subthalamic Nucleus for Parkinson’s Disease: What Have We Learned from Neuroimaging Studies?,” *Brain Connectivity*, 4(1), pp. 1–14.
- [3] Van Den Berge, N., Albaugh, D. L., Salzwedel, A., Vanhove, C., Van Holen, R., Gao, W., Stuber, G. D., and Shih, Y.-Y. I., 2017, “Functional Circuit Mapping of Striatal Output Nuclei Using Simultaneous Deep Brain Stimulation and fMRI,” *NeuroImage*, 146, pp. 1050–1061.
- [4] Rezai, A. R., Finelli, D., Nyenhuis, J. A., Hrdlicka, G., Tkach, J., Sharan, A., Rugieri, P., Stypulkowski, P. H., and Shellock, F. G., 2002, “Neurostimulation Systems for Deep Brain Stimulation: In Vitro Evaluation of Magnetic Resonance Imaging-Related Heating at 1.5 Tesla,” *Journal of the International Society for Magnetic Resonance in Medicine*, 15(3), pp. 241–250.
- [5] Shellock, F. G., 2002, “Magnetic Resonance Safety Update 2002: Implants and Devices,” *Journal of Magnetic Resonance Imaging*, 16(5), pp. 485–496.
- [6] Piccolino, M., 1997, “Luigi Galvani and Animal Electricity: Two Centuries after the Foundation of Electrophysiology,” *Trends in Neurosciences*, 20(10), pp. 443–448.
- [7] Adrian, E. D. A., 1928, *The Basis of Sensation, the Action of the Sense Organs*, W. W. Norton & Company, inc., New York.
- [8] Patil, A. C., and Thakor, N. V., 2016, “Implantable Neurotechnologies: A Review of Micro- and Nanoelectrodes for Neural Recording,” *Medical & Biological Engineering & Computing*, 54(1), pp. 23–44.
- [9] Hubel, D. H., and Wiesel, T. N., 1959, “Receptive Fields of Single Neurones in the Cat’s Striate Cortex,” *Journal of Physiology*, 148(3), pp. 574–591.
- [10] Yuen, T. G. H., and Agnew, W. F., 1995, “Histological Evaluation of Polyestkimide-Insulated Gold Wires in Brain,” 16(12), p. 6.
- [11] Xindong Liu, McCreery, D. B., Carter, R. R., Bullara, L. A., Yuen, T. G. H., and Agnew, W. F., 1999, “Stability of the Interface between Neural Tissue and Chronically Implanted Intracortical Microelectrodes,” *IEEE transactions on rehabilitation engineering*, 7(3), pp. 315–326.
- [12] Nicolelis, M. A. L., Dimitrov, D., Carmena, J. M., Crist, R., Lehew, G., Kralik, J. D., and Wise, S. P., 2003, “Chronic, Multisite, Multielectrode Recordings in Macaque Monkeys,” *Proceedings of the National Academy of Sciences of the United States of America*, 100(19),

pp. 11041–11046.

- [13] Wolbarsht, M. L., Macnichol, E. F., and Wagner, H. G., 1960, “Glass Insulated Platinum Microelectrode,” *Science*, 132(3436), pp. 1309–1310.
- [14] Green, J. D., 1958, “A Simple Microelectrode for Recording from the Central Nervous System,” *Nature*, 182(4640), pp. 962–962.
- [15] Marg, E., and Adams, J. E., 1967, “Indwelling Multiple Micro-Electrodes in the Brain,” *Electroencephalography and Clinical Neurophysiology*, 23(3), pp. 277–280.
- [16] Du, M., Xu, X., Yang, L., Guo, Y., Guan, S., Shi, J., Wang, J., and Fang, Y., 2018, “Simultaneous Surface and Depth Neural Activity Recording with Graphene Transistor-Based Dual-Modality Probes,” *Biosensors and Bioelectronics*, 105, pp. 109–115.
- [17] Schmidt, E. M., McIntosh, J. S., Durelli, L., and Bak, M. J., 1978, “Fine Control of Operantly Conditioned Firing Patterns of Cortical Neurons,” *Experimental Neurology*, 61(2), pp. 349–369.
- [18] Rousche, P. J., and Normann, R. A., 1998, “Chronic Recording Capability of the Utah Intracortical Electrode Array in Cat Sensory Cortex,” *Journal of Neuroscience Methods*, 82(1), pp. 1–15.
- [19] Wise, K. D., Angell, J. B., and Starr, A., 1970, “An Integrated-Circuit Approach to Extracellular Microelectrodes,” *IEEE Transactions on Biomedical Engineering*, BME-17(3), pp. 238–247.
- [20] Rohatgi, P., Langhals, N. B., Kipke, D. R., and Patil, P. G., 2009, “In Vivo Performance of a Microelectrode Neural Probe with Integrated Drug Delivery,” *Neurosurgical Focus*, 27(1), p. E8.
- [21] Abidian, M. R., and Martin, D. C., 2009, “Multifunctional Nanobiomaterials for Neural Interfaces,” *Advanced Functional Materials*, 19(4), pp. 573–585.
- [22] Wise, K. D., Sodagar, A. M., Yao, Y., Gulari, M. N., Perlin, G. E., and Najafi, K., 2008, “Microelectrodes, Microelectronics, and Implantable Neural Microsystems,” *Proceedings of the IEEE*, 96(7), pp. 1184–1202.
- [23] Hong, G., and Lieber, C. M., 2019, “Novel Electrode Technologies for Neural Recordings,” *Nature Reviews Neuroscience*, 20(6), pp. 330–345.
- [24] Jun, J. J., Steinmetz, N. A., Siegle, J. H., Denman, D. J., Bauza, M., Barbarits, B., Lee, A. K., Anastassiou, C. A., Andrei, A., Aydın, Ç., Barbic, M., Blanche, T. J., Bonin, V., Couto, J., Dutta, B., Gratiy, S. L., Gutnisky, D. A., Häusser, M., Karsh, B., Ledochowitsch, P., Lopez, C. M., Mitelut, C., Musa, S., Okun, M., Pachitariu, M., Putzeys, J., Rich, P. D., Rossant, C., Sun, W., Svoboda, K., Carandini, M., Harris, K. D., Koch, C., O’Keefe, J., and Harris, T. D., 2017, “Fully Integrated Silicon Probes for High-Density Recording of Neural Activity,” *Nature*, 551(7679), pp. 232–236.

- [25] Kim, C., Jeong, J., and Kim, S. J., 2019, “Recent Progress on Non-Conventional Microfabricated Probes for the Chronic Recording of Cortical Neural Activity,” *Sensors*, 19(5), p. 1069.
- [26] Weltman, A., Yoo, J., and Meng, E., 2016, “Flexible, Penetrating Brain Probes Enabled by Advances in Polymer Microfabrication,” *Micromachines*, 7(10), p. 180.
- [27] Saxena, T., Karumbaiah, L., Gaupp, E. A., Patkar, R., Patil, K., Betancur, M., Stanley, G. B., and Bellamkonda, R. V., 2013, “The Impact of Chronic Blood-Brain Barrier Breach on Intracortical Electrode Function,” *Biomaterials*, 34(20), pp. 4703–4713.
- [28] Clarke, L. E., and Barres, B. A., 2013, “Emerging Roles of Astrocytes in Neural Circuit Development,” *Nature Reviews Neuroscience*, 14(5), pp. 311-321.
- [29] Biran, R., Martin, D. C., and Tresco, P. A., 2007, “The Brain Tissue Response to Implanted Silicon Microelectrode Arrays Is Increased When the Device Is Tethered to the Skull,” *Journal of Biomedical Materials Research Part A*, 82(1), pp. 169-178.
- [30] Sun, Z., Zhang, L., and Rose, J. L., 2005, “Flexural Torsional Guided Wave Mechanics and Focusing in Pipe,” *J. Pressure Vessel Technol.*, 127(4), p. 471.
- [31] Tooker, A., Madsen, T. E., Yorita, A., Crowell, A., Shah, K. G., Felix, S., Mayberg, H. S., Pannu, S., Rainnie, D. G., and Tolosa, V., 2013, “Microfabricated Polymer-Based Neural Interface for Electrical Stimulation/Recording, Drug Delivery, and Chemical Sensing - Development,” In 2013 35th Annual International Conference of the IEEE Engineering in Medicine and Biology Society (EMBC), pp. 5159-5162. IEEE, 2013.
- [32] Kim, G. H., Kim, K., Lee, E., An, T., Choi, W., Lim, G., and Shin, J. H., 2018, “Recent Progress on Microelectrodes in Neural Interfaces,” *Materials (Basel)*, 11(10).
- [33] Stieglitz, T., Beutel, H., and Schuettler, M., “Micromachined, Polyimide-Based Devices for Flexible Neural Interfaces,” *Biomedical Microdevices 2.4 (2000)*, pp. 283-294.
- [34] Rubehn, B., E. Wolff, S. B., Tovote, P., Lüthi, A., and Stieglitz, T., 2013, “A Polymer - Based Neural Microimplant for Optogenetic Applications: Design and First in Vivo Study,” *Lab on a Chip*, 13(4), pp. 579–588.
- [35] Altuna, A., Bellistri, E., Cid, E., Aivar, P., Gal, B., Berganzo, J., Gabriel, G., Guimerà, A., Villa, R., Fernández, L. J., and Menendez de la Prida, L., 2013, “SU-8 Based Microprobes for Simultaneous Neural Depth Recording and Drug Delivery in the Brain,” *Lab on a Chip*, 13(7), pp. 1422-1430.
- [36] Mercanzini, A., Cheung, K., Buhl, D. L., Boers, M., Maillard, A., Colin, P., Bensadoun, J.-C., Bertsch, A., and Renaud, P., 2008, “Demonstration of Cortical Recording Using Novel Flexible Polymer Neural Probes,” *Sensors and Actuators A: Physical*, 143(1), pp. 90–96.
- [37] Lai, H.-Y., Liao, L.-D., Lin, C.-T., Hsu, J.-H., He, X., Chen, Y.-Y., Chang, J.-Y., Chen, H.-F., Tsang, S., and Shih, Y.-Y. I., 2012, “Design, Simulation and Experimental Validation

- of a Novel Flexible Neural Probe for Deep Brain Stimulation and Multichannel Recording,” *Journal of Neural Engineering*, 9(3), p. 036001.
- [38] Musk, E. and Neuralink, 2019, “An Integrated Brain-Machine Interface Platform with Thousands of Channels,” *Journal of Medical Internet Research*, 21(10), p. 16194.
- [39] Szostak, K. M., Grand, L., and Constandinou, T. G., 2017, “Neural Interfaces for Intracortical Recording: Requirements, Fabrication Methods, and Characteristics,” *Frontiers in Neuroscience*, 11, p. 665.
- [40] Cogan, S. F., 2008, “Neural Stimulation and Recording Electrodes,” *Annual Review of Biomedical Engineering*, 10(1), pp. 275–309.
- [41] Meng, E., 2010, *Biomedical Microsystems*, CRC Press.
- [42] Chang, J. H., Lu, B., and Tai, Y., 2011, “Adhesion-Enhancing Surface Treatments for Parylene Deposition,” In 2011 16th International Solid-State Sensors, Actuators and Microsystems Conference, pp. 390–393.
- [43] Kim, S. H., Na, S. W., Lee, N.-E., Nam, Y. W., and Kim, Y.-H., 2005, “Effect of Surface Roughness on the Adhesion Properties of Cu/Cr Films on Polyimide Substrate Treated by Inductively Coupled Oxygen Plasma,” *Surface and Coatings Technology*, 200(7), pp. 2072–2079.
- [44] Von Metzen, R. P., and Stieglitz, T., 2013, “The Effects of Annealing on Mechanical, Chemical, and Physical Properties and Structural Stability of Parylene C,” *Biomedical Microdevices*, 15(5), pp. 727-735.
- [45] Atta, A., 2013, “Modification of the Surface Properties of Polyimide Films Using Oxygen Plasma Exposure,” *Applied Surface Science*, 255(18), pp. 8135-8144.
- [46] Chen, Y.-Y., Lai, H.-Y., Lin, S.-H., Cho, C.-W., Chao, W.-H., Liao, C.-H., Tsang, S., Chen, Y.-F., and Lin, S.-Y., 2009, “Design and Fabrication of a Polyimide-Based Microelectrode Array: Application in Neural Recording and Repeatable Electrolytic Lesion in Rat Brain,” *Journal of Neuroscience Methods*, 182(1), pp. 6–16.
- [47] Ludwig, K. A., Uram, J. D., Yang, J., Martin, D. C., and Kipke, D. R., 2006, “Chronic Neural Recordings Using Silicon Microelectrode Arrays Electrochemically Deposited with a Poly(3,4-Ethylenedioxythiophene) (PEDOT) Film,” *Journal of Neural Engineering*, 3(1), p. 59.
- [48] Yang, J., Kim, D. H., Hendricks, J. L., Leach, M., Northey, R., and Martin, D. C., 2005, “Ordered Surfactant-Templated Poly(3,4-Ethylenedioxythiophene) (PEDOT) Conducting Polymer on Microfabricated Neural Probes,” *Acta Biomaterialia*, 1(1), pp. 125–136.
- [49] Hashemi Noshahr, F., Nabavi, M., and Sawan, M., 2020, “Multi-Channel Neural Recording Implants: A Review,” *Sensors (Basel)*, 20(3), p. 904.

- [50] Mandarelli, G., Moretti, G., Pasquini, M., Nicolò, G., and Ferracuti, S., 2018, “Informed Consent Decision-Making in Deep Brain Stimulation,” *Brain sciences*, 8(5), 84.
- [51] Chen, X. L., Xiong, Y. Y., Xu, G. L., and Liu, X. F., 2013, “Deep Brain Stimulation,” *Interventional Neurology*, 1(3-4), pp. 200-212.
- [52] Crosson, B., Ford, A., McGregor, K. M., Meinzer, M., Cheshkov, S., Li, X., Walker-Batson, D., and Briggs, R. W., 2010, “Functional Imaging and Related Techniques: An Introduction for Rehabilitation Researchers,” *Journal of Rehabilitation Research and Development*, 47(2), vii.
- [53] Jech, R., 2008, “Functional Imaging of Deep Brain Stimulation: FMRI, SPECT, and PET,” In *Deep brain stimulation in neurological and psychiatric disorders* (pp. 179-201). Humana Press.
- [54] Carmichael, D. W., Pinto, S., Limousin-Dowsey, P., Thobois, S., Allen, P. J., Lemieux, L., Yousry, T., and Thornton, J. S., 2007, “Functional MRI with Active, Fully Implanted, Deep Brain Stimulation Systems: Safety and Experimental Confounds,” *Neuroimage*, 37(2), pp. 508–517.
- [55] Lee, J. H., Durand, R., Gradinaru, V., Zhang, F., Goshen, I., Kim, D.-S., Fenno, L. E., Ramakrishnan, C., and Deisseroth, K., 2010, “Global and Local FMRI Signals Driven by Neurons Defined Optogenetically by Type and Wiring,” *Nature*, 465(7299), pp. 788–792.
- [56] Jorgensen, S., 2016, Design and Testing of Microfabricated Surgical Tools for Large Animal Probe Insertion, Lawrence Livermore National Lab.(LLNL), Livermore, CA (United States).
- [57] Felix, S. H., Shah, K. G., Tolosa, V. M., Sheth, H. J., Tooker, A. C., Delima, T. L., Jadhav, S. P., Frank, L. M., and Pannu, S. S., 2013, “Insertion of Flexible Neural Probes Using Rigid Stiffeners Attached with Biodissolvable Adhesive,” *Journal of Visualized Experiments*, (79).
- [58] Zhang, S., Wang, C., Gao, H., Yu, C., Yan, Q., Lu, Y., Tao, Z., Linghu, C., Chen, Z., Xu, K., and Song, J., 2020, “A Removable Insertion Shuttle for Ultraflexible Neural Probe Implantation with Stable Chronic Brain Electrophysiological Recording,” *Advanced Materials Interfaces*, 7(6), p. 1901775.
- [59] Wu, F., Im, M., and Yoon, E., 2011, “A Flexible Fish-Bone-Shaped Neural Probe Strengthened by Biodegradable Silk Coating for Enhanced Biocompatibility,” In *2011 16th International Solid-State Sensors, Actuators and Microsystems Conference, IEEE, Beijing, China*, pp. 966–969.
- [60] Xiang, Z., Yen, S.-C., Xue, N., Sun, T., Tsang, W. M., Zhang, S., Liao, L.-D., Thakor, N. V., and Lee, C., 2014, “Ultra-Thin Flexible Polyimide Neural Probe Embedded in a Dissolvable Maltose-Coated Microneedle,” *Journal of Micromechanics and Microengineering*, 24(6), p. 065015.

- [61] Kozai, T. D. Y., Gugel, Z., Li, X., Gilgunn, P. J., Khilwani, R., Ozdoganlar, O. B., Fedder, G. K., Weber, D. J., and Cui, X. T., 2014, “Chronic Tissue Response to Carboxymethyl Cellulose Based Dissolvable Insertion Needle for Ultra-Small Neural Probes,” *Biomaterials*, 35(34), pp. 9255–9268.
- [62] Lewitus, D., Smith, K. L., Shain, W., and Kohn, J., 2011, “Ultrafast Resorbing Polymers for Use as Carriers for Cortical Neural Probes,” *Acta Biomaterialia*, 7(6), pp. 2483–2491.
- [63] Lecomte, A., Castagnola, V., Descamps, E., Dahan, L., Blatché, M. C., Dinis, T. M., Leclerc, E., Egles, C., and Bergaud, C., 2015, “Silk and PEG as Means to Stiffen a Parylene Probe for Insertion in the Brain: Toward a Double Time-Scale Tool for Local Drug Delivery,” *Journal of Micromechanics and Microengineering*, 25(12), p. 125003.
- [64] Lecomte, A., Descamps, E., and Bergaud, C., 2018, “A Review on Mechanical Considerations for Chronically-Implanted Neural Probes,” *Journal of Neural Engineering*, 15(3), p. 031001.
- [65] Ware, T., Simon, D., Hearon, K., Liu, C., Shah, S., Reeder, J., Khodaparast, N., Kilgard, M. P., Maitland, D. J., Rennaker, R. L., and Voit, W. E., 2012, “Three-Dimensional Flexible Electronics Enabled by Shape Memory Polymer Substrates for Responsive Neural Interfaces,” *Macromolecular Materials and Engineering*, 297(12), pp. 1193–1202.
- [66] Harris, J. P., Capadona, J. R., Miller, R. H., Healy, B. C., Shanmuganathan, K., Rowan, S. J., Weder, C., and Tyler, D. J., 2011, “Mechanically Adaptive Intracortical Implants Improve the Proximity of Neuronal Cell Bodies,” *Journal of Neural Engineering*, 8(6), p. 066011.
- [67] Sakes, A., Dodou, D., and Breedveld, P., 2016, “Buckling Prevention Strategies in Nature as Inspiration for Improving Percutaneous Instruments: A Review,” *Bioinspiration & Biomimetics*, 11(2), p. 021001.
- [68] Shoffstall, A. J., Srinivasan, S., Willis, M., Stiller, A. M., Ecker, M., Voit, W. E., Pancrazio, J. J., and Capadona, J. R., 2018, “A Mosquito Inspired Strategy to Implant Microprobes into the Brain,” *Scientific Reports*, 8(1), p. 122.
- [69] Kim, E. G. R., John, J. K., Tu, H., Zheng, Q., Loeb, J., Zhang, J., and Xu, Y., 2014, “A Hybrid Silicon–Parylene Neural Probe with Locally Flexible Regions,” *Sensors and Actuators B: Chemical*, 195, pp. 416–422.
- [70] Andrei, A., Tutunjyan, N., Verbinnen, G., VanPut, S., Krylychkina, O., Eberle, W., and Musa, S., 2012, “Fabrication and Successful In-Vivo Implantation of a Flexible Neural Implant with a Hybrid Polyimide-Silicon Design,” 2012 Annual International Conference of the IEEE Engineering in Medicine and Biology Society, IEEE, San Diego, CA, pp. 3890–3893.
- [71] A. Fomani, A., and Mansour, R. R., 2011, “Fabrication and Characterization of the Flexible Neural Microprobes with Improved Structural Design,” *Sensors and Actuators A: Physical*, 168(2), pp. 233–241.

- [72] Bernard, T. St., Chen, P. C., Hoople, J., Johnson, B., and Lal, A., 2015, "Silicon Horn Transducer Based Ultrasonically Enhanced Nerve Firing," 2015 IEEE International Ultrasonics Symposium (IUS), IEEE, Taipei, Taiwan, pp. 1–4.
- [73] Chen, P.-C., and Lal, A., 2015, "Detachable Ultrasonic Enabled Inserter for Neural Probe Insertion Using Biodissolvable Polyethylene Glycol," In 2015 Transducers - 2015 18th International Conference on Solid-State Sensors, Actuators and Microsystems (TRANSDUCERS), IEEE, Anchorage, AK, USA, pp. 125–128.
- [74] Zhang, E. Y., 2018, "Microinvasive Probes for the Longitudinal Interrogation of Neural Dynamics," Doctoral dissertation, Massachusetts Institute of Technology.
- [75] Yang, M., and Zahn, J. D., 2004, "Microneedle Insertion Force Reduction Using Vibratory Actuation," *Biomedical Microdevices*, 6(3), pp. 177–182.
- [76] Huang, Y. C., Tsai, M. C., and Lin, C. H., 2012, "A Piezoelectric Vibration-Based Syringe for Reducing Insertion Force," *IOP Conference Series: Materials Science and Engineering*, 42, p. 012020.
- [77] Xiaochun Liao, Sadiq, M., Corner, G., Cochran, S., and Zhihong Huang, 2013, "Reduced Penetration Force through Ultrasound Activation of a Standard Needle: An Experimental and Computational Study," In 2013 IEEE International Ultrasonics Symposium (IUS), pp. 1436–1439.
- [78] Cai, Y., Moore, J., and Lee, Y.-S., 2018, "Vibration Study of Novel Compliant Needle Used for Vibration-Assisted Needle Insertion," *Computer-Aided Design and Applications*, 16(4), pp. 742–754.
- [79] Cai, Y., Moore, J., and Lee, Y.-S., 2017, "Novel Surgical Needle Design and Manufacturing for Vibratory-Assisted Insertion in Medical Applications," *Computer-Aided Design and Applications*, 14(6), pp. 833–843.
- [80] Wilson, W. C., and Atkinson, G. M., 2007, Review of polyimides used in the manufacturing of microsystems.
- [81] Cheung, K. C., Renaud, P., Tanila, H., and Djupsund, K., 2007, "Flexible Polyimide Microelectrode Array for in Vivo Recordings and Current Source Density Analysis," *Biosensors and Bioelectronics*, 22(8), pp. 1783–1790.
- [82] Constantin, C. P., Aflori, M., Damian, R. F., and Rusu, R. D., 2019, "Biocompatibility of Polyimides: A Mini-Review," *Materials*, 12(19), p. 3166.
- [83] Hartwig, V., Carbonaro, N., Tognetti, A., and Vanello, N., 2017, "Systematic Review of fMRI Compatible Devices: Design and Testing Criteria," *Annals of biomedical engineering*, 45(8), pp. 1819–1835.
- [84] Wang, Y., Lee, S.-H., Shih, Y. I., and Lee, Y.-S., 2022, "Design and Fabrication of MRI-Compatible and Flexible Neural Microprobes for Deep Brain Stimulation and Neurological

- Treatment Applications,” Submitted to Manufacturing Science and Engineering Conference 2022.
- [85] Christiaens, W., “Active and Passive Component Integration in Polyimide Interconnection Substrates,” Doctoral dissertation, Ghent University.
- [86] Nguyen, T. N. T., and Lee, N.-E., 2007, “Deep Reactive Ion Etching of Polyimide for Microfluidic Applications,” *Journal of the Korean Physical Society*, 51(3), pp. 984-988.
- [87] Christiaens, W., Loehner, T., Pahl, B., Feil, M., Vandeveld, B., and Vanfleteren, J., 2008, “Embedding and Assembly of Ultrathin Chips in Multilayer Flex Boards,” *Circuit World*, 34(3), pp. 3–8.
- [88] Chen, Y., Mao, H., Tan, Q., Xue, C., Ou, W., Liu, J., and Chen, D., 2014, “Fabrication of Polyimide Sacrificial Layers with Inclined Sidewalls Based on Reactive Ion Etching,” *AIP Advances*, 4(3), p. 031328.
- [89] Bagolini, A., Pakula, L., Scholtes, T. L. M., Pham, H. T. M., French, P. J., and Sarro, P. M., 2002, “Polyimide Sacrificial Layer and Novel Materials for Post-Processing Surface Micromachining,” *Journal of Micromechanics and Microengineering*, 12(4), pp. 385–389.
- [90] Zawierta, M., Martyniuk, M., Jeffery, R. D., Putrino, G., Keating, A., Silva, K. K. M. B. D., and Faraone, L., 2017, “Control of Sidewall Profile in Dry Plasma Etching of Polyimide,” *Journal of Microelectromechanical Systems*, 26(3), pp. 593–600.
- [91] Kim, B. J., and Meng, E., 2016, “Review of Polymer MEMS Micromachining,” *Journal of Micromechanics and Microengineering*, 26(1), p. 013001.
- [92] du Toit, H., and Di Lorenzo, M., 2014, “Electrodeposited Highly Porous Gold Microelectrodes for the Direct Electrocatalytic Oxidation of Aqueous Glucose,” *Sensors and Actuators B: Chemical*, 192, pp. 725–729.
- [93] Tsujino, J., Sano, T., Ogata, H., Tanaka, S., and Harada, Y., 2002, “Complex Vibration Ultrasonic Welding Systems with Large Area Welding Tips,” *Ultrasonics*, 40(1–8), pp. 361–364.
- [94] Gao, J., and Altintas, Y., 2019, “Development of a Three-Degree-of-Freedom Ultrasonic Vibration Tool Holder for Milling and Drilling,” *IEEE/ASME Transactions on Mechatronics*, pp. 1–1.
- [95] Liu, Y., Yan, J., Wang, L., and Chen, W., 2019, “A Two-DOF Ultrasonic Motor Using a Longitudinal–Bending Hybrid Sandwich Transducer,” *IEEE Transactions on Industrial Electronics*, 66(4), pp. 3041–3050.
- [96] Li, C., Lu, C., Huang, W., and Ma, Y., 2014, “Design and Finite Element Analysis of a Novel Longitudinal-Torsional Hybrid Ultrasonic Motor,” *Proceedings of the 2014 Symposium on Piezoelectricity, Acoustic Waves, and Device Applications*, pp. 76–79.

- [97] Lin Shuyu, 1997, “Sandwiched Piezoelectric Ultrasonic Transducers of Longitudinal-Torsional Compound Vibrational Modes,” *IEEE Transactions on Ultrasonics, Ferroelectrics, and Frequency Control*, 44(6), pp. 1189–1197.
- [98] Tsujino, J., 1998, “Ultrasonic Motor Using a One-Dimensional Longitudinal-Torsional Vibration Converter with Diagonal Slits,” *Smart Materials and Structures*, 7(3), pp. 345–351.
- [99] Al-Budairi, H., and Lucas, M., 2012, “An Analytical Model of a Longitudinal-Torsional Ultrasonic Transducer,” In *Journal of Physics: Conference Series*, 382, p. 012061.
- [100] Al-Budairi, H., Lucas, M., and Harkness, P., 2013, “A Design Approach for Longitudinal-Torsional Ultrasonic Transducers,” *Sensors and Actuators A: Physical*, 198, pp. 99–106.
- [101] Ni, H., Wang, Y., Gong, H., Pan, L., Li, Z. J., and Wang, D., 2018, “A Novel Free-Form Transducer for the Ultra-Precision Diamond Cutting of Die Steel,” *The International Journal of Advanced Manufacturing Technology*, 95(5–8), pp. 2185–2192.
- [102] Yap, C. Y., Chua, C. K., Dong, Z. L., Liu, Z. H., Zhang, D. Q., Loh, L. E., and Sing, S. L., 2015, “Review of Selective Laser Melting: Materials and Applications,” *Applied Physics Reviews*, 2(4), p. 041101.
- [103] Brandl, E., Heckenberger, U., Holzinger, V., and Buchbinder, D., 2012, “Additive Manufactured AlSi10Mg Samples Using Selective Laser Melting (SLM): Microstructure, High Cycle Fatigue, and Fracture Behavior,” *Materials & Design*, 34, pp. 159–169.
- [104] Siddique, S., Awd, M., Tenkamp, J., and Walther, F., 2017, “High and Very High Cycle Fatigue Failure Mechanisms in Selective Laser Melted Aluminum Alloys,” *Journal of Materials Research*, 32(23), pp. 4296–4304.
- [105] Rosenthal, I., Stern, A., and Frage, N., 2014, “Microstructure and Mechanical Properties of AlSi10Mg Parts Produced by the Laser Beam Additive Manufacturing (AM) Technology,” *Metallography, Microstructure, and Analysis*, 3(6), pp. 448–453.
- [106] Wang, Y., Cai, Y., Gong, H., and Lee, Y.-S., “Design and 3D Printing of Waveguide-Based Ultrasonic Longitudinal-Torsional Transducers for Medical Needle Insertion,” *Submit to Sensors and Actuators A: Physical*, under review.
- [107] Cornogolub, A., Cottinet, P.-J., and Petit, L., 2014, “Analytical Modeling of Curved Piezoelectric, Langevin-Type, Vibrating Transducers Using Transfer Matrices,” *Sensors and Actuators A: Physical*, 214, pp. 120–133.
- [108] Chen, P.-C., Clark, C., Shen, C.-P. J., Schaffer, C., and Lal, A., 2013, “Ultrasonically Actuated Inserted Neural Probes for Increased Recording Reliability,” In *2013 Transducers & Eurosensors XXVII: The 17th International Conference on Solid-State Sensors, Actuators and Microsystems (TRANSDUCERS & EUROSENSORS XXVII)*, IEEE, Barcelona, Spain, pp. 872–875.

- [109] Ramasubramanian, M. K., Barham, O. M., and Swaminathan, V., 2008, “Mechanics of a Mosquito Bite with Applications to Microneedle Design,” *Bioinspiration & Biomimetics*, 3(4), p. 046001.
- [110] Gutowski, P., and Leus, M., 2012, “The Effect of Longitudinal Tangential Vibrations on Friction and Driving Forces in Sliding Motion,” *Tribology International*, 55, pp. 108–118.
- [111] Tsai, C. C., and Tseng, C. H., 2006, “The Effect of Friction Reduction in the Presence of In-Plane Vibrations,” *Archive of Applied Mechanics*, 75(2–3), pp. 164–176.
- [112] Littmann, W., Storck, H., and Wallaschek, J., 2001, “Sliding Friction in the Presence of Ultrasonic Oscillations: Superposition of Longitudinal Oscillations,” *Archive of Applied Mechanics (Ingenieur Archiv)*, 71(8), pp. 549–554.
- [113] Wang, Y., Lee, Y.-S., Cai, Y., Sun, Y., and Gong, H., 2020, “Design of Ultrasonic Longitudinal-Torsional Vibrator Based on Waveguide Principle for Manufacturing and Medical Applications,” *Procedia Manufacturing*, 48, pp. 114–122.
- [114] Reed, K. B., Okamura, A. M., and Cowan, N. J., 2009, “Modeling and Control of Needles With Torsional Friction,” *IEEE Transactions on Biomedical Engineering*, 56(12), pp. 2905–2916.
- [115] Teidelt, E., Popov, V., and Starcevic, J., 2011, “Influence of In-Plane and Out-of-Plane Ultrasonic Oscillations on Sliding Friction,” *SAE Int. J. Passeng. Cars – Mech. Syst.*, 4(3), pp. 1387–1393.
- [116] Wang, Y., Shih, Y. Y. I., and Lee, Y., 2021, “Vibration-Assisted Insertion of Flexible Neural Microelectrodes With Bio-Dissolvable Guides for Medical Implantation,” In *International Manufacturing Science and Engineering Conference (Vol. 85062, p. V001T03A009)*. American Society of Mechanical Engineers.
- [117] Chen, Z.-J., Broaddus, W. C., Viswanathan, R. R., Raghavan, R., and Gillies, G. T., 2002, “Intraparenchymal Drug Delivery via Positive-Pressure Infusion: Experimental and Modeling Studies of Poroelasticity in Brain Phantom Gels,” *IEEE Transactions on Biomedical Engineering*, 49(2), pp. 85–96.
- [118] Pomfret, R., Miranpuri, G., and Sillay, K., 2013, “The Substitute Brain and the Potential of the Gel Model,” *Annals of Neurosciences*, 20(3).
- [119] Fiáth, R., Márton, A. L., Mátyás, F., Pinke, D., Márton, G., Tóth, K., and Ulbert, I., 2019, “Slow Insertion of Silicon Probes Improves the Quality of Acute Neuronal Recordings,” *Scientific Reports*, 9(1).
- [120] Liang, Z., Watson, G. D. R., Alloway, K. D., Lee, G., Neuberger, T., and Zhang, N., 2015, “Mapping the Functional Network of Medial Prefrontal Cortex by Combining Optogenetics and fMRI in Awake Rats,” *NeuroImage*, 117, pp. 114–123.
- [121] Wang, Y., Cai, Y., and Lee, Y.-S., 2021, “Design and Development of Longitudinal and

Torsional Ultrasonic Vibration-Assisted Needle Insertion Device for Medical Applications,”
Computer-Aided Design and Application, 19(4), pp. 797–811.